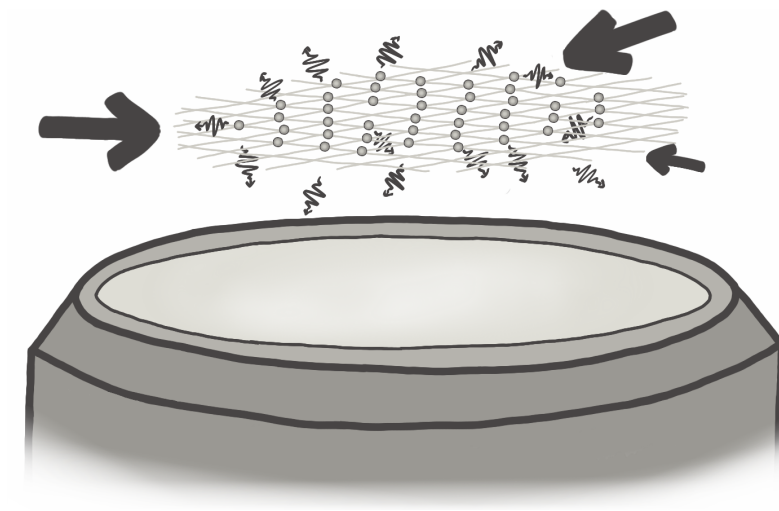# A Microscope for Fermi Gases

Ahmed Omran

München 2016

A Microscope for Fermi Gases

Dissertation
an der Fakultät für Physik
der Ludwig–Maximilians–Universität
München

vorgelegt von
AHMED OMRAN
aus Kairo, Ägypten

München, den 16.03.2016

Erstgutachter: Prof. Dr. Immanuel Bloch
Zweitgutachter: Prof. Dr. Selim Jochim
Tag der mündlichen Prüfung: 11.05.2016

Zusammenfassung

Diese Dissertation berichtet über ein neuartiges Quantengasmikroskop, mit dem Vielteilchensysteme von fermionischen Atomen in optischen Gittern untersucht werden. Die einzelplatzaufgelöste Abbildung ultrakalter Gase im Gitter hat mächtige Experimente an bosonischen Vielteilchensystemen ermöglicht. Die Erweiterung dieser Fähigkeit auf Fermigase bietet neue Aussichten, komplexe Phänomene stark korrelierter Systeme zu erforschen, für die numerische Simulationen oft nicht möglich sind.

Mit Standardtechniken der Laserkühlung, optischen Fallen und Verdampfungskühlung werden ultrakalte Fermigase von ^{6}Li präpariert und in ein 2D optisches Gitter mit flexibler Geometrie geladen. Die Atomverteilung wird mithilfe eines zweiten, kurzskaligen Gitters eingefroren. Durch Raman-Seitenbandkühlung wird an jedem Atom Fluoreszenz induziert, während seine Position festgehalten wird. Zusammen mit hochauflösender Abbildung erlaubt die Fluoreszenz die Rekonstruktion der ursprünglichen Verteilung mit Einzelplatzauflösung und hoher Genauigkeit.

Mithilfe von magnetisch angetriebener Verdampfungskühlung produzieren wir entartete Fermigase mit fast einheitlicher Füllung im ersten Gitter. Dies ermöglicht die ersten mikroskopischen Untersuchungen an einem ultrakalten Gas mit klaren Anzeichen von Fermi-Statistik. Durch die Präparation eines Ensembles spinpolarisierter Fermigase detektieren wir eine Abflachung im Dichteprofil im Zentrum der Wolke, ein Charakteristikum bandisolierender Zustände.

In einem Satz von Experimenten weisen wir nach, dass Verluste von Atompaaren an einem Gitterplatz, bedingt durch lichtinduzierte Stöße, umgangen werden. Die Überabtastung des zweiten Gitters erlaubt eine deterministische Trennung der Atompaare in unterschiedliche Gitterplätze. Die Kompression einer dichten Wolke in der Falle vor dem Laden ins Gitter führt zu vielen Doppelbesetzungen von Atomen in unterschiedlichen Bändern, die wir ohne Anzeichen von paarweisen Verlusten abbilden können. Somit erhalten wir die wahre Besetzungsstatistik an jedem Gitterplatz.

Mithilfe dieser Besonderheit werten wir die lokale Besetzungsstatistik an einem Ensemble bandisolierender Wolken aus. Im Zentrum bei hoher Füllung sind die Atomzahlfluktuationen um eine Größenordnung unterdrückt, verglichen mit klassischen Gasen, eine Manifestation des Pauliverbots. Die Besetzungswahrscheinlichkeiten werden verwendet, um die lokale Entropie an jedem Gitterplatz zu messen. Eine niedrige Entropie pro Atom bis $0.34k_{\mathrm{B}}$ wird im Zentrum des Bandisolators gefunden.

Die Erweiterung der Quantengasmikroskopie auf entartete Fermigase eröffnet neue Möglichkeiten der Quantensimulation stark korrelierter Vielteilchensysteme und kann einzigartige Erkenntnisse über fermionische Systeme im und außerhalb vom Gleichgewicht, Quantenmagnetismus und verschiedene Phasen des Fermi-Hubbard-Modells ergeben.

Abstract

This thesis reports on a novel quantum gas microscope to investigate many-body systems of fermionic atoms in optical lattices. Single-site resolved imaging of ultracold lattice gases has enabled powerful studies of bosonic quantum many-body systems. The extension of this capability to Fermi gases offers new prospects to studying complex phenomena of strongly correlated systems, for which numerical simulations are often out of reach.

Using standard techniques of laser cooling, optical trapping, and evaporative cooling, ultracold Fermi gases of ^{6}Li are prepared and loaded into a large-scale 2D optical lattice of flexible geometry. The atomic distribution is frozen using a second, short-scaled lattice, where we perform Raman sideband cooling to induce fluorescence on each atom while maintaining its position. Together with high-resolution imaging, the fluorescence signals allow for reconstructing the initial atom distribution with single-site sensitivity and high fidelity.

Magnetically driven evaporative cooling in the plane allows for producing degenerate Fermi gases with almost unity filling in the initial lattice, allowing for the first microscopic studies of ultracold gases with clear signatures of Fermi statistics. By preparing an ensemble of spin-polarised Fermi gases, we detect a flattening of the density profile towards the centre of the cloud, which is a characteristic of a band-insulating state.

In one set of experiments, we demonstrate that losses of atom pairs on a single lattice site due to light-assisted collisions are circumvented. The oversampling of the second lattice allows for deterministic separation of the atom pairs into different sites. Compressing a high-density sample in a trap before loading into the lattice leads to many double occupancies of atoms populating different bands, which we can image with no evidence for pairwise losses. We therefore gain direct access to the true number statistics on each lattice site.

Using this feature, we can evaluate the local number statistics on an ensemble of band-insulating clouds. In the central region of high filling, the atom number fluctuations are suppressed by an order of magnitude compared to classical gases, which is a manifestation of Pauli blocking. Occupation probabilities are used to measure the local entropy on each individual site. The entropy per atom is found to be as low as $0.34k_\mathrm{B}$ in the band-insulating core.

The extension of quantum gas microscopy to degenerate Fermi gases opens up new avenues in quantum simulation of strongly correlated many-body systems and can yield unprecedented insight into fermionic systems in and out of equilibrium, quantum magnetism and different phases of the Fermi-Hubbard model.

Contents

To my family

Chapter 1

Introduction

The degenerate Fermi gas is a ubiquitous system in nature. In the standard model, fermions make up all elementary constituents of matter, and quantum degenerate gases of fermions are found everywhere, most importantly electrons in solids and nuclear matter. Identical fermions are forbidden from occupying the same quantum state, which is the statement of the famous Pauli exclusion principle [1]. This is responsible for the stability of large systems of matter [2–4], which are prevented from collapsing under electrostatic forces (solids) or gravitation (white dwarfs and neutron stars).

The study of degenerate quantum matter has a long history and has given rise to many applications. For example, superconductivity has been subject to intense research for over a century and has enabled several technological breakthroughs. As another example, 2D electron gases have strongly impacted upon fundamental and applied research in solid state physics. They are found in field effect transistors, now an indispensable piece of technology, and the quantum Hall effect was discovered in these systems [5], leading to new precise standards of electrical resistance.

Many properties of materials arise due to interactions between their constituents. In solids, where the Coulomb interactions between electrons are very strong, it seems almost counterintuitive that electronic phenomena could be described very well in a picture of very weakly interacting quasiparticles, which is the basis of Landau's hugely successful Fermi-liquid theory [6, 7]. Within this framework, it became possible to understand macroscopic quantum phenomena, such as giant magnetoresistance [8, 9] and conventional BCS superconductivity [10]. However, novel materials have emerged, where interactions and correlations between electrons or spins are so strong that the Fermi-liquid picture breaks down. Strongly correlated systems are found, for example, in certain quasi-2D electron gases [11], which include high-T_c superconductors [12]. The complexity of the interactions and the difficulty of numerical simulations of these materials has impeded a full understanding of many emergent phenomena in these quantum many-body systems.

The advent of ultracold atoms

Over the past few decades, ultracold atoms have offered new ways of studying quantum systems by providing a clean, flexible, and tunable platform for realising and simulating various quantum models [13]. This is in line with Richard Feynman's vision of using quantum devices to accurately simulate quantum systems [14]. The field of ultracold atoms is comparatively young, but already very successful.

The idea of cooling dilute vapours with radiation pressure is over four decades old [15, 16]. This has come to fruition with the laser cooling of trapped ions [17, 18] and the cooling and trapping of neutral atoms [19, 20]. More advanced laser cooling techniques such as polarisation-gradient cooling [21, 22], velocity-selective coherent population trapping [23], and sideband cooling in harmonic traps [24] have been employed to overcome the Doppler and recoil limits of laser cooling. However, these techniques did not suffice to bring atomic vapours to quantum degeneracy. It was the development of magnetic traps for neutral atoms [25] together with evaporative cooling techniques [26, 27] that have enabled the observation of Bose-Einstein condensation (BEC) in ultracold atomic clouds [28–30]. Far-detuned optical traps [31] and evaporative cooling therein [32] offer added flexibility and are now commonly used in the lab.

Since the observation of BEC, the field has undergone rapid developments. The phase coherence in BECs was investigated via matter-wave interference [33], and exploited to realise atom lasers [34–36]. In weakly interacting Bose gases, the excitations described by Bogoliubov theory could be investigated [37–41]. Other excitations such as vortices [42–44] and solitons [45, 46] were also observed.

All the aforementioned results can be described in a mean-field context with weakly interacting quasiparticles. For interactions comparable to the kinetic energy or even larger, one must depart from this picture, but therefore gains access to many rich phenomena with strong correlations between the atoms. This regime can be reached by using Feshbach resonances [47, 48] that modify the low energy scattering properties [49, 50]. However, dipolar collisions and three-body recombination cause strong losses in BECs [51, 52]. Another way to increase the role of interactions is by confining the atoms to low-dimensional geometries. For example, a Tonks-Girardeau gas could be realised with interacting bosons in 1D [53, 54].

Ultracold Fermi gases

The adaptation of the cooling methods to fermionic alkali atoms led to the production of a degenerate Fermi gas via evaporative cooling of spin mixtures [55]. Since

then, several Fermi gas experiments have been constructed, where mixtures of different spin components or atomic species were cooled together [56–60]. Basic properties of fermions arising from their quantum statistics could be observed, for example antibunching [61] or suppression of density fluctuations due to Pauli blocking [62, 63].

While accessing the strongly correlated regime using Feshbach resonances with bosons was challenging due to strong three-body relaxation, Pauli blocking turned out to stabilise Fermi gases against these losses [64], making Feshbach resonances useful to probe a wide range of interactions. Thus, interacting ultracold Fermi gases have attracted great theoretical interest [65]. Strongly interacting Fermi gases were soon realised [66, 67], as well as condensates of molecules created from fermion pairs [68–70], Cooper pairs in the attractive BCS regime [71], and superfluids of fermions [72–74].

Fermi gas experiments have traditionally employed the alkali atoms ^{6}Li and ^{40}K. Later, other fermionic isotopes have been successfully cooled to quantum degeneracy, namely the alkaline earth atoms ^{87}Sr [75, 76], or alkaline earthlike lanthanides such as ^{161}Dy [77], ^{167}Eb [78], ^{171}Yb and ^{173}Yb [79, 80]. Their complex level structures enable the realisation of outstanding optical clocks [81–83] and quantum information protocols [84, 85]. With their permanent magnetic dipole moments, one can access the rich physics of dipolar quantum gases [86] and exotic spin models [87, 88].

Optical lattices

For both fermions and bosons, there is another successful approach to entering the strongly correlated regime. Instead of enhancing the interaction energy by Feshbach resonances, the kinetic energy is suppressed by confining the atoms in optical lattices [89], standing waves of light that represent clean periodic potentials for neutral atoms, and for which many different geometries can be implemented [90].

An immediate success of the optical lattice approach was the observation of transition from a superfluid to a Mott insulator with bosonic atoms [91]. This proved that synthetic quantum systems can indeed be used to study phenomena known from solid state physics in a novel way [92]. Fermions in optical lattices have attracted a lot of interest for addressing open questions in quantum many-body physics [93, 94]. For repulsive interactions, the crossover from conducting to Mott insulating states could be probed [95, 96], as well as magnetic correlations [97, 98].

Probing optical lattices

Different methods can be used to study optical lattice gases. A sudden release of the atoms from the lattice gives access to coherence properties through the interference

of expanding wave functions [91, 99], while underlying many-body properties can be detected via correlations in the density noise of expanding clouds [61, 100, 101]. The quasi-momentum distribution in the lattice can be converted into real-space momentum via adiabatic band mapping [102]. Bragg spectroscopy can be used to probe the excitation spectrum and spatial ordering [98, 103]. High-resolution in situ absorption imaging can yield the density distribution [104, 105]. A state-of-the-art approach is using high-resolution fluorescence imaging to resolve the spatial lattice population with single atom sensitivity. This imaging technique, termed quantum gas microscopy, has proven to be an especially powerful method for investigating optical lattice systems.

The technique of site resolved imaging was achieved with fluorescence [106] and absorption imaging [107] in large spaced optical lattices, not yet in the strongly correlated regime. Higher resolution imaging and addressing could be achieved using electron beam microscopy on lattice sites with many atoms [108, 109]. Then, two experiments were realised with fluorescence imaging of single ^{87}Rb atoms in lattices with submicron spacings [110, 111].

Since then, single-atom resolved imaging has enabled microscopic studies of phase transitions [111, 112], dynamics [113–115], correlations [116], nonlocal order [117], spin interactions [118], quantum magnetism [119], long-range interactions and collective dynamics using Rydberg atoms [120–122] and entanglement[123, 124]. Following the two pioneering ^{87}Rb experiments, two quantum gas microscopes of bosonic ^{174}Yb have recently been demonstrated [125, 126].

Applying similar techniques to the imaging of single fermions in optical lattices offered prospects of studying interesting spin physics and address open questions of condensed matter. However, the more difficult cooling of fermions in regular traps and in optical lattices required several more years of development to achieve the same technology. Finally in 2015, five groups, including ours, have reported the imaging of single fermionic atoms in optical lattices [127–131], paving the way to novel studies of fermionic many-body systems.

Outline

This thesis describes the development of a new-generation quantum gas microscope for fermionic ^{6}Li, with the first measurements on degenerate Fermi gases using this method. The experiment has the unique features of a tunable and nontrivial lattice geometry, and a dedicated optical lattice for the imaging process, allowing for unprecedented insights into fermionic systems. We also find that our method allows for overcoming a common limitation of quantum gas microscopes, where pairs of atoms populating the same lattice site get lost during imaging [110, 111]. We use this to probe number statistics in the lattice and measure statistical properties of our system.

The chapters are structured as follows:

- Chapter 2 presents some basic properties of Fermi gases, and compares energy scales of Fermi gases in nature and those created in the lab. A brief summary of the band structure in inhomogeneous optical lattices is given, and the Fermi-Hubbard model is described, as well as the different phases expected to emerge from it.

- Chapter 3 describes the experimental setup. The various subsystems developed in the course of this work for creating and probing ultracold Fermi gases are explained.

- Chapter 4 describes the experimental protocol. Using several stages of laser cooling and evaporative cooling, ^{6}Li atoms are brought from a hot vapour down to quantum degeneracy in a 2D plane of an optical lattice.

- Chapter 5 focuses on the Raman sideband cooling in an optical lattice and the simultaneous fluorescence imaging of single atoms. The circumvention of pair-wise losses of atoms during imaging is discussed in more detail.

- Chapter 6 deals with a statistical study of a gas of identical fermions in the band-insulating regime. A flattening of the density profile, strong suppression of density fluctuations and low entropy per atom are observed. Finally, density-density correlations are evaluated as a basic measure for compressibility.

- Chapter 7 summarises the work and gives an outlook on recent and future developments.

The main results of this work have recently been published in:

Microscopic observation of Pauli blocking in degenerate fermionic lattice gases
A. Omran, M. Boll, T. Hilker, K. Kleinlein, G. Salomon, I. Bloch and C. Gross
Phys. Rev. Lett. **115**, 263001 (2015)

Chapter 2

Ultracold Fermi gases

This chapter briefly reviews the basic properties of ultracold Fermi gases. The so-called Fermi energy sets a characteristic energy scale, and is discussed for free and trapped Fermi gases. A comparison is made between Fermi gases occurring in nature on the one hand, and their synthetic, ultracold counterparts on the other.

The main part of the chapter focuses on fermions in periodic potentials. Because of its relevance for our experiment, the band structure in inhomogeneous optical lattices is briefly described. This work aims to realise a useful quantum simulator for the Fermi-Hubbard model, which is commonly used in solid state physics and thought to be a minimal model for describing high-T_c superconductors. In addition, the Fermi-Hubbard model is expected to possess a multitude of phases under different conditions, some of which are presented here.

2.1 Fermi energy

Special properties of Fermi gases arise from their quantum statistics. A system of many fermions must have a wave functions which is fully antisymmetric with respect to the exchange of two fermions [132]. For a system with a set of eigenstates $\{|i\rangle\}$, the creation and annihilation operators $\hat{a}_i^\dagger$ and $\hat{a}_i$ for identical fermions in the different modes fulfill the anticommutation relations:

$$\left\{\hat{a}_i, \hat{a}_j\right\} = \left\{\hat{a}_i^\dagger, \hat{a}_j^\dagger\right\} = 0 \tag{2.1a}$$

$$\left\{\hat{a}_i, \hat{a}_j^\dagger\right\} = \delta_{ij} \tag{2.1b}$$

Eq. (2.1a) is in accordance with Pauli's principle: we cannot create two fermions in the same mode, as $\left(\hat{a}_i^\dagger\right)^2 |0\rangle = -\left(\hat{a}_i^\dagger\right)^2 |0\rangle = 0$, where $|0\rangle$ is a vacuum state. Therefore, N fermions must necessarily distribute themselves among N different states. For N fermions at zero temperature, the energetically lowest N single-particle levels are populated. The energy of the highest populated level is called the Fermi energy ε_F. We can express the Fermi energy in terms of a Fermi temperature $T_F = \varepsilon_F/k_B$ or a Fermi momentum $\hbar k_F = \sqrt{2m\varepsilon_F}$.

2.1.1   Homogeneous systems

The Fermi energy generally depends on the potential landscape and the dimensionality of the system, in addition to the number of fermions. ε_F can always be obtained by integrating over the density of states for all energies, and adjusting the value of ε_F to obtain the correct particle number [133]. For homogeneous systems of fixed volume V in d dimensions, we can also simply count the number of momentum eigenstates that go up to the Fermi momentum k_F, which is the boundary between momentum states which are occupied at $T = 0$ and those which are not. The number of momentum states within the "sphere" of radius k_F is given by an integral over momentum space, divided by the number of states per momentum space volume [133]:

$$N = \int\limits^{|\vec{k}|=k_F} \mathrm{d}^d k \, \frac{V}{(2\pi)^d} \tag{2.2}$$

By using the dispersion relation for free particles $\varepsilon = \hbar^2 k^2 / 2m$, we can convert Eq. (2.2) to an integral over energy up to ε_F. This gives a relation between the Fermi energy and number density $n = N/V$ of the fermions:

$$\varepsilon_F = \frac{\hbar^2}{2m} \times \begin{cases} \left(3\pi^2 n\right)^{2/3} & \text{(3D)} \\ (2\pi n) & \text{(2D)} \\ (\pi n)^2 & \text{(1D)} \end{cases} \tag{2.3}$$

2.1.2   Harmonically trapped gases

Experiments on ultracold atoms usually operate with particles confined in approximately harmonic optical or magnetic traps. Consider a gas of N identical fermions in a harmonic potential with different trap frequencies ω_i at $T = 0$. N is equal to the number of states with $\varepsilon \leq \varepsilon_F$, which is given by an integral over all energies up to a total energy ε_F, divided by the number of states per energy interval. For example, in 3D this gives:

$$N = \left(\prod_{i=1}^{3} \frac{1}{\hbar\omega_i}\right) \int\limits_0^{\varepsilon_F} \mathrm{d}\varepsilon_1 \int\limits_0^{\varepsilon_F - \varepsilon_1} \mathrm{d}\varepsilon_2 \int\limits_0^{\varepsilon_F - \varepsilon_1 - \varepsilon_2} \mathrm{d}\varepsilon_3 \tag{2.4}$$

Generalising this to d dimensions, one can then show that the relation between the Fermi energy and particle number is given by:

$$\varepsilon_F = \hbar\overline{\omega} \left(d! N\right)^{1/d} \tag{2.5}$$

where $\overline{\omega} = (\prod_{i=1}^{d} \omega_i)^{1/d}$ is the geometric mean of the trap frequencies. Here we assume the N fermions are identical. If they are distributed among different internal

states, we treat these states separately and assign to each state its own Fermi energy.

In the case of cold atoms confined to shallow harmonic traps, where the average energy is much larger than the trap level spacing, the density varies slowly over the trapping potential $V(\vec{r})$. One then typically applies the local-density approximation [13, 65], where a local chemical potential is given by $\mu(\vec{r}) = \mu(0) - V(\vec{r})$. As the chemical potential and Fermi energy are of the same order for low temperatures [133], the system can be treated as possessing a wide range of Fermi energies. This makes global thermodynamic measurements challenging due to the average over the trap. However, the trap provides simultaneous access to different phases, and new techniques have been developed to measure the full equations of state with trapped gases [134–140]. Furthermore, the high-resolution imaging described in this work provides a way to go beyond the trap average and isolate regions of a given local thermodynamic configuration.

2.1.3 Fermi energy scales

For electrons in metals, where the densities are on the order of 10^{23}-10^{24} cm^{-3} [141], the Fermi temperature is on the order of several 10^4 K. This is two orders of magnitude higher than room temperature, hence electrons in metals are strongly degenerate systems. Neutron stars are a more striking example. Consisting mostly of neutrons with densities of up to 10^{38} cm^{-3}, the Fermi temperature is several 10^{11} K. This is larger than the core temperature and many orders of magnitude higher than the surface temperature [142]. Therefore, even these extreme systems are deeply quantum degenerate.

It is very hard for ultracold Fermi gases to compete with natural Fermi gases in terms of quantum degeneracy. The ground state of dilute vapours is the solid state. The only way to avoid solidification in alkali atomic clouds is to prepare low enough densities $< 10^{13}$ cm^{-3}, such that three-body recombinations are very unlikely to occur and the vapour remains metastable. As a consequence of the low density, the energy scale for quantum degeneracy becomes extremely small, and the Fermi temperature is typically on the μK scale. So far, experiments on ultracold Fermi gases have reached a few percent of the Fermi temperature [98, 136]. This is still less degenerate than for naturally occurring Fermi gases, despite their much higher temperature.

Nevertheless, the usefulness of ultracold Fermi gases stems from the strong interactions one can engineer, which give access to phenomena previously reserved for extremely degenerate matter. For example, the onset of fermionic superfluidity in conventional superconductors and ^{3}He occurs at temperatures several orders of magnitude lower than T_F [143], whereas superfluidity can occur in strongly interacting Fermi gases at temperatures on the order of $0.2T_F$ [144, 145]. This temperature is readily accessible in experiments and has allowed for fascinating studies of superfluid

properties [74, 138, 146].

Sometimes, temperature is not even the most relevant quantity. For characterising ordered phases, it is more useful to speak of entropy [147]. Here, ultracold Fermi gases have a clear advantage, being very clean systems with only few contributions to the system entropy. In solids, on the other hand, the entropy is often dominated by defects and strong coupling to the environment.

2.2 Fermions in optical lattices

2.2.1 Band structure in inhomogeneous lattices

We turn to a discussion of fermionic particles in periodic potentials. Electrons in a crystal lattice are the most common manifestation of this system. It is well known that these particles have eigenstates described by extended Bloch functions with eigenenergies extending over energy bands separated by finite gaps [133]. The band structure depends on the potential shape and depth.

Ultracold atom experiments often make use of sinusoidal optical lattices, for which a regular band structure exists with all its features [13]. However, the lattice potential is not spatially homogeneous, as one typically employs Gaussian red-detuned lattice beams, or blue-detuned lattices together with an extra red-detuned confinement trap. The Gaussian confinement can be approximated in the centre of the lattice by a harmonic potential, which breaks translational invariance. As a consequence, the eigenfunctions of the total potential are oscillatory but not periodic, and they typically decay over much fewer lattice periods than Bloch functions in regular solids.

For a confinement that varies slowly compared to the lattice constant, one can describe the energy structure of the system as regular energy bands of a comparable homogeneous lattice, which are bent by the external confinement. If identical fermions are placed into the system at $T = 0$, the lowest energy eigenstates are successively populated from the bottom up. At some point, adding more fermions does not lead to a higher peak in the total density profile, but the cloud just increases in diameter with a flat density distribution [148, 149].

However, for fermions that are sufficiently far away from the trap centre, the eigenenergies are larger than the lowest energy of the first excited band at the centre. There, it becomes energetically more favourable for the particles to populate the next higher band, and the central density starts to increase above one particle per site. The system consists of a lowest band with an insulating core of flat-top density and an excited band that is still conducting. A qualitative picture is shown in Fig. 2.1.
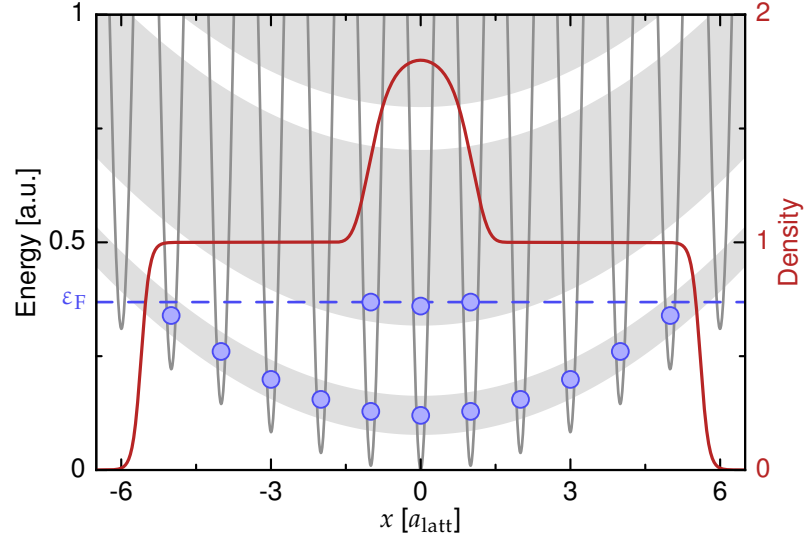
Figure 2.1: Band structure in an optical lattice with harmonic confinement. Identical fermions (blue circles) at $T = 0$ fill up the lowest energy states in the lowest band, up to a certain point where the Fermi energy ε_F exceeds the lowest energy of the first excited band, upon which the next fermions start populating this excited band. The grey shaded areas mark a qualitative band structure. The red line shows a qualitative density profile of the system, with a flat-top profile from the lowest band and a peak in the centre owing to the higher band population.

2.2.2 Fermi-Hubbard model

In this context of solids, the Hubbard model [150–152] was proposed as a simplified model to describe a single band of valence electrons in a lattice, taking dynamics (tunneling between lattice sites) and short-range electrostatic interactions into account. Hubbard's original model was described by the approximated Hamiltonian [150]

$$\hat{\mathcal{H}} = \sum_{i,j} \sum_{\sigma} T_{ij} \, \hat{c}_{i,\sigma}^{\dagger} \hat{c}_{j,\sigma} + \frac{I}{2} \sum_{i,\sigma} \hat{n}_{i,\sigma} \hat{n}_{i,-\sigma} \tag{2.6}$$

where $\hat{c}_{i,\sigma}^{\dagger}$ and $\hat{c}_{i,\sigma}$ are creation and annihilation operators for an electron of spin with sign $\sigma = \pm 1$ with a Wannier wave function $\phi(\vec{r} - \vec{R}_i)$ localised around an ion at $\vec{R}_i$. The matrix element T_{ij} describes the tunneling from site i to j and is given by a Fourier transform of the band structure:

$$T_{ij} = \frac{1}{N} \sum_{\vec{k}} \varepsilon(\vec{k}) e^{-i\vec{k} \cdot (\vec{R}_j - \vec{R}_i)} \tag{2.7}$$

where N is the number of ions.

The second term in (2.6) originates from an electrostatic interaction integral:

$$\left\langle ij \left| \frac{q^2}{r} \right| kl \right\rangle = q^2 \iint \mathrm{d}^3 r \, \mathrm{d}^3 r' \, \frac{\phi^*(\vec{r} - \vec{R}_i)\phi^*(\vec{r}\,' - \vec{R}_j)\phi(\vec{r} - \vec{R}_k)\phi(\vec{r}\,' - \vec{R}_l)}{|\vec{r} - \vec{r}\,'|} \tag{2.8}$$

whereas all integrals are neglected except for $I = \langle ii|q^2/r|ii\rangle$, which describes the interaction energy of two electrons populating the same site, and has the biggest contribution to all interactions. The Coulomb interaction between distant sites is assumed to be screened by the positively charged ions, and any long-range interaction is neglected.

The Hubbard Hamiltonian (2.6) was found to capture the essential physics in all regimes between the limit of non-interacting particles in a band structure with free tunneling motion, and the atomic limit where the electron system is insulating, even if the band in question is not filled (the so-called Mott insulating state [153, 154]).

In the context of ultracold atoms, optical lattices have enabled the study of Hubbard models in a clean and tunable environment with access to many observables on reasonable timescales [13]. The Hubbard model for bosonic particles has been studied extensively, both theoretically [89, 155, 156] and experimentally in inhomogeneous optical lattices [91, 104, 111, 112, 157, 158].

However, there are ongoing efforts to address open questions of condensed matter physics, e.g. whether the Hubbard model with electrons accommodates the essential features of high-T_c superconductivity [159, 160], for which the use of fermionic particles would be necessary. The numerical simulation of the Hubbard model poses a big challenge because of an exponential growth of Hilbert space with system size [161], and especially with fermions, the "sign problem" makes it extremely difficult to simulate certain system configurations at all [162]. This has partly motivated the study of ultracold fermions in optical lattices, which can be described by the Fermi-Hubbard model [163]:

$$\hat{\mathcal{H}}_{\mathrm{FH}} = -t \sum_{\langle i,j \rangle, \sigma} \left(\hat{a}^\dagger_{i,\sigma} \hat{a}_{j,\sigma} + \mathrm{h.c.} \right) + U \sum_i \hat{n}_{i,\uparrow} \hat{n}_{i,\downarrow} + \sum_{i,\sigma} \varepsilon_i \hat{n}_{i,\sigma} \tag{2.9}$$

where $\langle i, j \rangle$ denotes the sum over all pairs of nearest neighbours, σ denotes the spin, and the eigenvalues of $\hat{n}_{i,\sigma}$ are restricted to 0 and 1. The atoms are assumed to populate a single band.

The first term describes the tunneling, where the tunnel coupling t is assumed to be finite only for nearest neighbour tunneling. This condition holds in the tight-binding regime [133], where the particles are restricted to a single band of the lattice. The tunnel coupling t can be calculated as a matrix element in the basis of Wannier
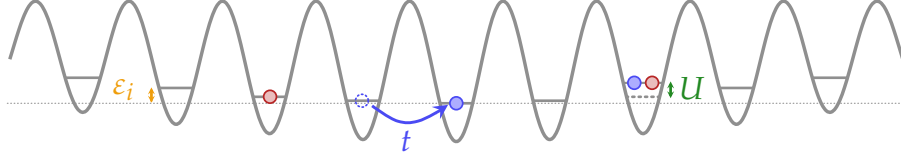
Figure 2.2: Fermi-Hubbard model. Atoms can tunnel between neighbouring sites of a lattice with a tunnel coupling t. Identical fermions are prohibited from occupying the same site, but distinguishable fermions (e.g. in different spin components) can occupy the same site, where they interact with an energy U. For real experiments in optical lattices, each site i typically has an energy offset ε_i because of the inhomogeneous lattice potential.

functions $\phi(\vec{r})$ associated with the lowest band [94]:

$$t = -\int d^3r\, \phi(\vec{r} - \vec{R}')\left[-\frac{\hbar^2\vec{\nabla}^2}{2m} + V_{\text{latt}}(\vec{r})\right]\phi(\vec{r}) \tag{2.10}$$

where $\vec{R}'$ is a vector connecting to a neighbouring site, and $V_{\text{latt}}(\vec{r})$ is the lattice potential. Here, we assume that the tunneling is the same in all directions and independent of the spin. If the band structure is known, but not the Wannier functions, the tunneling matrix element can be obtained by the same prescription as Eq. (2.7). The dependence of t on the lattice depth is exponential [13], it can thus be varied over many orders of magnitude in the experiment.

The second term in (2.9) describes the interaction. In contrast to the conventional Hubbard model (2.6), neutral atoms in optical lattices do not have mutual Coulomb interaction, but rather short-range interactions arising from s-wave collisions [164]. We therefore restrict the interaction term to pairs of atoms on the same site, which means both atoms must be in different spin states, otherwise their population of the same site in a single band would be forbidden by Pauli's principle. The interaction strength U is given by [94]:

$$U = \frac{4\pi\hbar^2 a_s}{m}\int d^3r\, |\phi(\vec{r})|^4 = g\int d^3r\, |\phi(\vec{r})|^4 \tag{2.11}$$

where m is the atomic mass and a_s is the s-wave scattering length between the different spin states. The coupling constant g appears in the pseudopotential $V(\vec{r}) = g\delta(\vec{r})$, which is used to describe the pair collisions and is a valid approximation for atoms in the sub-mK temperature range [13, 164]. As a consequence of the $|\phi|^4$ term in (2.11), the lattice depth has a slight effect on the interaction strength through the localisation of the Wannier functions [13]. Using Feshbach resonances, the interactions can be tuned over a much wider range. Though, as long as the interaction strength U

is much smaller than the gap separating the lowest from the first excited bands, the tight-binding approximation remains valid. Otherwise, the excited bands must be taken into account [94], and the single band picture of the Hubbard model breaks down.

The third term in (2.9) is not found in the original Hubbard model (2.6), and accounts for the inhomogeneity of the lattice potential via a spatially dependent energy offset ε_i on each site. Typically, the energy offsets between the nearest neighbours is small enough to be neglected in the tunneling, provided the offsets are much smaller than the local energy width of the band. This width is given by $4t$ for a single lattice axis in the tight-binding regime [13].

2.2.3   Interactions in the Fermi-Hubbard model

Interactions in the Fermi-Hubbard model give rise to many interesting phases. For the following arguments, we consider a two-component Fermi gas in a lattice at half-filling, i.e. an average of one fermion per site. The basic phenomena in Hubbard physics can be captured with a single parameter, the ratio of interaction energy to tunnel coupling U/t, which is very widely tunable in experiments, as discussed previously. For the following, a full phase diagram is shown in Fig. 2.3.

Repulsive regime $U > 0$

We first consider repulsive interactions. For small U/t, the atoms can minimise their kinetic energy by delocalising and therefore can tunnel freely through the lattice, without paying a significant energy penalty due to interactions. The system behaves as a metal. However, for large U/t, the repulsive interactions dominate over the tunneling and lead to the formation of a Mott insulator [95, 96, 165] with a single fermion per site. The density is ordered, but the spin distribution is generally random and the Mott insulator behaves as a paramagnet.

In the limit of zero tunneling, there is no mechanism that allows for reordering of spins. For weak tunneling, the energy of a spin singlet is reduced because of virtual 2$^{\text{nd}}$ order tunneling processes, where opposite spins on two neighbouring sites exchange places [94], a process forbidden for spin triplets by Pauli blocking. This "superexchange" process has a coupling strength given by $J = 4t^2/U$ [13]. If all neighbouring sites are coupled, and the temperature is lower than the superexchange energy scale $T < J$, the system undergoes a transition to an antiferromagnet. The Néel temperature T_N, at which the transition occurs, is therefore on the order of J for strong repulsion. This is typically much smaller than U, so the required temperatures and entropies to observe antiferromagnetic ordered Mott insulators are much lower than for paramagnetic Mott insulators [147, 166]. In terms of entropy, antiferromagnetic ordering is observable below a critical entropy per atom of $0.7k_B$ in 3D [147] and $0.4k_B$ in
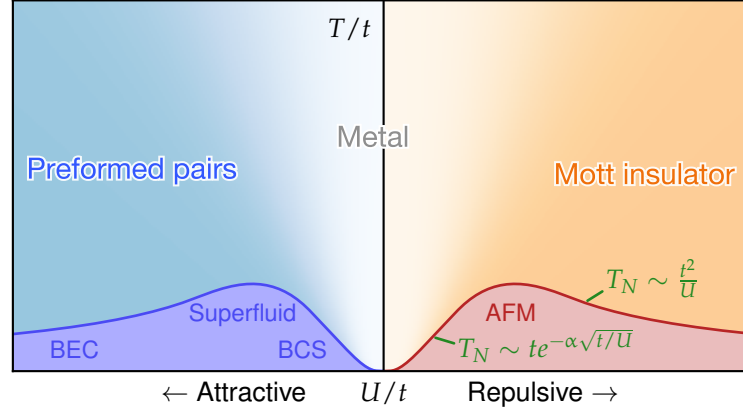
Figure 2.3: Phase diagram of the Fermi-Hubbard model at half-filling. On the repulsive side, there is a crossover from a metal to a Mott insulator for increasing U. Below the critical Néel temperature T_N, an antiferromagnet (AFM) forms. On the attractive side, non-ordered pairs can exist above the critical temperature for superfluidity. For increasing attractions at low temperatures, there is a crossover from a BCS-type superfluid to a BEC of tightly bound pairs. Phase diagram is adapted from [163].

2D [167]. Recently, short-ranged antiferromagnetic correlations have been observed with fermions in 1D chains [97] and 3D cubic lattices [98].

The cause of antiferromagnetic ordering becomes more obvious if we treat the tunneling term in second order perturbation theory in the limit $U/t \gg 1$. In this case, the Hubbard Hamiltonian can be mapped onto a Heisenberg model [168]:

$$\hat{\mathcal{H}}_{\mathrm{H}} = J \sum_{\langle i,j \rangle} \vec{S}_i \cdot \vec{S}_j, \tag{2.12}$$

with the superexchange coupling constant J as defined above. As we assumed $U > 0$ and therefore $J > 0$, we see that the Heisenberg model (2.12) favours neighbouring spins which are anti-aligned.

For strong tunneling or weak repulsive interactions, the perturbative treatment is no longer valid. Nevertheless, the antiferromagnetic order should exist for any $U > 0$. The system becomes a spin density wave below the critical temperature T_N that scales exponentially with t/U in this regime as $T_N \sim t \exp\left(-\alpha\sqrt{t/U}\right)$ [169], whereas the precise exponential scaling depends on the dimensionality of the system [170].

Attractive regime $U < 0$

The attractive regime of the Hubbard model also displays interesting phases as well. For weak attractive interactions $U < t$ at high temperatures, the system is metal-

lic. However, if the attractive interaction is much stronger than the tunnel coupling, bound pairs form on the lattice sites which behave as composite hardcore bosons. The pair can tunnel together in a second order process, with a tunnel coupling given by $\sim 4t^2/|U|$, and different bound pairs display next-neighbour repulsion given by the same energy scale [171].

At low temperatures and for weak attraction in 2D, a BCS-type superfluid is expected to form below a critical temperature T_c that scales exponentially in $t/|U|$ in the same manner as the transition temperature to the spin density wave for $U > 0$ [170]. This is due to a symmetry of the Hubbard model, where the attractive and repulsive cases are interchangeable via a particle-hole-transformation [171]. For increasingly strong attraction, the BCS pairs cross over to the strongly bound pairs, which are superfluid below a critical temperature proportional to $t^2/|U|$ [159, 170] and can undergo Bose-Einstein condensation. Due to the nearest neighbour repulsion of these pairs, the ground state is expected to be a charge density wave, forming a checkerboard pattern of doubly occupied sites and holes [171].

2.2.4   Quantum simulation prospects

The observation of the different phases of the Fermi-Hubbard model with ultracold fermions in optical lattices would represent a milestone in the field. There still remain technical challenges in achieving low enough temperatures and entropies to observe long-ranged antiferromagnetic correlations, for example. In addition to the phases of the Hubbard model at half-filling outlined above, there are other, novel phases that are expected to exist for the doped Hubbard model [160], the most prominent one being high-T_c superconductivity in cuprates. Understanding this doped regime with all its different phases remains a major theoretical challenge [172].

A possible realisation of a doped Hubbard model in ultracold Fermi gases is by preparing a spin-imbalanced gas in an optical lattice, where the excess spins play the role of dopants. Spin-imbalanced Fermi gases have generally attracted a lot of theoretical [173–175] and experimental attention [144, 176–178] in the context of superfluidity and FFLO phases [179, 180]. Whether these systems display d-wave superfluidity in a lattice is still unknown [159].

The construction of a Fermi gas microscope offers new opportunities to study the Fermi-Hubbard model in great detail, both for the spin-balanced and -imbalanced cases. Preparing Fermi gases of varying spin-imbalance poses no experimental challenge. With high-resolution imaging, we can gain access to local observables and measure correlation functions in the density and possibly spin domain, which will be instrumental in studying the Fermi-Hubbard model.

Chapter 3

Experimental setup

A large part of this work was focused on constructing an ultracold quantum gas machine, designed to image single fermionic atoms. Quantum gas microscopy is a technology that poses a considerable technical challenge. We put effort into designing the experiment to be flexible and operate with fast cycle times. To this end, we set up an all-optical scheme to produce ultracold Fermi gases using narrow-line laser cooling along other, standard techniques.

This chapter describes the hardware used in the experiment. The main properties of ^{6}Li, our atom of choice, are surveyed. The ultrahigh vacuum setup is described, as well as all laser systems used for cooling, trapping and imaging the atoms. An ultraviolet laser was constructed for a narrow-line magneto-optical trap (MOT) and is discussed in more detail. In addition, we present our techniques to generate tunable optical lattices, and detect single atoms with a dedicated optical lattice.

3.1 The atom - ^{6}Li

3.1.1 Level structure

An overview of the level structure of ^{6}Li is shown in Fig. 3.1**(a)** with the relevant fine- and hyperfine-structure levels. ^{6}Li has a $2S_{1/2}$ ground state. The principal D_1 and D_2 transitions at 671 nm lead to the excited $2P_{1/2}$ and $2P_{3/2}$ states, respectively. Both these states have natural widths of $\Gamma_{2P} = 2\pi \cdot 5.87$ MHz and therefore a radiative lifetime of $\tau_{2P} = 27.1$ ns [181]. The fine-structure splitting is small, approximately 10 GHz.

The next higher transition from the 2S to the 3P levels at 323 nm is also important as we employ laser cooling along this UV line (see Section 4.1.2). The linewidth of the $2S_{1/2} \rightarrow 3P_{3/2}$ transition is $\Gamma_{2S-3P} = 2\pi \cdot 159$ kHz, but due to an additional decay path $3P \rightarrow 3S \rightarrow 2P \rightarrow 2S$, the natural width of the $3P$ levels is broadened to $\Gamma_{3P} = 2\pi \cdot 754$ kHz [182], which is still significantly narrower than the width of the $2P$ levels. The laser setup to address the UV transition is described in Section 3.5.

The nuclear spin is $I = 1$, giving rise to hyperfine levels $F = 1/2$ and $F = 3/2$ for
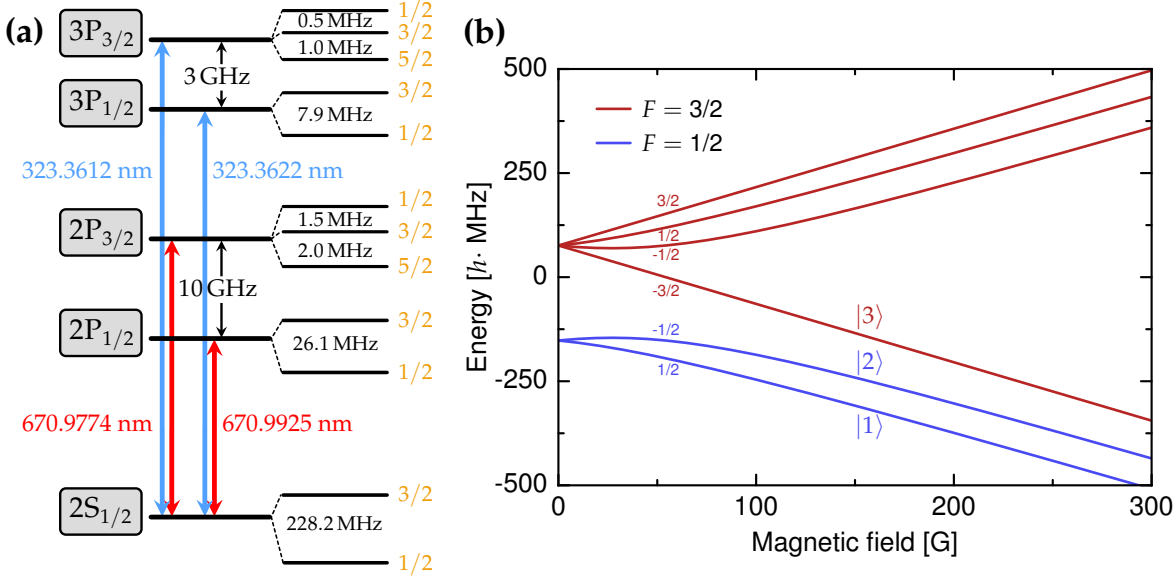
Figure 3.1: Level structure of ⁶Li. (a) Fine and hyperfine structure of ⁶Li with splittings. The $3S_{1/2}$ level is omitted. F quantum numbers are in orange. **(b)** Hyperfine structure of the $2S_{1/2}$ ground state vs. magnetic field, with denoted m_F quantum numbers.

electronic angular momentum $J = 1/2$ and $F = 1/2$, $F = 3/2$ and $F = 5/2$ for $J = 3/2$. The level splittings in Fig. 3.1**(a)** are obtained from the hyperfine constants [181, 183, 184] [1]. In the ground state, the energy splitting is $E_{HFS} = h \cdot 228.205$ MHz at zero magnetic field, which is small compared to the ground state splittings of other alkali atoms. It also means that ⁶Li enters the Paschen-Back regime for comparatively small fields: already for a few tens of G, the nuclear spin I starts to decouple from the electronic angular momentum J. Fig. 3.1**(b)** shows the energies of the ground state hyperfine sublevels for different magnetic fields, calculated by the Breit-Rabi formula [181, 185].

Due to the very weak coupling of the electronic to the nuclear spin, the hyperfine splitting of the excited levels is very small: 26.1 MHz for $2P_{1/2}$ and a few MHz for $2P_{3/2}$, less than the natural width of this level. The small splitting of the excited states prevents standard sub-Doppler cooling with the MOT beams [21]. The ratio of linewidth to splitting is marginally larger for the $3P$ levels: the splitting is comparable to the natural linewidth.

---

[1]For the higher levels, the hyperfine constants of ⁶Li can be obtained from the known values of ⁷Li in [184] by scaling them with the ratio of the nuclear g-factors $g_I(^6\text{Li})/g_I(^7\text{Li}) = 0.822/2.171$.
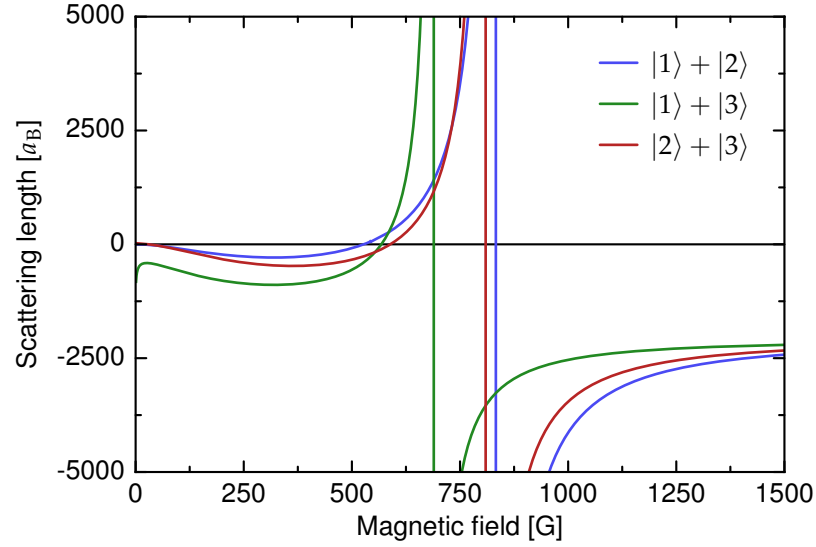
Figure 3.2: Feshbach resonances between the three lowest hyperfine sublevels of ^{6}Li. Data is taken from supplemental material of [186].

3.1.2 Feshbach resonances

^{6}Li has extremely broad Feshbach resonances [48]. For each pair of the three energetically lowest hyperfine sublevels $|F = 1/2, m_F = \pm 1/2\rangle$ and $|F = 3/2, m_F = -3/2\rangle$, there exists one broad Feshbach resonance of a few hundred Gauss width [186] (shown in Fig. 3.2). These three sublevels are commonly denoted by $|1\rangle$, $|2\rangle$ and $|3\rangle$, respectively. For our experiments, we mainly use a mixture of the $|1\rangle$ and $|2\rangle$ states. The scattering length of this mixture practically vanishes at zero field and displays a local minimum of $-290a_B$ at a field of 320 G, which gives a sufficiently high scattering rate for efficient evaporative cooling with very few inelastic losses. There is a narrow Feshbach resonance of 0.1 G width at 543 G [187] and the broad Feshbach resonance is located at 832 G with a width of around 300 G.

3.1.3 Advantages and disadvantages of ^{6}Li

For quantum gas experiments using fermionic alkali atoms, the choice is limited to ^{6}Li and ^{40}K. Both species have their merits and have proven to be successful candidates for quantum gas microscopy [127–131]. Our choice of ^{6}Li stemmed from different considerations.

The light mass of ^{6}Li allows for very fast tunneling timescales in an optical lattice. Experiments that rely on superexchange interaction can be performed with large coupling rates as these scale as the square of the tunneling matrix element ($J = 4t^2/U$).

We can also afford to work with optical lattices of large lattice constants, while still maintaining fast enough tunneling for studying strongly correlated systems. Large spacings give a big advantage in optically resolving and addressing single sites. Also, the very broad Feshbach resonances of a few hundred G width allow for straightforward tuning of interactions in the lattice. They are much broader than the Feshbach resonances of ^{40}K, which have widths smaller than $10\,$G [188].

In addition, the ground state level structure of ^{6}Li is much simpler than ^{40}K and offers an $F = 1/2$ hyperfine level, which is a natural spin-1/2 system. In general, the level structure of ^{6}Li is convenient for laser setups as all level splittings are small enough to be in reach of offset locks and standard acousto-optic modulators (AOM). The $2P$ fine-structure splitting of $10\,$GHz is convenient because one can use the same laser type and optics for addressing both the D_1 and D_2 lines.

The small fine and hyperfine splittings have advantages and disadvantages for two-photon processes that couple $F = 1/2$ and $F = 3/2$ in the ground state. The small hyperfine splitting makes it easy to produce two Raman photons with a single laser and an AOM. However, as the excited levels $2P_{1/2}$ and $2P_{3/2}$ have opposite hyperfine shifts, the contribution of both D_1 and D_2 lines interfere destructively as soon as the one-photon detuning of the Raman beams is larger than the fine-structure splitting of $10\,$GHz, setting a limit to the two-photon coupling rate relative to the off-resonant scattering rate [189].

The disadvantages of using ^{6}Li are closely related to their advantages: the light mass makes the task of fluorescence imaging for quantum gas microscopy very challenging. To suppress the rapid tunneling, the lattice requires an exceptionally large depth. Furthermore, the $671\,$nm photons used for imaging impart a very large recoil energy onto the atoms:

$$E_{\text{rec}} = \frac{h^2}{2m\lambda^2} \approx h \cdot 74\,\text{kHz} \tag{3.1}$$

For a good signal-to-noise ratio, each atom needs to scatter several thousands of photons while staying on the same lattice site. This demands a very efficient cooling mechanism to carry away the large recoil energy, before the atom starts to tunnel or is lost. However, the level structure of ^{6}Li, albeit simple, provides practically no cycling optical transitions due to the small hyperfine splittings in the excited state. This makes laser cooling and manipulation of the atoms challenging.

Cooling mechanisms that have been used successfully for fluorescence imaging of single atoms such as optical molasses [110, 111] and EIT cooling [127, 130, 190, 191] do not work for ^{6}Li. Raman sideband cooling [192–194] has proven to give enough cooling power for imaging single atoms of ^{6}Li with high fidelity [129, 131]. But even here, the efficiency is reduced compared to other atomic species, owing to the strong off-resonant scattering for a given Raman coupling strength [189].

3.2 Vacuum setup

Our ultrahigh vacuum system consists of an oven for providing atomic vapour, a Zeeman slower, a MOT chamber and a glass cell. Two titanium sublimation pumps and two ion getter pumps (VacIon Plus 55/75 Starcell by Varian) maintain a sufficiently low vacuum pressure on the order of 10^{-10} mbar in the oven section and a few 10^{-11} mbar in the experimental chambers. An overview of the setup is shown in Fig. 3.3.

3.2.1 Atom source and Zeeman slower

The atom source consists of a steel oven containing a few grams of lithium. We heat the oven to $380°$C to reach an appreciable vapour pressure [181]. The atoms effuse out of the oven towards the Zeeman slower and MOT chamber via an aperture of 1 cm diameter. A large water-cooled pipe of aluminium is mounted around the oven to prevent convection of hot air into the experimental setup and remove the heat from the table.

The Zeeman slower consists of a differential pumping tube surrounded by the inhomogeneous magnetic coils [195]. We use copper wire with a Kapton insulation layer and a hollow core for direct water cooling of the coils. The Zeeman field merges smoothly into the MOT gradient, which allows for a more compact setup and a small impact of the atom beam divergence (for more details, see [196]). The decelerating laser beam enters through a viewport on the far end of the vacuum system, which we heat to $90°$C to prevent the lithium from sticking to the window and rendering it opaque.

3.2.2 Science chambers

Our MOT chamber is a nonmagnetic steel octagon chamber by Kimball Physics. It has four standard CF40 silica viewports from the side for the MOT beams, and two reentrant silica viewports along the vertical direction for housing magnetic coils close to the atoms.

The quadrupole MOT coils are located outside the chamber and consist of four layers, each of four windings. The wire is the same as the Zeeman coils. Inside the reentrant viewports, we have another set of coils which served as a quadrupole magnetic trap for a mixture of ^{6}Li/^{7}Li in the past [197]. As the evaporative cooling scheme in this magnetic trap performed very badly, we replaced this stage with narrow-line laser cooling using the setup described in Section 3.5. From then on, we switched the old magnetic trap coils from a quadrupole configuration to a homogeneous one for tuning the scattering length in optical traps.
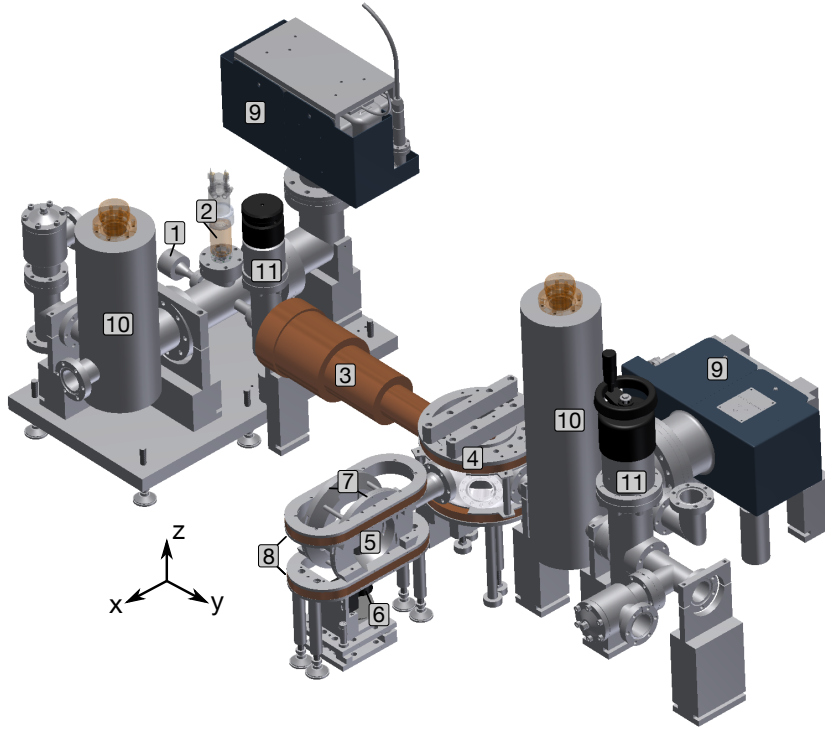
Figure 3.3: Vacuum system. 1: Oven. **2:** Atom beam shutter. **3:** Zeeman slower. **4:** MOT chamber. **5:** Glass cell. **6:** Microscope objective mount. **7:** Feshbach and gradient coils. **8:** Vertical gradient coils. **9:** Ion pumps. **10:** Titanium sublimation pumps. **11:** Gate valves.

The main experiments take place outside the MOT chamber. In order to have good optical access and avoid problems with eddy currents while switching magnetic fields, we use a vacuum glass cell (by Hellma Analytics). It has 4 mm thick walls made of Spectrosil glass and measures 40 mm by 34 mm on the outer edges. It is specified to have a wavefront deformation of less than $\lambda/2$ over a diameter of 25 mm at a wavelength of 633 nm. For reasons of manufacturing, the glass cell has no anti-reflection coatings to ensure this surface flatness.

3.2.3 Magnetic fields

The glass cell is surrounded by an arrangement of magnetic coils. Two vertical "race-track" coils produce quadrupole fields for applying vertical magnetic gradients. The coils are not mounted symmetrically around the atoms, but the upper coil is raised by 1 cm to pull the quadrupole field centre away from the atoms. This provides a more homogeneous vertical gradient with little transverse variation of the field.

Two further pairs of coils are mounted along the horizontal y-axis: a small coil pair of four windings each for applying transverse gradient fields, and another Feshbach coil pair with a staircaselike cross section, where each winding pair is in Helmholtz configuration. These coils produce the fields for tuning the scattering length via Feshbach resonances. Both the transverse gradient and Feshbach coils are housed in a solid mount of PEEK thermoplastic.

The Feshbach and vertical gradient fields are each stabilised using a precision flux-gate current sensor (IT 700-SB by LEM) and a feedback loop to four power MOS-FETs (SKM111AR by Semikron) that regulate the current from the power supply. An insulated-gate bipolar transistor (SKM600GA12T4 by Semikron) in the current path is used to enable or disable the current altogether. This system is described in more detail in [197].

The glass cell is surrounded by a large aluminium frame carrying three pairs of compensation coils for cancelling the magnetic field of the Earth. These are driven by high-power operational amplifiers (DCP260/30 by ServoWatt) that can run up to $\pm 10\,$A of current. In addition, we have coils of solid wire outside of every viewport around the MOT chamber for applying small bias fields of up to a few Gauss to the atoms inside.

Two radio-frequency (RF) antennae are fixed near the glass cell for driving magnetic transitions between hyperfine sublevels. The antennae are made from standard RG58 cable tied to a loop with the shielding removed around the loop circumference. One of the antennae is around the glass cell itself with the loop axis pointing along the x-direction, the long axis of the glass cell. The other antenna is above the cell with its axis pointing downwards.

3.3   Imaging

The main feature of this experiment is the ability to optically resolve single fermions. The centrepiece of the setup is the high-resolution microscope objective mounted beneath the glass cell. This objective is used for projecting in some of the physics lattice beams (described later in Section 3.8) and gathering the photons scattered by the atoms during fluorescence imaging. We mounted the objective onto a nanopositioning linear stage (PIFOC N-725.1A by PI) for precise focusing onto the atoms.

Our objective, shown in Fig. 3.4, is custom made by Special Optics. It has a numerical aperture (NA) of 0.5 and an effective focal length of 28.1 mm, whereas the chromatic shift between this imaging wavelength and the lattice wavelength of 1064 nm is corrected by design. Its theoretical resolution is $\Delta r = 0.82\,\mu$m at the imaging wavelength of 671 nm, according to the Rayleigh criterion: for an imaged point source, Δr
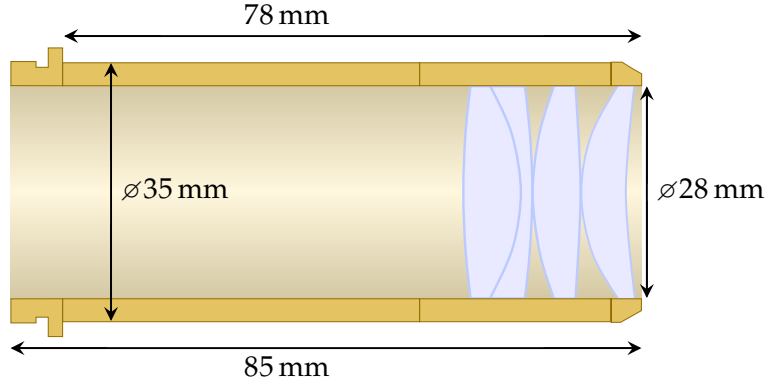
Figure 3.4: Cross section of the custom high-resolution objective. The NA is 0.5 and the effective focal length is 28.1 mm.

specifies the distance between the centre of the Airy disk to the first minimum [198]. A Gaussian function approximated to the point-spread-function (PSF) has a standard deviation of $\sigma_{\mathrm{PSF}} \approx 0.29\,\mu\mathrm{m}$ [199]. To avoid eddy currents while switching magnetic fields, the objective housing is made from Ultem thermoplastic.

The photons emitted by the atoms are collimated by the objective and steered via several mirrors onto a lens of 1700 mm focal length, which focuses the image onto an electron multiplied CCD camera (EMCCD, ProEM1024 by Princeton Instruments). This camera has a quantum efficiency of 95% at the imaging wavelength of 671 nm.

A second, identical objective from the top enables us to pick up the physics lattice beams from below after they have left the system and image them onto a camera. This gives us the unique ability to directly measure our lattice intensity pattern and correct for any errors or drifts that may arise. It also offers the possibility to project in further light potentials from the top.

For basic measurements on atom clouds, such as atom numbers, temperatures and cloud positions, we rely on absorption imaging. Three axes of imaging provide spatial information for aligning traps and different levels of sensitivity. For each axis, we image a resonant absorption beam onto a CCD camera (Manta G-145B NIR by Allied Vision).

One of the imaging axes is along the glass cell (x-direction) with a magnification of 0.8. The image plane is in the glass cell, however the imaged clouds in the MOT chamber are typically large and dense enough to be imaged even out of focus. Nevertheless, an extra, removable lens can be quickly installed in the imaging path to shift the focus plane into the MOT chamber and image with a magnification of 0.7.

The second imaging axis is along the horizontal direction perpendicular to the glass cell (y-direction). Using a high-NA lens at the side of the glass cell, we get a

magnification of 10.

The third imaging axis is along the vertical z-direction in the glass cell, through the high-resolution objective. Instead of using the 1700 mm and EMCCD camera, a detachable mirror is used to divert the absorption signal onto a separate lens and camera with a magnification of 2.

3.4   671 **nm laser setup**

We operate a dedicated optical table for all lasers running at 671 nm used to cool, trap and image the atoms. All lasers running at this wavelength are external cavity diode lasers (ECDL, DL100 Pro Design by Toptica). Each relevant frequency for cooling and imaging is within a sufficiently small frequency range from the D_2 line of ^{6}Li, such that we can use a single laser as a frequency reference for the whole table. Part of this master laser beam goes to a standard Doppler-free saturation spectroscopy [200] in a lithium heat pipe. A reservoir of lithium is heated to 400°C to produce a vapour in the centre. An EOM is used to generate sidebands, which we use for electronic feedback to stabilise the laser frequency to the ground-state crossover line of ^{6}Li. A sketch of the setup is shown in Fig. 3.5(a).

All other lasers are of the same type as the master laser. To stabilise their frequencies, part of their beams (< 1 mW) is split off and overlapped with a fraction of the master laser beam on a fast photodetector (ET-4000 by EOT). We compare the detected beat signal between the two lasers to a reference frequency and then feed back the deviation as an error signal to the corresponding slave laser using a PI controller. We use the following lasers:

- One "cooling" laser, running on the $|2S_{1/2}, F = 3/2\rangle \rightarrow |2P_{3/2}, F'\rangle$ transition (F' is undetermined as the hyperfine structure of the upper state is unresolved).

- One "D_2 repumper" laser, running on the $|2S_{1/2}, F = 1/2\rangle \rightarrow |2P_{3/2}, F'\rangle$ line.

- One "D_1 repumper" laser, running on the $|2S_{1/2}, F = 1/2\rangle \rightarrow |2P_{1/2}, F = 3/2\rangle$ line.

- One "Zeeman slower", red-detuned to the $|2S_{1/2}, F = 3/2\rangle \rightarrow |2P_{3/2}, F'\rangle$ cooling transition by 100 MHz. This is an ECDL seeding a tapered amplifier.

- One "imaging" laser, resonant to the transition on which the cooling laser is running.

The "cooling" and "D_2 repumper" lasers each seed a tapered amplifier chip to obtain more power for the laser cooling. The two amplifier beams are overlapped and
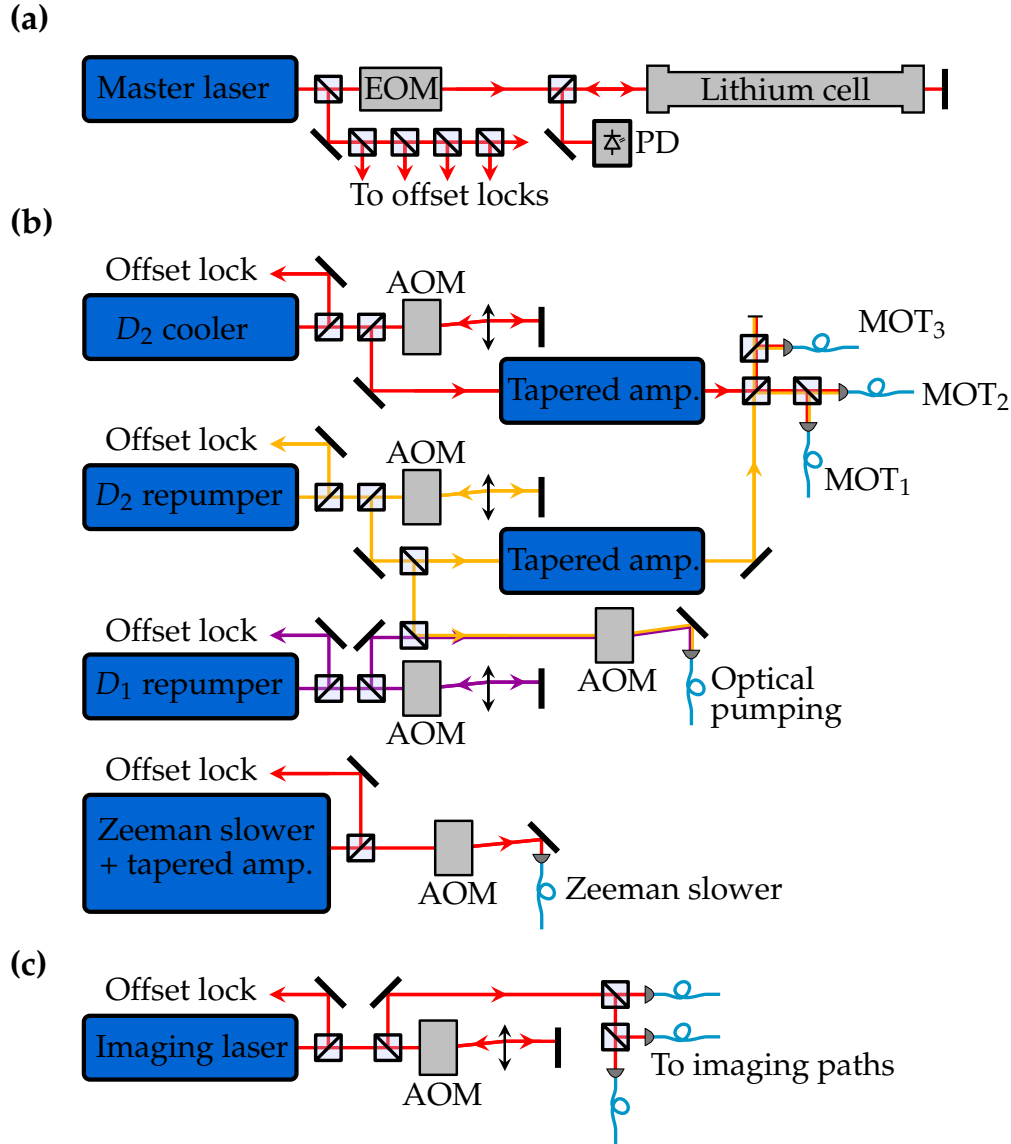
Figure 3.5: 671 **nm laser setup.** Most optical elements (lenses, waveplates and mirrors) are omitted for simplicity. **(a)** Master laser setup. The beam passes twice through a homemade ^{6}Li vapour cell. An EOM imprints sidebands on the beam for frequency stabilisation. Several beamsplitters divert parts of the beam to offset lock setups. **(b)** Laser cooling setup. Four lasers provide frequencies for laser cooling, repumping along the D_1 and D_2 lines, and Zeeman slowing. A fraction of power is split off from each beam and overlapped with the master laser beam for offset locking. The cooler and repumper lasers have their powers switched and controlled by double-pass AOM setups. Two tapered amplifiers provide the necessary power for the MOT. The two frequencies are combined and distributed among three fibres for the MOT axes. **(c)** Imaging laser setup. The laser is offset locked to the master laser. The power is switched by an AOM and distributed among three fibres for different imaging axes. Three shutters (not shown) are used to choose the imaging axis.

split into four different paths. Three of these are coupled into single-mode fibres leading to the different MOT ports. An overview of the setup is shown in Fig. 3.5**(b)**.

The two repumpers are overlapped and split off to a separate fibre which is used for optical pumping in the glass cell. The D_2 repumper is used for transferring the atoms from the $F = 1/2$ ground-state sublevels back into the $F = 3/2$ ones during absorption imaging. The D_1 repumper, on the other hand, is used for the Raman sideband cooling, described in Chapter 5.

The imaging laser is used exclusively for absorption imaging in both the MOT chamber and the glass cell. An AOM is used to switch on the laser power, which is then coupled into separate optical fibres for the three imaging axes described in Section 3.3. The setup is sketched in Fig. 3.5**(c)**.

3.5 Ultraviolet laser

A special feature of our experiment is the narrow-line laser cooling of ^{6}Li along the $2S_{1/2} \to 3P_{3/2}$ transition at an ultraviolet (UV) wavelength of 323.36 nm, where the excited state has a decay rate of $\Gamma_{3P} = 2\pi \cdot 754$ kHz. Laser cooling of atoms on narrow transitions allows for achieving lower temperatures and boosting the phase-space density, as described in [182, 201, 202]. It provides an alternative scheme to recently developed sub-Doppler cooling via grey molasses on the D_1 line, which was demonstrated for ^{6}Li, ^{7}Li, ^{39}K and ^{40}K [203–207].

There are no direct narrowband UV sources at 323 nm, therefore we must rely on frequency conversion using nonlinear crystals to obtain this wavelength. UV lasers that rely on second-harmonic generation (SHG) of semiconductor lasers at 646 nm are offered as a commercial solution, but the laser diodes and amplifier chips are limited in power. A natural choice to overcome this is using a dye laser for generation of 646 nm light with high spectral purity and sufficiently high power. However, this solution requires intensive maintenance and achieving laser linewidths below 100 kHz is challenging.

To circumvent these limitations, we developed a turnkey laser system very similar to those in [208, 209] to generate UV light via two successive nonlinear conversion processes: the 646 nm light is obtained via sum-frequency generation (SFG) of two infrared wavelengths. The second harmonic of this light is subsequently generated in a resonant doubling cavity. By stabilising the visible subharmonic to a transition of molecular iodine, we fix the frequency of the UV light.

3.5.1   Laser sources

The generation of UV starts from two infrared wavelengths. We use a single-frequency laser (Orion laser source by RIO) at 1550 nm and a fibre laser at 1110 nm (Koheras Adjustik Y10 by NKT Photonics). While the 1550 nm laser remains free running, the 1110 nm fibre laser is equipped with a fast piezo actuator for modulating the frequency, used later for overall frequency stabilisation.

The 1550 nm light is amplified using an erbium-doped fibre amplifier (Nufern NUA-1550-PB-0005), rated at 5 W of output power. We use a similar, ytterbium-doped fibre amplifier (Nufern NUA-1100-PB-0005) to amplify the light at 1110 nm. As this wavelength is on the edge of the amplifier emission profile, the gain needs to be very high, leading to a strong sensitivity to back-reflections into the output fibre. Therefore, we operate the amplifier below 2 W instead of the rated 5 W, limiting the achievable power in our system.

3.5.2   Sum-frequency generation (SFG)

The two infrared beams are overlapped and focused through a magnesium oxide doped periodically poled lithium niobate (MgO:PPLN) crystal of 40 mm length and a poling periodicity of 12.3 μm (Fig. 3.6). The sum frequency at 646.72 nm is generated via quasi-phase-matching [210, 211]. For our parameters, we need to operate the crystal at 65.20(1)°C inside a temperature-stabilised oven (OC1 by Covesion). The PPLN has a triple-band anti-reflection coating for both infrared wavelengths and the visible output.

To obtain the best conversion efficiency, we apply a Boyd-Kleinman optimisation [212], a general method to determine the optimal beam parameters for maximising the conversion output. In particular, one optimises the ratio between the crystal length l and the confocal parameter $2z_0$:

$$\xi = \frac{l}{2z_0}; \qquad z_0 = \frac{n\pi w_0^2}{\lambda} \tag{3.2}$$

where z_0 is the Rayleigh length, λ is the wavelength of the incoming radiation, w_0 is the $1/e^2$ radius at the focus, and n is the effective refractive index along the propagation direction. A thorough treatment of the Boyd-Kleinman theory is found in [213].

For periodically poled crystals, where the effects of Poynting vector walk-off are cancelled, the optimal value is found at $\xi = 2.836$ for both input beams [213, 214]. As we are dealing with two input wavelengths that have the same optimal confocal parameter $2z_0$, this necessarily means that both beams need different focus waists (33.4 μm for 1110 nm and 39.8 μm for 1550 nm). For each beam, we use different combinations of lenses to achieve the respective waist size.
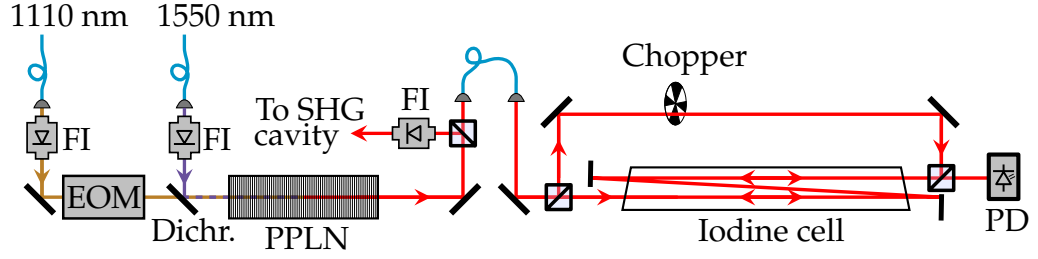
Figure 3.6: Scheme of the SFG setup. The sum frequency of two infrared wavelengths is generated in a PPLN crystal. For frequency locking, sidebands are imprinted onto the light using an EOM. Both infrared lasers and the SFG output are protected from back-reflections by Faraday isolators (FI). Part of the SFG output is coupled into a fibre leading to an iodine spectroscopy setup. The pump beam is chopped for lock-in detection of the spectroscopy signals. To tune the frequency of the Doppler-free iodine line, the pump frequency is shifted with two AOMs (not shown), one of which replaces the chopper (see Section 3.6.3).

We found that for 4 W input power at 1550 nm and 1.6 W at 1110 nm we could get up to 800mW of continuous red power, which is very close to the efficiency limit reported elsewhere [208].

3.5.3 Frequency-doubling cavity

The visible output of the SFG process is coupled into a resonant bow-tie cavity for second-harmonic generation in a barium borate (β-BBO) crystal. Here, we rely on critical phase-matching, where the phase velocity of the fundamental frequency ω is matched to that of the second harmonic at 2ω. This is done by tilting the principal crystal axis by 37° with respect to the direction of light propagation and exploiting the birefringence to match the two refractive indices $n(\omega)$ and $n(2\omega)$.

The cavity design is sketched in Fig. 3.7. Its housing is machined from a single block of aluminium and the four mirror mounts with alignment screws are integrated into the cavity walls. The input mirror M1 is flat and has 98% reflectivity at 646 nm for impedance matching, i.e. the transmission is matched to the intrinsic cavity losses, which leads to very efficient cavity coupling [215, 216]. Mirror M2 is flat and glued onto a small piezo actuator. It is attached to a hollow copper cone filled with a tin-lead alloy, which shifts the centre of mass away from the piezo, allowing for larger bandwidths [217]. The small piezo has its mechanical resonance at 80 kHz, including the mirror, so fast feedback on the cavity length is possible. As an alignment aid, two iris diaphragms are mounted on an optical rail between M1 and M2 to define the long cavity arm.

Mirrors M3 and M4 are both concave with a curvature radius of $R = 75$ mm in
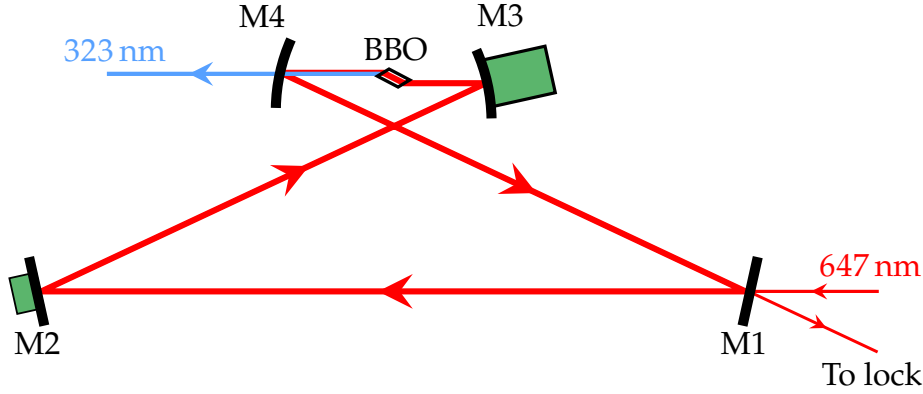
Figure 3.7: Schematic of the SHG cavity. The mirrors M2-4 are high-reflective for 646 nm, whereas M1 has 98% reflectivity for impedance matching. M4 is also coated to be highly transmissive for 323 nm. M3 is glued onto a piezo tube for scanning and stabilising the cavity length. M2 is glued onto a small piezo stack for fast feedback.

order to focus the light through the crystal with a waist of 20.1 μm. M3 is glued onto a large piezo tube for scanning the cavity length and for slow feedback. M4 is coated to be highly transmissive for the UV light.

The BBO crystal is 10 mm long and Brewster cut with an angle of 56.1°, in order to minimise losses of the incoming p-polarised light. It is enclosed by a copper block from four sides with a small air gap to prevent crystal damage due to the anisotropic thermal expansion of BBO. The crystal is temperature stabilised to 65°C by the heat dissipation of a high-power resistor attached to the top of the copper mount. A combination of translation and tilt stages provides six degrees of freedom for positioning and aligning the crystal with respect to the incoming focused beam. Detailed calculations of this cavity design are found in [218].

The cavity length is stabilised to the visible input light using the Pound-Drever-Hall method [219, 220]. We first imprint sidebands onto the 1110nm light using a resonant lithium niobate EOM (Fig. 3.6). These sidebands are transferred to the visible light due to the sufficiently large bandwidth of the SFG process. We monitor the back reflection from the cavity input mirror M1 using a fast photodetector (PDA10A-EC from Thorlabs) and demodulate the signal to obtain an error signal for feeding back to both movable cavity mirrors using a PI controller.

To preserve the lifetime of the mirrors and the doubling crystal, we implemented an automatic cavity lock for stabilising the cavity to a resonance using a remote TTL signal. Thus, the cavity is only enabled when the light is needed in the experimental sequence. A photodetector after the cavity detects the transmission of the visible light on resonance. Upon triggering the lock, the piezo voltage is ramped until a resonance is detected. A logic circuit converts the signal into a TTL pulse that is used to enable the servo loop and lock the cavity.
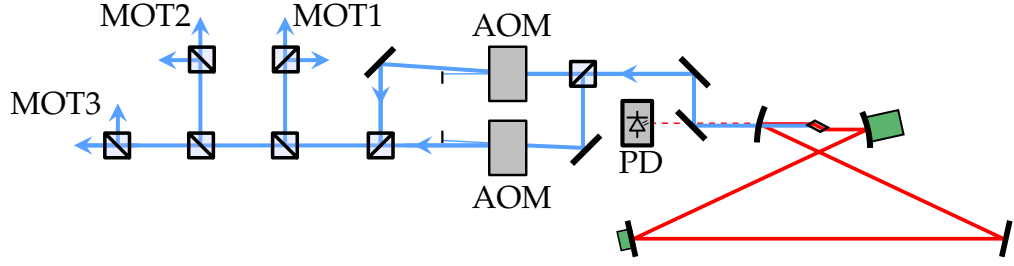
Figure 3.8: Scheme of UV optics setup. The photodetector (PD) is used to detect transmission of 646 nm on cavity resonances for automatic locking. Both AOMs diffract in opposite orders to produce the frequencies for cooling and repumping. Most optical elements (lenses, waveplates and mirrors) are omitted for simplicity.

Despite the absence of any perpendicular surface in the cavity, we observed back-reflections in the doubling crystal, possibly due to non-linear refractive index modulation caused by the high circulating power. The photons interfered with the incoupled light, causing power instability. Therefore, we required a Faraday isolator between the SFG crystal and SHG cavity, which solved the problem but reduced the available 646 nm power. At the time where we had 800 mW of incoming visible light, we could produce up to 280 mW of UV power. Due to slowly diminishing infrared power over a few years, as well as PPLN and BBO degradation, at the time of writing we are currently operating at 300 mW of red power and 30 mW of UV. This can be remedied by replacing the crystals or the infrared amplifiers. However, for the purpose of laser cooling, this power level is still sufficient.

3.5.4 UV optics setup

The optical setup after the UV cavity is designed for a free-space 3D MOT setup with two optical frequencies for cooling and repumping on the UV transition. A simplified schematic is shown in Fig. 3.8. First, the SHG cavity output is split into two paths. One beam is shifted by $+114$ MHz and the other by -114 MHz using quartz AOMs (I-M110-3C10BB-3-GH27 by Gooch and Housego). This is to address both hyperfine levels of the $2S_{1/2}$ ground state. Both beams are then overlapped again without losses on a polarising beam splitter (PBS) and expanded using a $1:4$ telescope to a beam waist of $w \approx 6.5$ mm.

The combined frequencies are split into two arms of equal power and rectified polarisations using a PBS. One of the two arms is then further split into equal parts. Each of these three arms is then split again into two beams, resulting in six beams for the UV MOT with a power ratio of $2:2:1:1:1:1$. The strongest two beams are used for the vertical MOT axis, along which the magnetic gradient is stronger by a factor of 2. The four remaining beams are guided to the horizontal MOT ports.

3.6 Iodine spectroscopy

The automatic cavity lock is incompatible with using a lithium reference to directly stabilise the UV laser frequency to the $2S_{1/2} \rightarrow 3P_{3/2}$ transition as the UV light is absent for the largest part of the experimental cycle. Nevertheless, as the narrow linewidth of the UV transition of ^{6}Li demands a high degree of frequency stability, it is important to use a stable atomic reference. To address this issue, we stabilise the visible SFG output to a transition of molecular iodine (^{127}I$_2$) due to an abundance of lines [221]. In fact, there is one transition which almost coincides with the ^{6}Li UV line.

3.6.1 Iodine transitions

The resonance frequency of the $2S_{1/2} \rightarrow 3P_{3/2}$ transition is at 927.113357 THz [222], so the subharmonic needs to run at 463.556679 THz. ^{127}I$_2$ has a coarse structure transition at $15462.6074\,\mathrm{cm}^{-1} = 463.557308$ THz [221], which is only 629 MHz away from the necessary subharmonic frequency. However, we need high-resolution spectroscopy to identify any potential lines that might lie much closer to the UV transition.

We couple part of the 646 nm light into a single-mode fibre to a different setup, where we perform Doppler-free saturation spectroscopy in an iodine gas cell (Fig. 3.6). The iodine transitions at the required wavelength are very weak. To boost the signal, we use a 30 cm long gas cell and send the beams three times through to cell to increase the interaction length in the gas. But even then, the spectroscopy signal is too weak to be detected directly. Therefore, we need lock-in detection to observe the different lines. At first, the pump beam was separated from the probe beam before entering the cell and chopped at kHz frequencies using an optical chopper, while the probe beam signal was detected with a photodetector (PDA10A-EC by Thorlabs).

The Doppler-free signals measured by the photodetector were demodulated and integrated in a lock-in amplifier to extract them from the noise (Fig. 3.9(b)). We found several transitions in the direct vicinity of the required subharmonic frequency, as verified by a wavemeter. Using IodineSpec5 [223], a program to calculate iodine spectra, we found that the measured hyperfine structure agrees well with calculations (Fig. 3.9(a) and 3.9(b)), and identified all the observed hyperfine components as belonging to the $|X^1\Sigma_{0g}^+, v = 4, J = 46\rangle \rightarrow |B^3\Pi_{0u}^+, v' = 5, J' = 45\rangle$ line[2] of ^{127}I$_2$.

---

[2]The prefix X denotes the singlet electronic ground state and B the second singlet excited state. The superscripts 1 and 3 describe the multiplicities $2S + 1$ of the total electron spin. The projection Λ of the orbital angular momentum onto the axis between both nuclei is given by Σ ($\Lambda = 0$) or Π ($\Lambda = 1$). The subscript 0 refers to the projection Ω of the total electronic angular momentum onto the axis. The inversion symmetry of the electron wave functions is given as even (g) or odd (u). The superscript $+$ denotes even parity with respect to reflection by a perpendicular plane between the two nuclei. Finally, v and J denote the vibrational and rotational quantum number of the molecule, respectively.
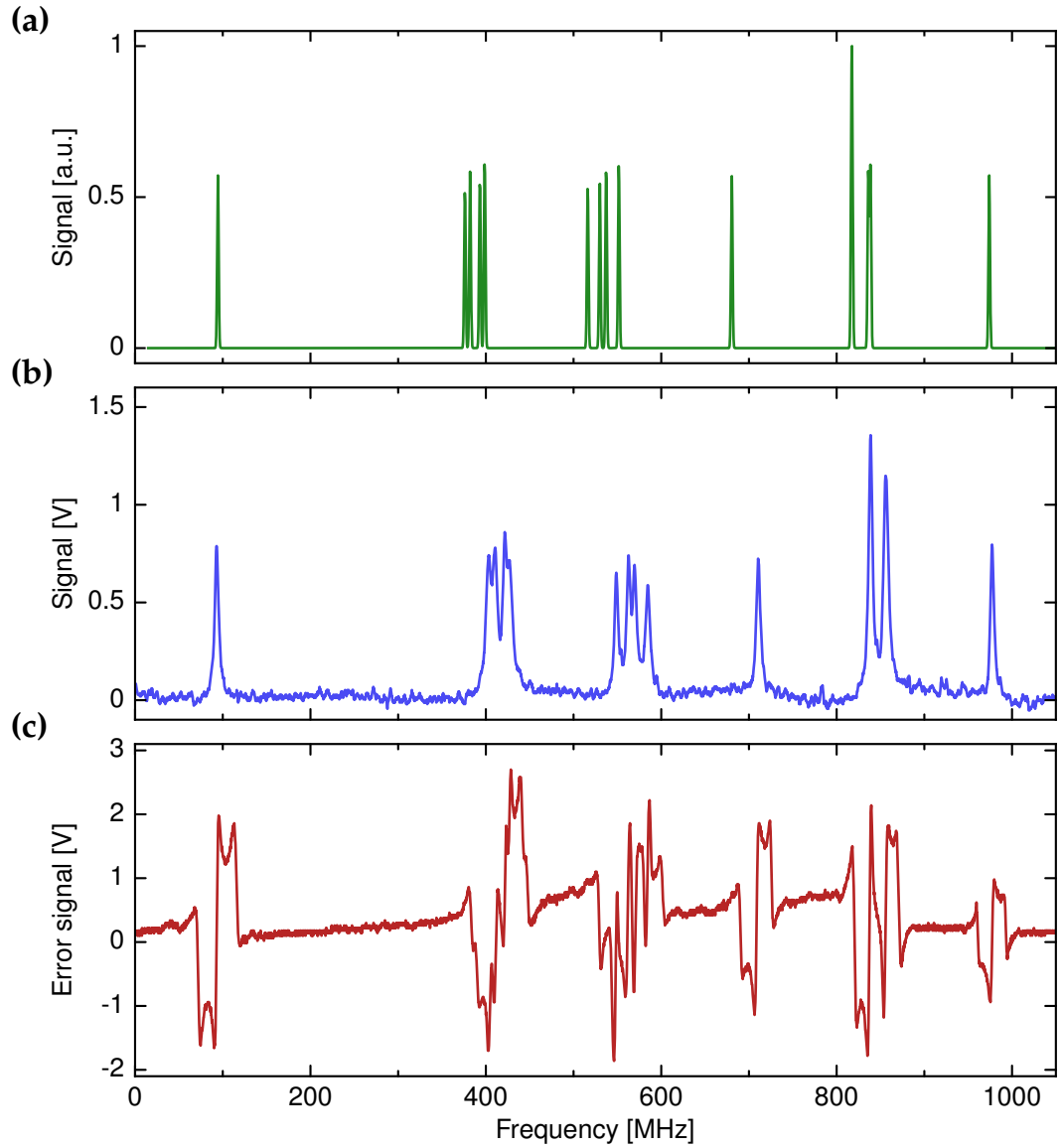
Figure 3.9: Iodine spectroscopy. (a) Simulation of hyperfine structure of $^{127}I_2$ around in the relevant frequency range (463.5565 THz) using IodineSpec [223]. **(b)** Doppler-free spectroscopy signal measured by lock-in detection and a frequency scan of 60 s. The mismatch of the measured line positions and the simulation is probably due to frequency drifts of the laser during the slow scan. The frequency axis on the measured data was calibrated using a wavemeter by measuring the position of the two outermost lines. **(c)** Error signal, obtained by demodulation of the photodetector signal and subsequent lock-in detection. We stabilise the frequency to the left-most hyperfine component.

Of the detected lines from the spectrum in Fig. 3.9**(b)**, the isolated line farthest to the left was the closest to the required frequency. Furthermore, it displayed no measurable sensitivity to external magnetic fields, making it a very suitable candidate for a stable frequency reference.

3.6.2 Error signal generation

To generate an error signal for frequency stabilisation, we make use of the same sidebands used for locking the SHG cavity. The probe beam photodetector signal is first sent through a wideband double-balanced RF mixer for demodulation at the EOM modulation frequency ν_{EOM} with the correct phase to generate an error signal. As the pump beam is being chopped at a frequency ν_{chop}, the error signal undergoes a full amplitude modulation at ν_{chop} as well. By sending this signal through a lock-in amplifier, we can extract the error signal with almost no background and a large signal-to-noise ratio (Fig. 3.9**(c)**).

The strong signal obtained by this method comes at the cost of loop bandwidth of the frequency lock, due to the narrow-band filter stage in the lock-in amplifier. However, the requirement of large bandwidths for this frequency stabilisation is relaxed by the inherently narrow linewidth and passive stability of our infrared seed lasers.

3.6.3 Frequency calibration and stabilisation

The detected iodine transitions all lie at different frequencies than the one needed for UV cooling. Fortunately, the nearest transition is close enough that we can eliminate the frequency gap by detuning the pump and probe beams with respect to each other.

$$\omega_{pr} = \omega_0 + \delta \qquad\qquad v \qquad \omega_{pu} = \omega_0 + \delta + \Delta$$
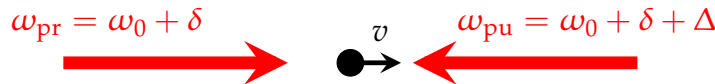
Consider a near-resonant probe beam traveling through a gas of particles with a frequency $\omega_{pr} = \omega_0 + \delta$, where ω_0 is the lab-frame resonant transition frequency of a particle and δ is the detuning. Consider also a counterpropagating pump beam with a frequency offset of Δ with respect to the probe beam, i.e. $\omega_{pu} = \omega_0 + \delta + \Delta$ (see figure above). A particle traveling with a velocity v towards the pump beam will see Doppler-shifted frequencies:

$$\begin{aligned}
\omega'_{pu} &= \left(1 + \frac{v}{c}\right)\omega_{pu} = \left(1 + \frac{v}{c}\right)(\omega_0 + \delta + \Delta) \\
\omega'_{pr} &= \left(1 - \frac{v}{c}\right)\omega_{pr} = \left(1 - \frac{v}{c}\right)(\omega_0 + \delta)
\end{aligned} \tag{3.3}$$

We can resolve the system of equations (3.3) to determine the necessary probe

beam detuning δ for the particle to resonantly interact with both beams simultaneously, i.e. $\omega'_{pu} = \omega'_{pr} \stackrel{!}{=} \omega_0$.

$$\delta = \frac{-\Delta\left(1 + \frac{v}{c}\right)}{2} \approx -\frac{\Delta}{2} \tag{3.4}$$

where we assume small detunings from resonance, such that $v \ll c$. This condition can only hold if the particle has a finite velocity along the beam direction, contrary to the standard scheme where pump and probe beams have the same frequency and the particle interacts with both on resonance only if it is at rest along the beam direction.

Eq. (3.4) tells us that if the pump beam is offset by a frequency $+\Delta$ from the probe beam, then we encounter a Doppler-free signal if we detune the probe beam by $-\Delta/2$ from the lab-frame resonance. We can therefore eliminate the frequency difference between the iodine and lithium lines by choosing an appropriate frequency offset between the pump and probe beams.
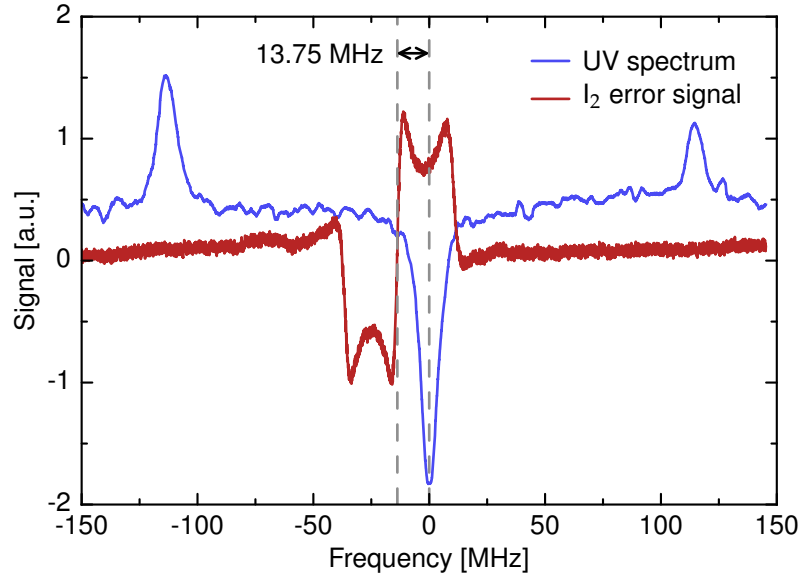
Figure 3.10: Calibration of the iodine transition frequency. Blue curve: Doppler-free fluorescence spectrum of ^{6}Li. The two peaks correspond to the $|2S_{1/2}, F = 3/2\rangle \rightarrow |3P_{3/2}\rangle$ and $|2S_{1/2}, F = 1/2\rangle \rightarrow |3P_{3/2}\rangle$ transitions, respectively. The central dip is the ground state crossover line. Red curve: error signal of closest iodine line. Both signals are obtained by lock-in detection. The frequency difference between the iodine and lithium lines is measured from the crossover minimum to the zero crossing of the error signal, whereas the frequency axis is calibrated by the ^{6}Li hyperfine splitting of 228.205 MHz.

We first measured the lithium UV transition frequencies using Doppler-free spectroscopy in a heat pipe. Instead of measuring the absorption of the probe beam, we used the fluorescence of the lithium vapour as a signal for higher sensitivity. The vapour was imaged onto a large area, high-gain photodetector (DET100A by Thorlabs). The pump beam was chopped at a few kHz using a chopper wheel and the photodetector signal was amplified by lock-in detection with 100 Hz bandwidth.

By slowly scanning the laser frequency we could observe the hyperfine structure of the ground state. At the same time, a part of the 646 nm light was sent through the iodine spectroscopy, where we measured the error signal of the iodine lines. This way, we could calibrate the frequency difference between the lithium crossover line and the closest iodine transition (Fig. 3.10). We found the iodine line at a frequency of $\delta = 13.75$ MHz below the lithium crossover line. Therefore, if we detuned the iodine spectroscopy pump beam by -27.5 MHz with respect to the probe, we would shift up the effective iodine resonance frequency and thus set it equal to the crossover line.

To bridge this gap, we now use two AOMs in series on the pump beam path. The first AOM shifts the frequency down by -100 MHz, and the next one shifts it back up by 72.5 MHz. We apply an additional full-amplitude modulation on the first AOM in this chain at 150 kHz. This gives a chopped pump beam, which we exploit for extracting the error signal by the extra lock-in detection described in Section 3.6.2.

3.7   Dipole traps

While laser cooling has been a workhorse of cold-gas experiments, the regime of quantum degeneracy with alkali atoms is not accessible with laser cooling alone. One requires forced evaporative cooling in optical or magnetic traps to reach high enough phase-space densities for creating Bose-Einstein condensates or degenerate Fermi gases. We use three different types of far-detuned optical traps that serve different purposes.

3.7.1   "Magic-wavelength" dipole trap

The UV transition in lithium has a useful feature that the polarisabilities of the $2S_{1/2}$ and $3P_{3/2}$ states are equal if the atoms are irradiated with light close to 1069 nm [222]. Therefore, there is no differential light shift of the two states and no effect on the laser cooling with UV light in the presence of an optical trap at this magic wavelength. This enables us to directly load a suitable optical trap from the UV MOT.

We use a broadband high-power ytterbium fibre laser (YLR-100-LP by IPG Photonics) with 100 W output power, a central wavelength of 1070 nm, and a FWHM spectral width of 3 nm. A sketch of the optical setup is shown in Fig. 3.11(a). The

beam is collimated to 5 mm diameter with a proprietary collimator. Using a PBS and a waveplate in a homemade, motorised rotation mount, we can send all the power into a water-cooled beam dump at the beginning of the setup and switch the power into the setup when it is needed. The beam is reduced to 1 mm diameter using a telescope and sent through a special shear-mode AOM (I-FS080-2S2G-3-LV1 by Gooch and Housego) which offers large diffraction angles due to a slow shear wave, and very high diffraction efficiencies of $\sim 93\%$ for low RF powers at the cost of speed.

After the AOM, we use the transmission through a mirror to monitor the diffracted power using a low-noise homemade photodetector. A PI controller is used to stabilise the power to a given setpoint via feedback to the AOM.

The beam is then expanded with a $1:6$ telescope and subsequently focused down with a 600 mm lens through the glass cell into the MOT chamber. The waist at focus was measured to be $w_0 = 100 \, \mu$m. For the final mirror, we use a piezo-actuated mirror mount (KC1-PZ by Thorlabs) for precise positioning.

3.7.2 Transport trap

For moving the atoms from the MOT chamber into the glass cell, we use a tightly focused optical dipole trap with a movable focus [224]. Optical transport of atoms is a common method for shifting atoms between vacuum chambers and a simple alternative to magnetic transport, which offers the possibility of transporting large samples but demands a complex design of magnetic coils. Furthermore, optical transport is less restrictive in the magnetic sublevels the atoms can populate during the transport process. The most common technique for optical transport is by mechanically moving optics using linear translation stages. Recent progress has been made in dynamic shifting of the trap focus position and size using focus-tunable lenses [225].

Our transport trap is derived from a high-power Nd:YAG laser at 1064 nm rated at 42 W output power. The setup is shown in Fig. 3.11**(b)**. Using a PBS and a waveplate in a homemade, motorised rotation mount, we can split up to 7 W of the power into a path where the intensity of the beam is switched and controlled by a high-power AOM (3080-1990 by Crystal Technology) and the diffracted order is coupled into a single-mode fibre for mode cleaning. The laser power that does not enter this optical path to the transport trap is sent to a fibre distribution breadboard for the optical physics lattice (see Section 3.8).

The fibre output is collimated to a waist of $w \approx 9.5$ mm and the beam is then focused down with a 750 mm lens, giving a measured focus size of $\sim 30 \, \mu$m. Three mirrors after the final lens steer the beam onto the atoms through the MOT chamber, such that the trap exits through the far end of the glass cell (Fig. 3.12). The first of the three mirrors is a motorised mirror mount (8818-6 by Newport) for fine posi-
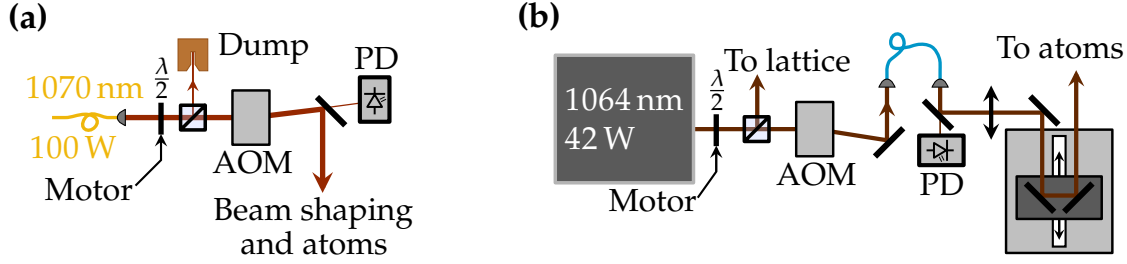
Figure 3.11: High-power infrared optical traps. Most optical elements (lenses, waveplates and mirrors) are omitted for simplicity. **(a) "Magic-wavelength" dipole trap setup.** A motorised waveplate controls the overall power in the setup. The photodiode (PD) is used to stabilise the power via the AOM. The final mirror has piezo actuators to fine-tune the beam position. **(b) Transport trap setup.** The laser power is split between a distribution setup for the physics lattice and the transport trap using a motorised waveplate and PBS. An AOM switches and controls the power coupled into a fibre, whose output is focused down using a lens. It is steered onto the atoms by mirrors on an air-bearing translation stage, which moves the focus back and forth.

tioning. The other two mirrors, placed in a cat-eye configuration, are mounted on an air-bearing linear translation stage (ABL1500 by Aerotech). The translation stage moves over 14.42 cm in 0.53 s, shifting the focus by twice this distance.

3.7.3   Crossed dipole trap

For further confinement of the atoms in the glass cell and for evaporative cooling, we use a further dipole trap at 1064 nm, derived from a high-power fibre amplifier (ALS-IR-50-SF by Azur Light). This "cross" trap has a waist of 130 μm and is used to provide a small confinement volume for the atoms. It is sent through the high-resolution objective with a displacement to the central axis and therefore focused onto the atoms under an angle of $\sim 20°$ to the z-direction. This is to avoid standing waves by back-reflections from the uncoated glass cell. The arrangement of the crossed dipole trap is shown in Fig. 3.12.

3.7.4   Dimple trap

To reach low temperatures and have good control over the total atom number in the system under study, it is useful to use small-volume optical "dimple" traps that are filled up from larger volume traps [226]. Furthermore, for quantum gas microscopy it is currently not possible to image three-dimensional systems due to the very small depth of focus. Therefore, one typically needs to restrict the atoms to a single two-dimensional plane.

We implemented a small-volume optical trap with a highly elliptical geometry to
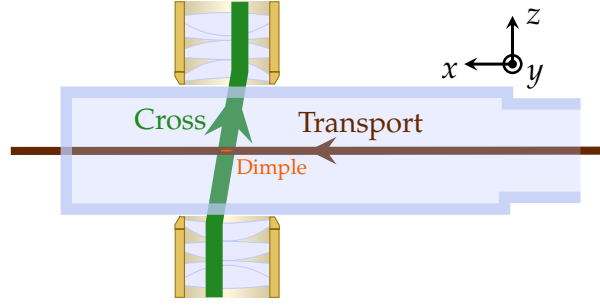
Figure 3.12: Crossed dipole trap and dimple. The 1064 nm transport and cross traps intersect above the objective to localise the atom cloud. The 780 nm dimple trap is perpendicular to the plane.

confine the atoms into a single plane before ramping up the optical lattice. The trap is derived from a distributed feedback (DFB) diode laser running at 780 nm. The power is switched and controlled using an AOM with a feedback loop. Its diffracted order is coupled into a fibre leading to the experimental table. After the outcoupler, the beam is shaped with a cylindrical telescope to an aspect ratio of approximately 1:6.

It is then focused down using a high-NA aspheric lens of 40 mm effective focal length. The resulting focus has waists of 1.7 μm along the z-direction and 10 μm in the x-direction. It intersects the crossed dipole trap beams as shown in Fig. 3.12.

3.8 Physics lattice

The optical lattice used in the experiment is slightly unconventional in its design, but provides a naturally flexible and tunable geometry. With our setup, we can realise non-trivial lattice geometries such as superlattices, with full control over relative barrier heights and relative phases of the different lattices. This will allow for studying many implementations of quantum many-body systems.

The principle of our lattice is not based on counterpropagating beams, but rather on interfering beam pairs under an angle. Generally, two beams of wavelength λ_{latt} interfering with a total opening angle φ between the two wave vectors produce an optical standing wave of a period:

$$a_{\text{latt}} = \frac{\lambda_{\text{latt}}}{2 \sin \frac{\varphi}{2}} \tag{3.5}$$

For the standard case of counterpropagating beams with $\varphi = 180°$, we reproduce the usual lattice constant of $\lambda_{\text{latt}}/2$.

Our method builds upon generating pairs of parallel and phase coherent beams

that are sent through a focusing lens or objective with a high NA. The beam pair is focused down under an angle, intersecting in the focal plane of the lens and generating a standing wave in the plane of the two beams. Due to the nature of optical images, one can think of this technique as a Fourier synthesis of a lattice potential, whereas the input beams to the focusing element play the role of the Fourier components [199] and their image is the corresponding Fourier pattern. As this technique has rotational symmetry around the optical axis, one can send in beam pairs running in orthogonal planes, to generate orthogonal standing waves.

One can extend this scheme by sending in a second pair with half the separation between the beams and a slightly different frequency to avoid cross-interference between both standing waves. The half distance leads to a standing wave of twice the spacing. Overall, this results in an optical superlattice potential.
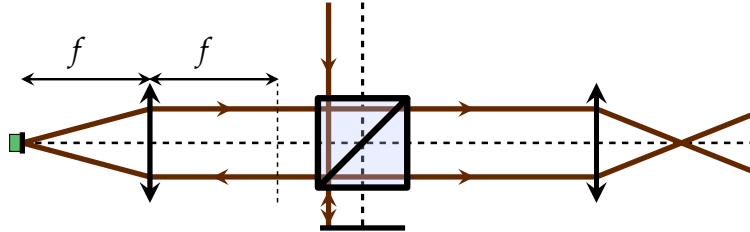
3.8.1   Lattice interferometers

We use a modified Michelson interferometer setup to generate pairs of parallel beams (Fig. 3.13**(a)** and [199, 227]). A large PBS splits incoming beams into two arms, a "short" one with retro-reflecting mirrors which recombine the beams at the same PBS, and a "long" one where the beam is focused by a lens onto a mirror and reflected back. The distances in the long arm are chosen such that the lens provides a $4f$ imaging system, which cancels a distance of $4f$ from the optical path of the Gaussian beam, such that the effective optical paths of the long and short arms are the same. The Gaussian beams therefore have the same sizes and divergences when they are recombined.

If we send in an input beam with some displacement to the optical axis, it gets focused by the lens in the long arm under an angle and gets reflected back onto the other side of the optical axis. This way, the output of the PBS after recombination consists of two parallel beams derived from one. The two beams are therefore phase coherent by definition.

In our setup, we send in beams with displacements of $d = 6.5\,\text{mm}$ and $2d = 13\,\text{mm}$ (Fig. 3.13**(b)**). By focusing the output beams with our high-resolution microscope objective (described in Section 3.3), this generates lattices of constants $a_{\text{latt}}^{xy} = 2.32\,\mu\text{m}$ and $a_{\text{latt}}^{xy} = 1.16\,\mu\text{m}$, respectively. The beams are delivered to the objective via a $1:1$ telescope with two $500\,\text{mm}$ lenses. To avoid having too small beams at the intersection point, they all need to have their focus at the principal plane of the objective. As the $1:1$ telescope must produce this focus on each beam, we require a focus within the interferometer setup. This places stringent demands on the distances between all the elements in the setup.

A second interferometer is used to generate a superlattice along the vertical z-direction. We create two pairs of beams within a vertical plane, which get focused

(a)

(b)
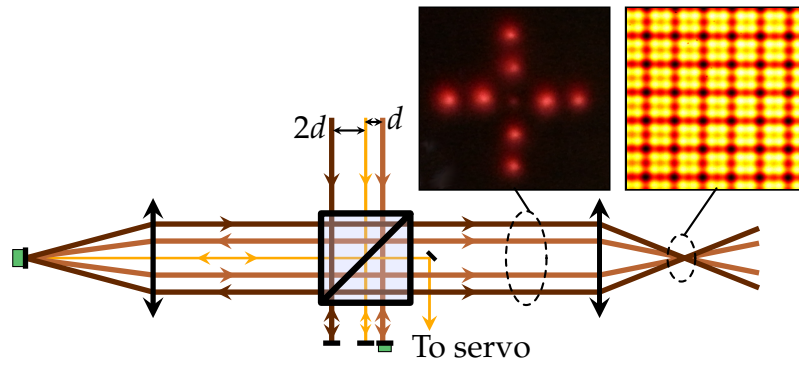
Figure 3.13: Physics lattice generation. (a) Principle of interferometric lattice generation. A displaced input beam of a Michelson interferometer gets split and recombined to a parallel beam pair, which is then focused down to produce a standing wave. A piezo can be used to shift the mirror of the long interferometer arm. **(b)** Concrete implementation for realising a superlattice. Two input beams at 1064 nm of displacements d and $2d$ produce two lattices of spatial periods $2a_{\text{latt}}$ and a_{latt}, respectively. A similar beam arrangement displaced out of the plane (not shown) produces a superlattice in the orthogonal direction. A weak alignment beam (yellow) travels along the optical axis and is picked out for interferometer stabilisation to an interference fringe. On the short arm, each beam has its own mirror. The large-scale lattice mirrors are mounted on piezos to shift the relative phase of both lattices. The inset figures show the 2D output pattern of the interferometer and the resulting interference after focusing. The interference pattern was measured by picking up the departing beams and imaging them onto a camera.

down using a 40 mm aspheric lens at the side of the glass cell – the same one used to focus the dimple trap. The z-lattice is positioned to overlap with the xy-lattice beams coming from below. We can produce vertical standing waves of lattice constants $a_{\text{latt}}^z = 3\,\mu\text{m}$ and $a_{\text{latt}}^z = 1.5\,\mu\text{m}$.

3.8.2 Phase stabilisation

The absolute phase of the lattice is stabilised via the interferometer arm lengths. A low-power "alignment" beam runs along the central axis of the interferometer. We pick out this beam from the centre after the interferometer, whereas it contains two orthogonal polarisations from both interferometer arms. By sending it through an EOM, we can modulate the phase of only one of the polarisations. We use a PBS to rectify the polarisations and send them onto a fast photodetector (KU LNA BB 0180A by Kuhne Electronic), where we measure the strength of the beating of the modulated and unmodulated part. We demodulate the beat signal and obtain a sinusoidal error signal, which we centre around 0 V and feed back to a piezo which shifts the mirror of the long interferometer arm. This method gives a more robust stabilisation than a direct side-of-fringe stabilisation to the DC signal.

To stabilise the relative phase between the short and long lattices, we can pick up the beams after traveling through the atoms with an identical objective on the other side of the glass cell and image the interference pattern on a camera (inset of Fig. 3.13(b)). By fitting or Fourier transforming the lattice image, we can detect phase deviations from the desired pattern. As each lattice beam has its own small mirror in the short arm of the interferometer, these deviations can be corrected by a phase shifter piezo (S-303.CD by PI) which displaces the mirror of one of the two axes.

3.9 Pinning lattice

Our large scale, tunable physics lattice is a powerful tool for studying fermionic quantum many-body systems. However, it is very limited in terms of potential depth for the purpose of fluorescence imaging. In quantum gas microscopy, one needs a lattice of typically several hundred to thousand E_{rec} depth, much more than what we can achieve with the physics lattice. Therefore, we rely on a further optical "pinning" lattice solely for the purpose of fluorescence imaging.

The pinning lattice consists of high-power retro-reflected lattice beams in 3D. Their wavelength is 1064 nm, therefore the pinning lattice constant is 532 nm, which oversamples the physics lattice by more than a factor of two in each direction. Every physics lattice site has access to at least 8 pinning lattice sites in its immediate vicinity. The pinning beam arrangement is shown in Fig. 3.14(b).
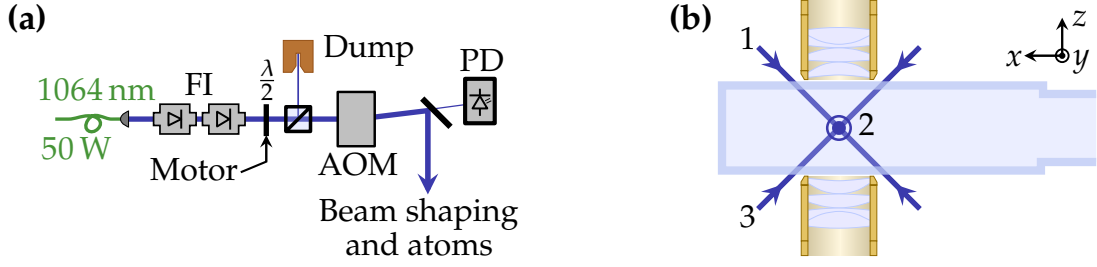
(a)

(b)

Figure 3.14: Pinning lattice. (a) Single pinning laser setup. A dual-stage Faraday isolator (FI) protects the fibre amplifier from the returning beam. A motorised waveplate controls the power in the setup. The photodiode (PD) is used to stabilise the power via the AOM. **(b)** Arrangement of the three pinning lattice axes. Axis 2 is actually tilted by $10°$ with respect to the y axis. The plane of axes 1 and 3 is orthogonal to 2.

This oversampling has two benefits: on the one hand, it allows us to work with any physics lattice geometry we want because the detection system is separate from the physical system under study. On the other hand, it provides a way to circumvent light-induced losses, a common limitation in all quantum gas microscopes [110, 111]. Pairs of atoms that populate the same lattice site during fluorescence imaging get rapidly lost due to light-assisted collisions. The oversampling of the physics lattice allows for separating pairs of atoms into different pinning lattice wells, where they can be detected without losses. By detecting higher fluorescence levels on a physics lattice site, one can directly measure these multiple occupancies. The prevention of pairwise losses with the pinning lattice is a unique feature of our experiment and is described in more detail in Section 5.3.

For each pinning lattice axis, we use a Yb-doped fibre amplifier with $50\,\text{W}$ of nominal output power (NUA-1064-PD-0050-D0 by Nufern). The three pinning lattice amplifiers are seeded with the same Nd:YAG seed laser source (Mephisto by Coherent) and have very similar setups: each amplifier is protected from the retro-reflected power by two Faraday isolator stages at the output. A waveplate in a motorised rotation mount allows for diverting all the power into a water-cooled beam dump via a PBS. Following the PBS, we use a shear-mode AOM to switch and control the power. A photodiode that measures the transmission through a mirror provides a signal we use for a feedback loop onto the AOM. A sketch of a pinning lattice setup is shown in Fig. 3.14(a).

After the AOM, we use a telescope to set the correct beam size before focusing the beam onto the atoms with a single lens. We typically produce a focus waist of $56\,\mu\text{m}$ on every axis. After the pinning beam passes through the cell, it is collimated with

a further lens before being retro-reflected. On each axis, we use a motorised mirror mount before the glass cell and for the retro-mirror for very precise beam positioning.

3.10 Raman laser
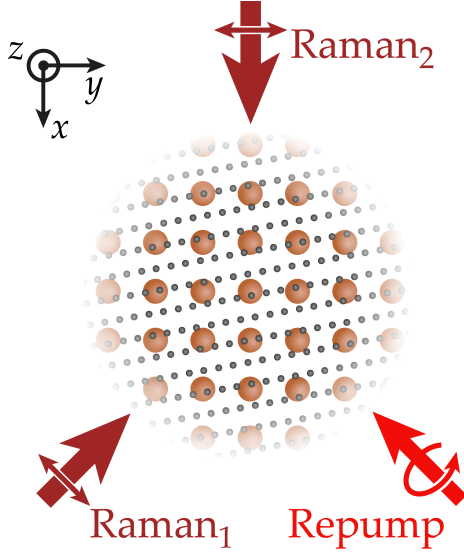
Figure 3.15: Raman beams and polarisation. Brown dots mark the physics lattice sites and grey dots show the pinning lattice sites in a vertical range of $\pm 250\,$nm from the lattice plane. The repump beam is used for Raman sideband cooling described in Section 5.2.2

To perform fluorescence imaging and simultaneous Raman sideband cooling in the pinning lattice, we use a pair of red-detuned beams for inducing Raman coupling between the two hyperfine levels of the ground state. This can also serve as a diagnostic tool for the pinning lattice (see Section 5.1). For this purpose, we use a dedicated tapered amplifier at 671 nm.

The Raman beam is sent through a double-pass AOM setup for switching the overall power. Afterwards, the beam is split into two paths: one is directly coupled into a single-mode optical fibre for the first beam ("Raman$_1$") delivered to the experiment. Using a further AOM double-pass setup, the second beam ("Raman$_2$") is shifted up in frequency by $\sim 228\,$MHz, then coupled into its own single-mode fibre leading to the experiment. Both AOMs are used for stabilising the powers of the two beams independently via feedback from photodetectors on the main experiment table.

Both Raman beams are sent into the glass cell under a mutual angle of $135°$ (Fig. 3.15). The difference momentum vector $\Delta \vec{k}$, which describes the net momentum transfer of the two Raman beams, is such that it has the same projection onto all three pinning lattice axes. This is necessary to achieve efficient Raman sideband cooling in three dimensions simultaneously.

Summary

This chapter described the hardware used for producing and imaging a Fermi gas of ^{6}Li in an optical lattice. A diode laser system at 671 nm provides light for laser cooling

and imaging. We produce cooling light on the narrow transition $2S \rightarrow 3P$ transition using a homebuilt UV laser system, where the sum of two infrared frequencies is produced in a PPLN crystal and then frequency doubled. A Doppler-free spectroscopy on iodine serves as a frequency reference for the UV laser.

Several optical traps have been described, which serve different purposes such as cooling, transport and/or confinement. Our physics lattice is generated by a modified Michelson interferometer that produces pairs of parallel beams that are focused down to interfere under an angle, providing flexibility in choosing the lattice geometry. A further high-power 3D pinning lattice is dedicated to the high-resolution imaging process, with a Raman laser used for sideband cooling.

Chapter 4

Preparation of ultracold 2D samples

With the hardware described in the previous chapter, we can produce ultracold Fermi gases of ^{6}Li confined to a 2D geometry, which is the starting point of all our experiments.

This chapter describes the experimental sequence, starting from two stages of laser cooling, optical trapping, evaporative cooling, transport, preparation of a single plane of atoms and a further step of magnetically driven evaporative cooling. The final step is the production of a spin-polarised gas using magnetic forces.

4.1 Laser cooling

Our laser-cooling scheme is standard and relies on the diode lasers described in Section 3.4. A special feature is the narrow-line cooling at 323 nm [182, 202] using the homebuilt laser system described in Section 3.5. With these two stages of laser cooling, we can directly load several millions of atoms into an optical trap with very short cycle times of a few seconds.

4.1.1 Zeeman slower and 671 nm MOT

First, the atoms are decelerated by a beam of 100 mW in the Zeeman slower. The beam is collimated to a diameter of 15 mm and 100 MHz red detuned to the cooling transition. The atoms are then captured in a standard MOT along the 671 nm D_2 line. We apply a quadrupole field of 36 G/cm along the vertical direction during the loading phase.

The three MOT fibres provide the light for each axis, whereas each fibre delivers an equal ratio of cooling and repumping light. Each beam is collimated at ~ 1.5 cm diameter. The three beams are sent through the chamber and then retro-reflected. The mirrors closest to the vacuum viewports on every side are dichroic mirrors that reflect 671 nm light and transmit light at 323 nm, in order to combine and separate the red MOT beams from the UV beams.

Both frequencies of the MOT beams are red-detuned by approximately $8\Gamma_{2P}$ with
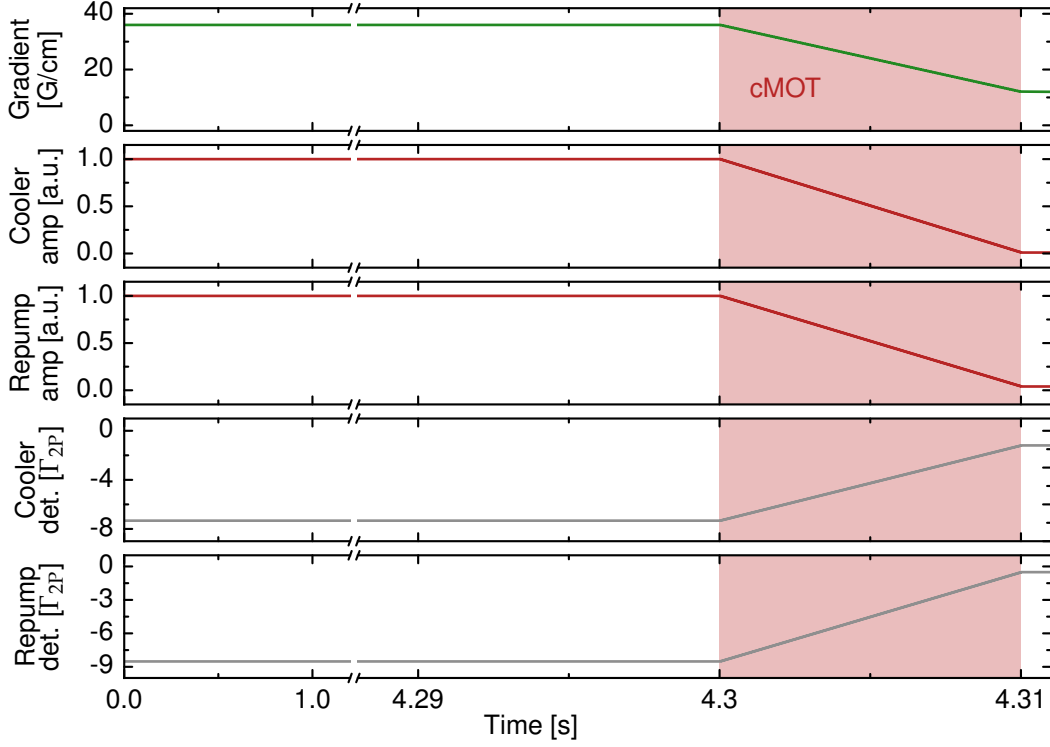
Figure 4.1: Timeline of the red MOT. The traces show the gradient field, amplitudes and detunings of the cooling and repumping light. The compressed MOT (cMOT) stage takes place in the last 10 ms.

respect to their transitions. The peak intensity is $\sim 8\,I_{\text{sat}}$, where $I_{\text{sat}} = 2.54\,\text{mW/cm}^2$ is the saturation intensity of the D_2 cooling transition [181, 196]. We capture around 10^8 atoms in 4 s, currently limited by the laser power in the MOT beams. The steady-state temperature of the atoms is roughly 1 mK, as measured by time-of-flight expansion.

After the regular MOT stage, we follow up with a compressed MOT. Within 10 ms, the gradient is reduced from 36 G/cm to 12 G/cm, the detuning to roughly Γ_{2P} and the MOT beam intensities to a few percent of their original value. This reduces the temperature to 300 µK and gives a phase-space density of $n_0 \lambda_T^3 \sim 2.1 \cdot 10^{-6}$, where n_0 is the peak density and $\lambda_T = h/\sqrt{2\pi m k_B T}$ is the thermal de Broglie wavelength. A timeline of the MOT parameters is shown in Fig. 4.1, and a detailed study of the MOT performance for different parameters is found in [196].

4.1.2 323 nm MOT

The standard red MOT is followed by narrow-line cooling along the UV transition $2S_{1/2} \rightarrow 3P_{3/2}$. As UV light causes colour-centre formation in silica optical fibres [228], which leads permanent transmission loss, we have to deliver the UV beams through free space. Furthermore, we cannot use a retro-reflected configuration as for the red MOT, since the vacuum viewports are anti-reflection coated only for 671 nm. Due to the unfavourable coating, the reflectivity for the UV light is up to 40% per surface, with a strong angle dependence to the level of 1°. Therefore, we send six separate beams into the chamber while maximising the throughput through each viewport via the beam angle.

We start with a detuning of a few linewidths on both frequencies and a gradient of 12 G/cm. After a few ms, we ramp down the power and tune both frequencies closer to resonance. In the meantime, the gradient is slightly increased to 17.5 G/cm. The process was optimised to maximise the density when loading the following optical trap (see Section 4.2.1). The UV cooling is very rapid, and the entire process takes only 13 ms. A time trace of the relevant parameters is shown

Figure 4.2: Absorption image of atoms released from the red cMOT (left) and UV MOT (right). Expansion time is 2ms.

in Fig. 4.3 and a comparison of cloud sizes between the red and UV MOTs is shown in Fig. 4.2.

We typically capture $3 \cdot 10^7$ atoms in the UV MOT, giving a capture efficiency of 30% from the red MOT. We found that there is a trade-off between minimum temperature after laser cooling and density of the cloud in the centre. It was more important for us to optimise the density and compensate small residual light shifts of the following dipole trap. For our current optimal parameters, we achieve a drop in temperature in the UV MOT to 60 μK. After the UV MOT, we found an increase in phase-space density to $3.2 \cdot 10^{-5}$, so over a factor of 10 higher than in the red cMOT. Temperatures as low as 33 μK and phase-space densities on the order of $3 \cdot 10^{-4}$ have been reported in UV MOTs of lithium [202].

We switch off the repump light 500 μs before the cooling light to optically pump the atoms from $|2S_{1/2}, F = 3/2\rangle$ to $|2S_{1/2}, F = 1/2\rangle$ (blue shaded area in Fig. 4.3). This directly yields a balanced, incoherent spin mixture of the $|F = 1/2, m_F = \pm 1/2\rangle$ (i.e. $|1\rangle$ and $|2\rangle$) states, which can be evaporatively cooled together in an optical trap.
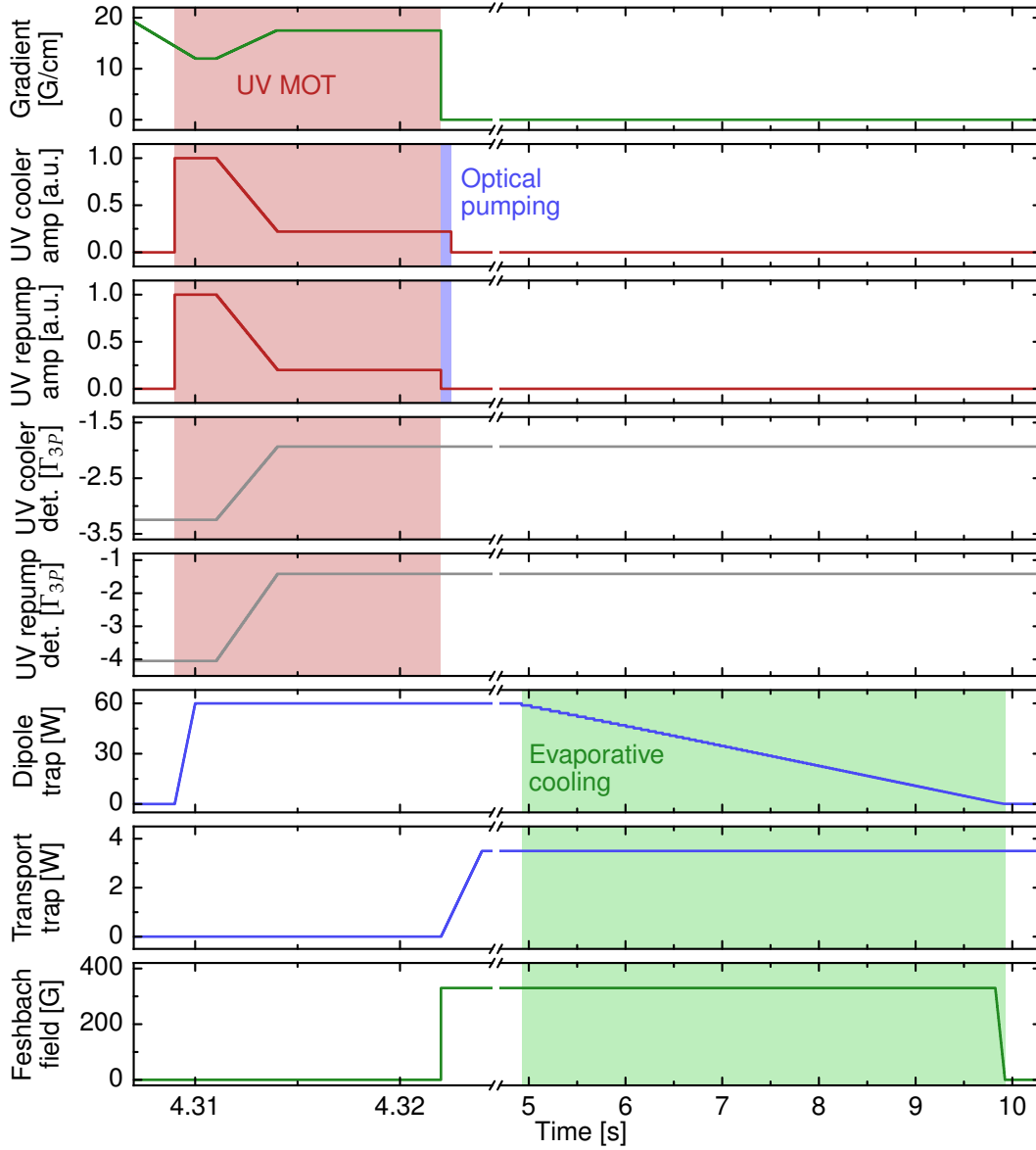
Figure 4.3: Timeline of UV MOT and dipole traps. The traces show magnetic fields, detunings and amplitudes of the UV light, as well as optical trap powers. In the optical pumping stage, the UV repump light is switched off before the cooling light to pump the atoms into a $|1\rangle$-$|2\rangle$ mixture. The atoms are transferred into the dipole trap and evaporatively cooled into the transport beam.

4.2   Dipole traps

4.2.1   Magic-wavelength trap

The dipole trap at 1070 nm, described in Section 3.7.1, is ramped on while the UV MOT is running (Fig. 4.3). The trap has a power of up to 65 W and a waist of 100 μm. If the UV MOT is performing optimally, we can capture up to $9 \cdot 10^6$ atoms in the dipole trap. Currently, the captured atom numbers are in the range of $5 \cdot 10^6$. Using a Feshbach coil pair at the MOT chamber, we apply a homogeneous magnetic field of 330 G to the dipole trap to set the scattering length to $-290a_B$. We then reduce the power in a linear ramp of 5 s to almost zero for evaporative cooling.

Due to the arrangement of the Feshbach coils, the field is not entirely homogeneous but has a saddle point: from the centre point of the coils, the field grows in the vertical direction along the coil axis, and becomes weaker along the horizontal plane. As both spin components are high-field seeking at the Feshbach field, they are confined in the horizontal plane and deconfined along the vertical direction. However, the radial confinement of the dipole trap is much stronger than the magnetic deconfinement. Nevertheless, it is important to align the beam exactly to the centre point in between the coils such that the deconfining potential has a quadratic maximum, otherwise the magnitude of the forces becomes much stronger and leads to rapid losses from the trap when the intensity is reduced.

4.2.2   Optical transport

During the evaporative cooling in the dipole trap, we ramp on the tightly focused transport beam at 1064 nm and 3.5 W to capture the atoms. Afterwards, the air-bearing translation stage is triggered to shift the focus from the MOT chamber to the glass cell over a distance of 28.84 cm. The stage undergoes a constant acceleration over 0.7 cm to a velocity of 30 cm/s, then keeps this velocity until decelerating to zero over the last 0.7 cm. We optimised the transport trap power and stage velocity to get the highest efficiency in transported atom numbers. We could achieve over 80% efficiency with very little heating and found no measurable dependence on the shape of the acceleration profile.

4.2.3   Crossed dipole trap

After the atoms arrive in the glass cell, the cross trap from below is turned on. We ramp on a Feshbach field at 300 G, and within a few seconds reduce the power of the transport beam in a sequence of linear ramps, roughly optimised to keep the highest number of atoms in the crossing region of both optical traps (Fig. 4.4). In the end of
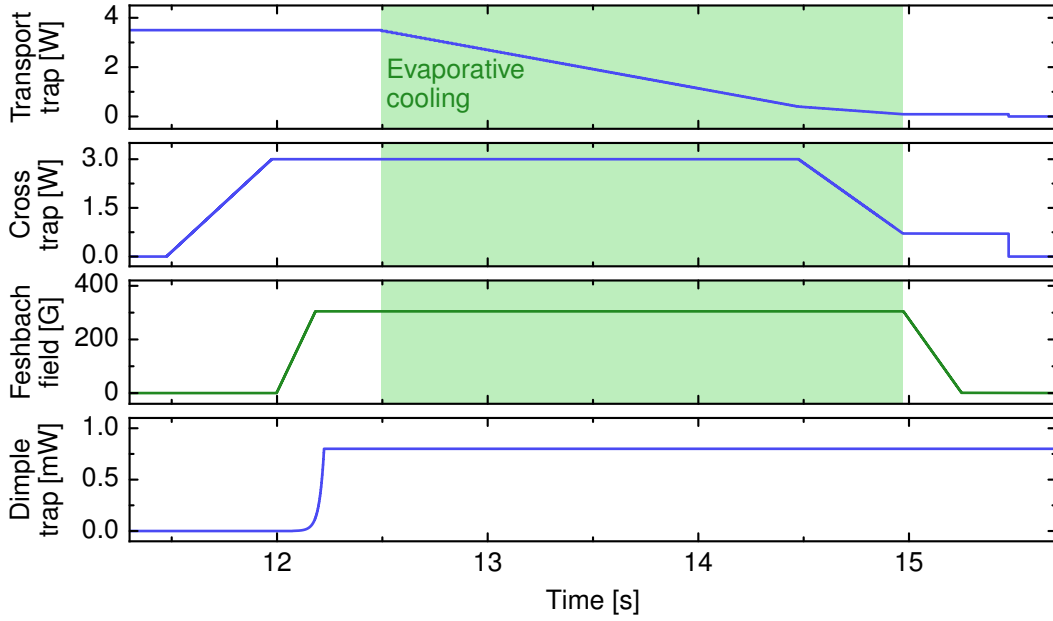
Figure 4.4: Optical evaporation in the glass cell. The atoms are transported to the glass cell, confined by the crossed dipole trap and evaporatively cooled in a Feshbach field of $300\,\text{G}$

the trapping stage, we have atom numbers of typically $1.5 \cdot 10^5$ at a temperature of $0.2\,T_\text{F}$, measured by fitting the expanding cloud with a polylogarithm [229].

4.2.4 Dimple trap

The $780\,\text{nm}$ dimple trap is ramped on during the crossed dipole trap stage and kept on for the entire duration of evaporative cooling in the crossed trap. After the crossed trap is turned off, the atoms are trapped in the dimple on its own. We find that density-dependent losses limit the atom number for too large dimple intensities. Therefore, the dimple power is optimised for maximum density. The highest atom numbers we trap are typically 10^4.

4.3 Preparation of a degenerate 2D gas

4.3.1 Vertical lattice

After filling the dimple trap, we load the atoms into the vertical z-lattice, which is produced interferometrically (see Section 3.8). We use the inner pair of beams to ob-

tain a long-scaled z-lattice of $3\,\mu$m spacing (Fig. 4.5(a)). The z-lattice is ramped on exponentially in order to be as adiabatic as possible.

The dimple trap is of such small volume that we can load a single plane of the z-lattice. It is important to have the dimple aligned to the centre of the plane, which places a strict demand on the lattice phase stability.

Initially, we got up to 50% of the atoms in neighbouring planes, which we would clean out using RF. We would apply a vertical gradient field and selectively transfer the atoms in all the wrong planes from $|1\rangle$ and $|2\rangle$ to the states $|F = 3/2, m_F = \pm1/2\rangle$, which undergo spin-changing collisions [230] and get rapidly lost from the trap. By carefully optimising the dimple shape and avoiding any clipping of the beam that led to a larger dimple trap volume after focusing, we could greatly improve the single-plane loading and abandon the RF cleaning altogether.

4.3.2 Magnetic evaporation

The transfer of atoms from a 3D harmonic trap into a standing wave can lead to heating. To counter this heating and dispose of atoms excited to a higher band in the vertical lattice, we need to apply evaporative cooling. At the same time, the standard technique of reducing the trap depth via the intensity is not a valid option because the lower intensity would lead to tunneling of the atoms to other planes. The only viable alternative is to change the effective trap depth by tilting the potential with a magnetic gradient field to spill out the most energetic atoms.
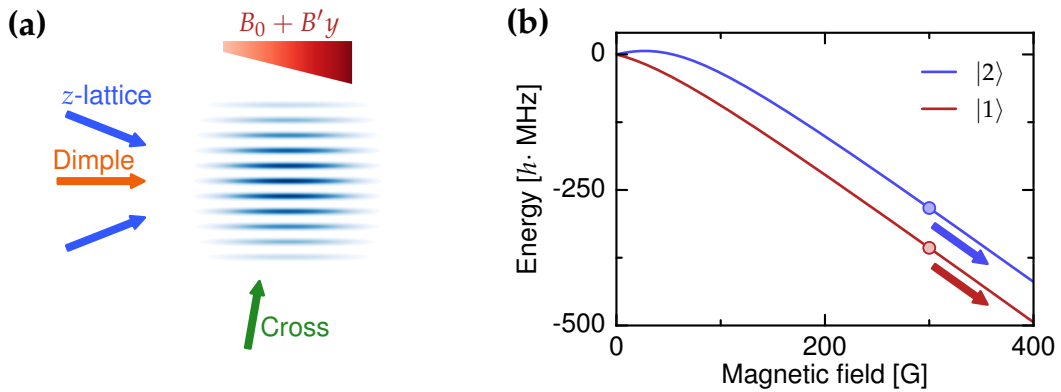
Figure 4.5: *z*-**lattice loading and magnetic evaporation.** **(a)** Arrangement of z-lattice and optical traps. A strong magnetic bias field B_0 and gradient B' are applied for evaporative cooling. **(b)** Energy level vs. magnetic field of the two spin components. At the bias field of $300\,$G, the magnetic gradient force on both spin components is the same.
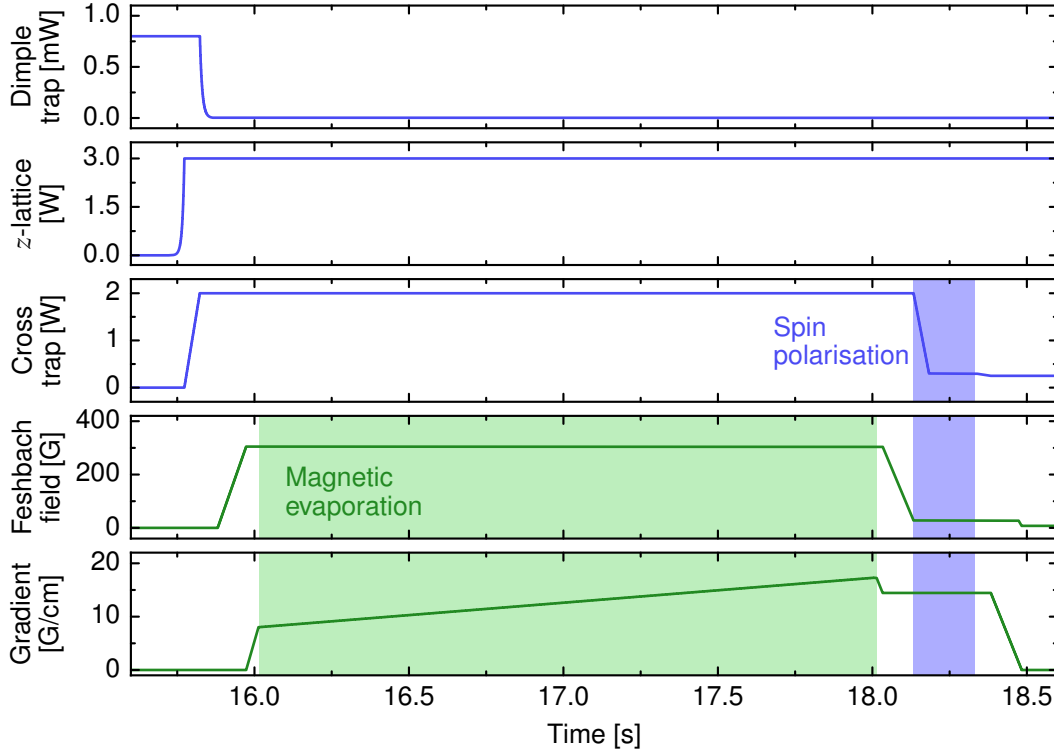
Figure 4.6: Timeline of the sequence in the vertical lattice. The atoms are loaded into a single plane from the dimple trap, evaporatively cooled with a magnetic gradient and then spin polarised.

We ramp on the Feshbach field, which is oriented along in the lattice plane, and superimpose a horizontal gradient field created by the extra coil pair embedded in the Feshbach-coil mount (Fig. 3.3 and Section 3.2.3). This gradient leads to an approximately constant force on the atoms, which in turn leads to a linear tilt of the potential. As the atoms are already in the Paschen-Back regime, the potential tilt for both spin components $|1\rangle$ and $|2\rangle$ is practically equal (Fig. 4.5(b)).

We keep the cross trap on to provide sufficiently stiff radial confinement to the atoms. The gradient is quickly ramped on in 40 ms to 8 G/cm, up to which we observe no losses from the trap. It is then slowly increased in a linear ramp over 2 s to a final value between 16 G/cm and 20 G/cm. This value is chosen to set the final density in the trap. A timeline of this process is shown in Fig. 4.6.

4.3.3   Spin polarisation

It is necessary to maintain a spin mixture of fermions for all steps of evaporative cooling. However, all experiments in the lattice that will be described later are conducted

with only a single spin component. To prepare a single-component Fermi gas, the gradient is slightly reduced to 15 G/cm to decrease the potential tilt, and the Feshbach field is ramped down to 27 G, where the magnetic moment of the $|2\rangle$ spin component vanishes (Fig. 4.7(a)). We maintain the magnetic gradient while reducing the confining potential given by the cross trap from below. The force on atoms in state $|1\rangle$ remains finite and pulls them out of the trap, while it should vanish for atoms in state $|2\rangle$ to first order. After spilling out the atoms, a Feshbach field of 8 G is kept on until the end to maintain a fixed polarisation of the atoms. The blue shaded area in Fig. 4.6 shows this protocol.

To verify that this process works efficiently, we spill out one component and measure the population of both components $|1\rangle$ and $|2\rangle$ via Stern-Gerlach separation. Be-
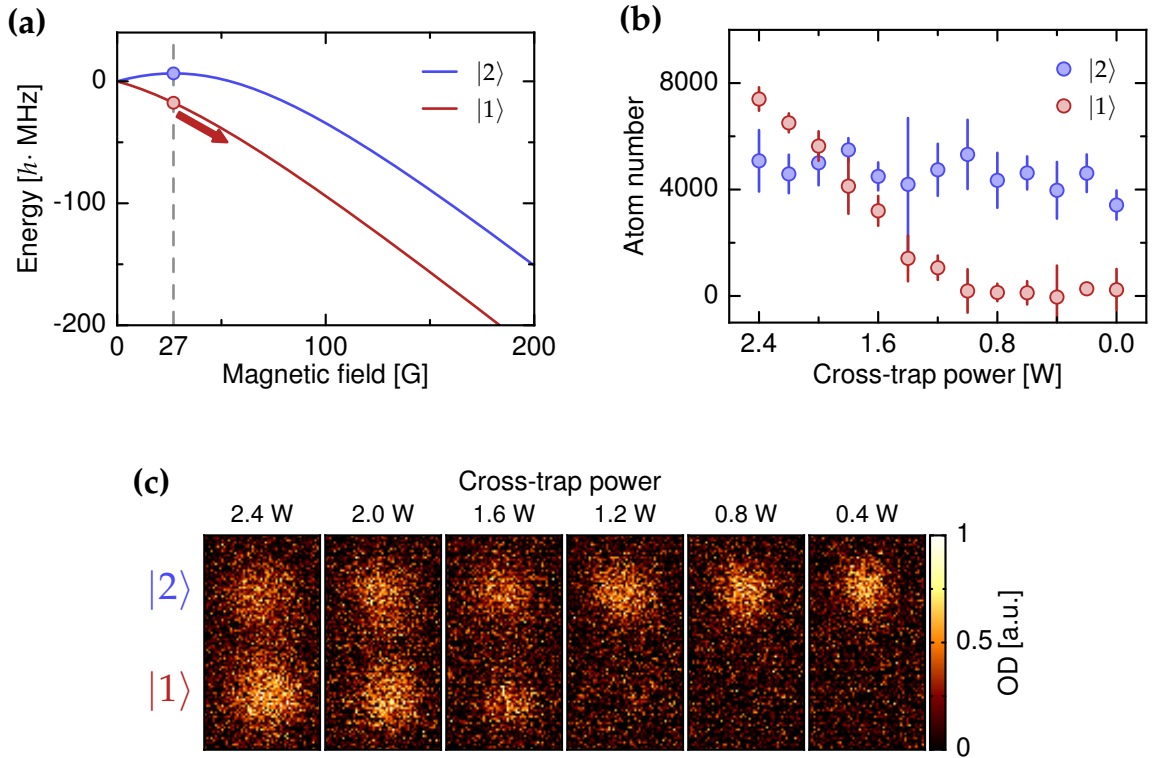
Figure 4.7: Creating a spin-polarised sample in the plane. (a) Energy diagram for spill-out process. At 27 G, the magnetic moment of $|2\rangle$ vanishes, while $|1\rangle$ remains high-field seeking. **(b)** Atom numbers of both spin components measured for different confinement strengths. Error bars denote one standard deviation. **(c)** Absorption images of clouds after spin polarisation and Stern-Gerlach separation.

fore switching off the trap for absorption imaging after time-of-flight, a transverse magnetic gradient field of 38 G/cm is turned on 1 ms before the trap is extinguished. It stays on during the expansion period of the cloud of 700 μs , after which we see clear separation of the two components (Fig. 4.7(c)).

We fix the spill-out gradient to 15 G/cm and vary the confinement via the cross-trap power from below. Then, we compare the number of atoms of both spin components and find that for increasingly weak confinement, there are no measurable losses for atoms in state $|2\rangle$, while the atoms in state $|1\rangle$ are entirely lost (Fig. 4.7(b)). We settle for 0.3 W of cross-trap power as a good compromise between guaranteeing losses of $|1\rangle$ while maintaining stiff enough confinement for $|2\rangle$.

In Fig. 4.7(b), there appears to be a population imbalance at stronger confinements, which may be an artifact from the gradient field that is still on during absorption imaging and the imaging frequency is better matched to the lower cloud than for the upper. There are otherwise no processes throughout the experimental cycle that would give rise to a spin imbalance.

Summary

Using two stages of laser cooling and efficient evaporative cooling in optical traps, we can produce ultracold Fermi gases with a short cycle time ($<$ 20 s). The atoms are loaded into a single plane of the vertical lattice using an appropriately shaped dimple trap. We perform evaporative cooling in the plane and can remove one spin component using magnetic gradient fields. The single-component sample in a 2D plane is the starting point of experiments on an ideal Fermi gas. The next step is to ramp on the physics lattice in the xy-directions and perform fluorescence imaging to image single atoms.

Chapter 5

Single-atom imaging of fermions

In this chapter, the methods to obtain fluorescence images with single-site resolution are presented. Using the techniques described in Chapter 4, we prepare a 2D gas of spin-polarised fermions in a single plane of a vertical optical lattice. After ramping up the physics lattice in the plane to enter the Hubbard regime, the atoms are transferred into a dedicated pinning lattice for imaging. We apply Raman sideband cooling for scattering photons while keeping the atoms near the vibrational ground state of the pinning lattice. This technique has already proven successful for fluorescence imaging of large clouds in optical lattices [231], single atoms in tight optical tweezers [232], and single fermionic atoms in optical lattices [128, 129]. Our method of freezing the atomic distribution using a short-scaled pinning lattice offers a new possibility of avoiding pairwise losses of atoms, currently present in all quantum gas microscopes. Analysis of the fluorescence images shows that we are able to detect more than one atom per physics lattice site.

This chapter contains an overview of the pinning lattice and Raman processes. The imaging results with sideband cooling are presented along with an analysis of the fluorescence signals. A simple model for the absence of pairwise losses is presented, as well as an experiment demonstrating this point in systems with many double occupancies.

5.1   Raman processes in the pinning lattice

Our main tool in single-atom imaging is the pinning lattice dedicated for the imaging process. With waists of 56 μm and powers of typically 20 W, we achieve trap depths of 800 μK per axis. This corresponds to on-site trap frequencies of $\omega_{tr} = 2\pi \cdot 1.4$ MHz. These large trap depths are necessary to sufficiently suppress tunneling of the light lithium atoms. We probe the characteristics of the pinning lattice using the Raman laser described in Section 3.10. For the following, it is operated with a one-photon red detuning of $\Delta = 7.3$ GHz with respect to the D_1 line.

5.1.1   Resolved sideband spectrum

We measure the on-site trap frequencies in the pinning lattice using sideband spec-
troscopy. The trap frequencies are large enough to easily resolve the vibrational level
structure on every site. First, the atoms are transferred to the pinning lattice from the
dimple trap in the $F = 1/2$ hyperfine level. The Raman beams are switched on and
the Raman detuning is swept over a range of $20\,\mathrm{kHz}$ in $150\,\mu\mathrm{s}$ to transfer the atoms
from $F = 1/2$ to $F = 3/2$. The population in $F = 3/2$ is measured by absorption
imaging without a repumping beam to keep the atoms in $F = 1/2$ invisible.

   We repeat this measurement for different relative detunings of the two Raman
beams and register a transfer if the frequency corresponds to the carrier transition
$|F = 1/2, \nu\rangle \rightarrow |F = 3/2, \nu\rangle$ or to a sideband $|F = 1/2, \nu\rangle \rightarrow |F = 3/2, \nu \pm 1\rangle$. A
sideband spectrum is shown in Fig. 5.1(a). The blue sideband transitions $\nu \rightarrow \nu + 1$
are clearly visible for the three different axes, whereas the red sidebands $\nu \rightarrow \nu - 1$
are barely distinguishable from the noise. This means that most of the atoms start out
in the lowest vibrational state, but we cannot quantify the fraction reliably. For the
spectrum shown here, the three pinning axes are set to powers of $[15.5\,\mathrm{W}, 21\,\mathrm{W}, 12\,\mathrm{W}]$.
The on-site trap frequencies are expected to be $2\pi \cdot [1.23\,\mathrm{MHz}, 1.43\,\mathrm{MHz}, 1.08\,\mathrm{MHz}]$,
which matches well to the measured sidebands.

   The shapes of the lines differ between the axes: pinning axis 2 has a narrower and
more sharply peaked sideband. This is due to the shape of the cloud loaded from
the dimple into the pinning lattice. The cloud is elongated along pinning axis 2 and
perpendicular to the other two axes. The entire cloud sits therefore in the largest
depths of pinning axis 2 and therefore gets transferred at the same time. For the
other two axes, the centre of the cloud lies at the maximum depth, but the tips lie in
regions where the intensity is reduced due to the strong inhomogeneity of the traps.
Therefore, we probe locally different trap frequencies on the other two axes with the
Raman transfer, leading to a broadening of the sidebands towards lower frequencies.
This explains the asymmetric shape of the lines.

5.1.2   Raman coupling strengths

Using the bias coils around the glass cell, we set the background magnetic field to
values smaller than $10\,\mathrm{mG}$, so we neglect the sublevel structure. We determine the
residual field with high precision by measuring RF transitions between the sublevels
of $F = 1/2$ and $F = 3/2$.

   The two Raman beams are linearly polarised, so we can also ignore vector light
shifts that would lift the sublevel degeneracy, and thus treat the hyperfine levels as
an effective two-level system. We measure the Raman coupling strength Ω_R by mea-
suring Rabi oscillations between the two hyperfine levels. The atoms are loaded from
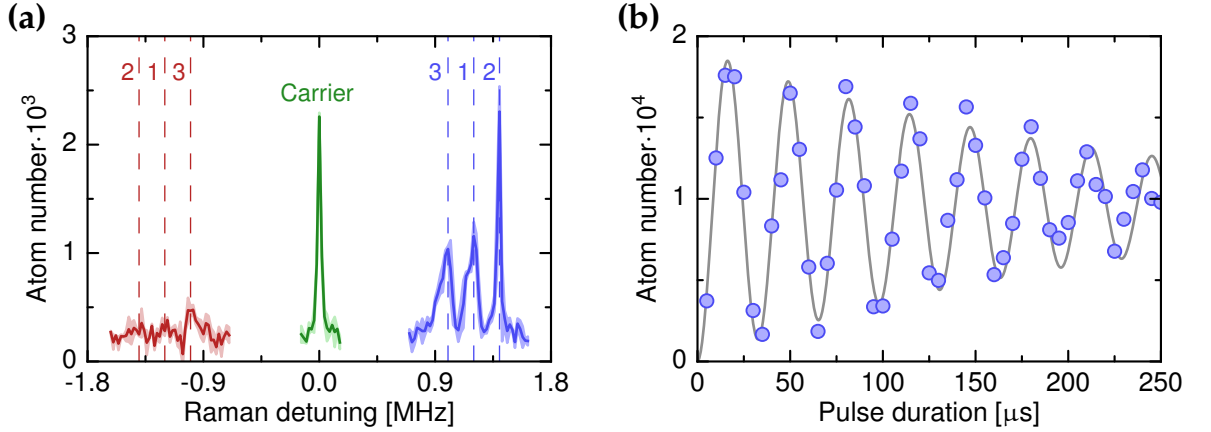
Figure 5.1: Raman processes in the pinning lattice. (a) Raman sideband spectrum, showing resolved sidebands for the three pinning lattice axes (numbers marked on plot). The red sidebands are barely visible. Shaded regions mark the standard deviations. **(b)** Coherent oscillations on the Raman carrier transition. The blue circles are measured data, the grey line is a fit with an exponentially decaying cosine.

the crossed dipole trap into the pinning lattice to be isolated from each other. We then drive the oscillations with square-shaped Raman pulses of variable length. The two-photon detuning is set to zero to address all the atoms equally on the carrier transition. One of the beams has a peak intensity of $325\,\mathrm{mW/cm^2}$ and the other one has 10 times more intensity. The resulting oscillations are shown in Fig. 5.1(b), where we measure a Rabi frequency of $\Omega_R = 2\pi \cdot 30.6\,\mathrm{kHz}$ and a damping rate of $\gamma \approx 4.7\,\mathrm{ms^{-1}}$. Using this, we can infer the coupling rates for any power combination, as Ω_R scales as $\sqrt{I_1 I_2}$, where $I_{1/2}$ are the intensities of the two beams [233].

A more interesting case is the Raman coupling of hyperfine levels with a transfer of vibrational energy in the lattice. In the regime where the motional sidebands are well resolved, the electronic and vibrational degrees of freedom are separable. The atoms can be in different product states $|F = 1/2, \nu\rangle$ and $|F = 3/2, \nu'\rangle$, where the $|\nu\rangle$ are vibrational states that we can approximate with harmonic oscillator levels. The transition strength between two such states is obtained from the dipole matrix element. The electronic part factors out to give the Raman Rabi frequency Ω_R, while the vibrational degree of freedom gives an extra factor that takes the momentum transfer $\Delta\vec{k}$ of the light onto the atoms into account. The total coupling is given by [234]:

$$\Omega_R^{\nu\nu'} = \Omega_R \langle\nu'| e^{i\Delta\vec{k}\cdot\vec{r}} |\nu\rangle = \Omega_R \langle\nu'| \exp\left[i\eta_R(\hat{a} + \hat{a}^\dagger)\right] |\nu\rangle \tag{5.1}$$

where $\hat{a}^\dagger$ and $\hat{a}$ are the raising and lowering operators for the vibrational energy levels,

respectively. We introduce the Lamb-Dicke parameter:

$$\eta_R = \sqrt{\frac{E_{\text{rec}}(\Delta\vec{k})}{\hbar\omega_{\text{tr}}}} = \sqrt{\frac{\hbar\Delta\vec{k}^2}{2m\omega_{\text{tr}}}} \tag{5.2}$$

where $E_{\text{rec}}(\Delta\vec{k})$ is the recoil energy associated with a momentum transfer $\Delta\vec{k}$. One must distinguish between two cases:

On the one hand, there is the Lamb-Dicke parameter which is commonly used to parametrise the confinement strength in harmonic traps. This parameter is based on the recoil momentum of a single-photon $k = 2\pi/\lambda$, and is a measure for the suppression of change in vibrational state during photon absorption. For our typical pinning-lattice trap frequencies of $2\pi \cdot 1.4\,\text{MHz}$, the single photon Lamb-Dicke parameter is:

$$\eta_1 = \sqrt{\frac{\hbar k^2}{2m\omega_{\text{tr}}}} \approx 0.23 \tag{5.3}$$

On the other hand, there is the Lamb-Dicke parameter which characterises the two-photon transition strength between $|\nu\rangle$ to $|\nu'\rangle$, from which we obtain the Raman coupling (5.1). Based on the 135° angle between the two beams (Fig. 3.15), the total momentum kick is larger than the single-photon momentum k by a factor of $\sqrt{2+\sqrt{2}} \approx 1.85$. At the same time, the vector $\Delta\vec{k}$ is not parallel to any of the motional axes of the pinning lattice, but has an equal angle of approximately $\vartheta = 55°$ with respect to every axis to ensure equal coupling to all sidebands. The exponent in the expression (5.1) therefore gets an extra projection factor of $\cos(\vartheta) \approx 0.57$. Consequently, the Lamb-Dicke factor for the two-photon transfer is given by:

$$\eta_R = \sqrt{\frac{\hbar k^2(2+\sqrt{2})}{2m\omega_{\text{tr}}}}\cos(\vartheta) \approx 1.06\eta_1 \tag{5.4}$$

The exponential in (5.1) can be expanded in powers of η_R. In the limit where $\eta_R \ll 1$, the matrix elements for transitions $|\nu\rangle \rightarrow |\nu \pm 1\rangle$ are dominant, and all others can be neglected. In this case, the coupling scales as $\eta_R\sqrt{\nu+1}$ for $|\nu\rangle \rightarrow |\nu+1\rangle$ and $\eta_R\sqrt{\nu}$ for $|\nu\rangle \rightarrow |\nu-1\rangle$ [234].

5.2 Single-atom resolved fluorescence imaging

5.2.1 Lattice parameters

After preparing the spin-polarised gas of fermions in a 2D plane, the physics lattice in the xy-plane is ramped up slowly within 100 ms to a depth of 2.4 µK per axis in
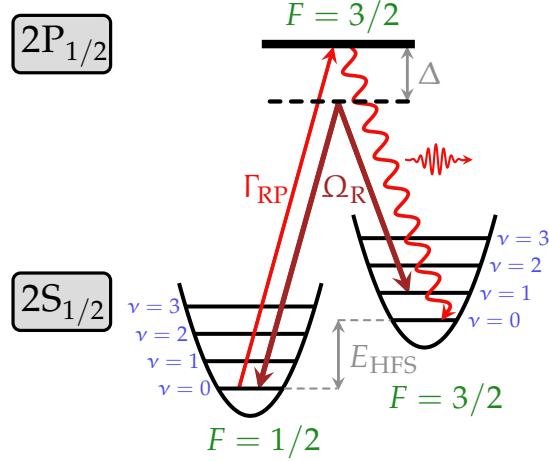
Figure 5.2: Raman sideband cooling scheme. Both Raman beams, detuned by $\Delta = 7.3\,\text{GHz}$, couple the ground state hyperfine levels, separated by $E_{\text{HFS}} = h \cdot 228.2\,\text{MHz}$, and transfer the atoms between neighbouring vibrational levels. The repumper brings the atoms back to $F = 3/2$, while the spontaneous emission provides a fluorescence signal.

order to be as adiabatic as possible. At this depth, the tunneling matrix element is given by $t_{xy} \approx 200\,\text{Hz}$. Along the vertical direction, the tunneling t_z is a few mHz due to the large spacing. We then ramp up the physics lattice depth to $6\,\mu\text{K}$ per axis in 1 ms to suppress the tunneling of the atoms by an order of magnitude. The pinning lattice is ramped up in 20 ms to adiabatically transfer the atoms to the pinning lattice sites. The "freezing" step in the physics lattice is necessary to prevent simultaneous density redistribution in the lattice during this ramp. The atoms feel a force towards the centre of the pinning lattice while it is being ramped up, due to its strong harmonic confinement. If the physics lattice is too shallow, the atoms get attracted towards the centre of the pinning lattice before it is deep enough to suppress tunneling on its own.

5.2.2   Raman cooling and imaging

For sideband cooling, we tune the Raman beams to couple the levels $|F = 3/2, \nu\rangle$ and $|F = 1/2, \nu - 1\rangle$. The atoms are then optically pumped into the level $|F = 3/2, \nu - 1\rangle$ using the repump beam running on the $|2S_{1/2}, F = 1/2\rangle \rightarrow |2P_{1/2}, F = 3/2\rangle$ transition (Fig. 5.2). The beam arrangement is shown in Fig. 3.15. We apply intensities of $2\,\text{W/cm}^2$ on Raman$_1$ and $22.7\,\text{W/cm}^2$ on Raman$_2$, which is chosen to be asymmetric because Raman$_1$ causes much more stray light on the camera. Based on Eqs. (5.1) and (5.4), we expect a coupling rate of $\Omega_R^{01} \approx 2\pi \cdot 48\,\text{kHz}$ between the lowest two states on each site.

The repumper has an intensity of $1.6\,\text{mW/cm}^2$ and is slightly blue-detuned to ac-
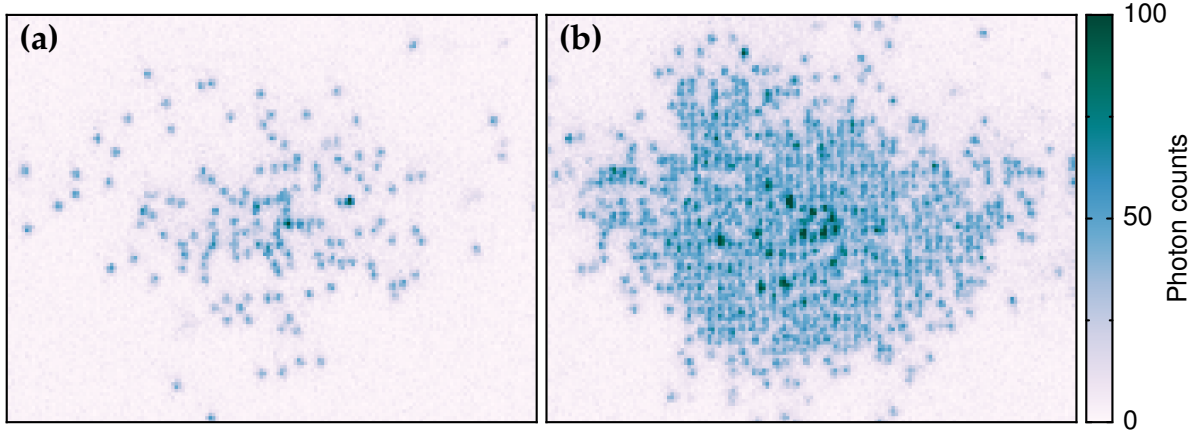
Figure 5.3: Single atom resolved fluorescence images. (a) Sparse cloud of single, spin-polarised ^{6}Li atoms. **(b)** A high density cloud of spin-polarised atoms, where we observe regions of almost unity filling, indicating a band-insulating behaviour.

count for the differential light shift on the D_1 line due to the pinning lattices. After enough cooling cycles, the atoms should accumulate in the state $|F = 3/2, v = 0\rangle$, which ideally should not couple to the Raman light or repumper any more. On the other hand, there is still off-resonant scattering from the repumper, which is only 228 MHz detuned, as well as from the intense Raman light. The off-resonant scattering rate is on the order of 3 kHz for the Raman light and 170 Hz for the repumper when the atoms are in the "dark" state. Both this scattering and the fluorescence from the spontaneous emission contribute to our signal.

The local energy gaps in the pinning lattice are not homogeneous, primarily due to the small waists of the pinning lattice, but also due to the anharmonicity of each site. For example, the energy difference between the lowest and first excited band is 30 kHz larger than the difference between the first and second excited bands. To address as many bands as possible and to enlarge our spatial cooling region, we periodically modulate the Raman detuning between 1 MHz and 1.4 MHz with a 20 kHz triangular wave.

Simultaneous exposure on the EMCCD camera for 1 s during Raman cooling leads to images like in Fig. 5.3 with very good signal-to-noise. We estimate a fraction of captured photons of 5% based on the NA of the objective and losses from the glass cell and other optics. The quantum efficiency of the camera is close to 95% at the imaging wavelength. Based on the number of counts we get per single atom, the total photon scattering rate per atom is in the range of 6–7 kHz.

The density of the system is set by the end point of the magnetic evaporation described in Section 4.3.2. For increasing density, we find that the atom distribution

tends to a dense core with one atom per site on average. This is what one expects for a single-component band insulator, where all available states are populated and all transport is suppressed by Pauli blocking. The properties of these band-insulating systems are investigated further in Chapter 6.

5.2.3   Imaging fidelity

To characterise the performance of our imaging system, we measure the point-spread-function (PSF) of the single atoms by taking many images of sparse samples, where individual atoms are separated by large distances. Isolated atoms are registered with a blob detection algorithm [235] and its signal is fitted by a Gaussian along the x- and y-directions. For the fit routines, the image is upsampled by a factor of 15 to have better precision in finding the peak centre. Afterwards, all Gaussians are centred onto each other and averaged, giving the PSF shown in Fig. 5.4**(a)** with Gaussian widths of $\sigma^x_{\mathrm{PSF}} = 403\,\mathrm{nm}$ and $\sigma^y_{\mathrm{PSF}} = 390\,\mathrm{nm}$. This is significantly larger than the theoretical value of $\sigma_{\mathrm{PSF}} = 290\,\mathrm{nm}$, which we also verified using an independent target. After all data for this thesis was taken, several successful steps were taken to improve the PSF size, including an increase in magnification, more careful alignment of the objective, and several improvements on the imaging setup. Currently, the PSF has $\sigma_{\mathrm{PSF}} = 320\,\mathrm{nm}$ on average.

To quantify the imaging fidelity further, we can take several successive images of $1\,\mathrm{s}$ exposure of the same sparse cloud and compare the images to detect hopping events and losses in a large region of $50\,\mu\mathrm{m} \times 50\,\mu\mathrm{m}$. The cooling parameters are optimised to minimise the tunneling and losses. For the best parameters, we find that after $1\,\mathrm{s}$, a fraction of $5(1)\%$ of the atoms tunnel, and $2.5(5)\%$ of the atoms get lost. However, these events occur mostly around the edge of the cloud, where the trap depths are not as large as in the centre.

5.2.4   Lattice reconstruction

For our analysis, it is essential to determine the spatial distribution of atoms in the lattice. To this end, we use a numerical reconstruction algorithm, developed by Timon Hilker, to find the lattice populations by analysing the fluorescence levels on each site.

First, the phase of the physics lattice is determined by taking an image with a clear lattice structure such as Fig. 5.3**(b)**. The image is then Fourier transformed in real space, giving Fourier peaks corresponding to the lattice wave vectors $\vec{k}_i$. The lattice phases in each direction are equivalent to the complex phases associated with the respective wave vectors. From the wave vectors we can extract not only the lattice constants but also any skew between the two lattices: the two axes have an $89°$ angle between them.
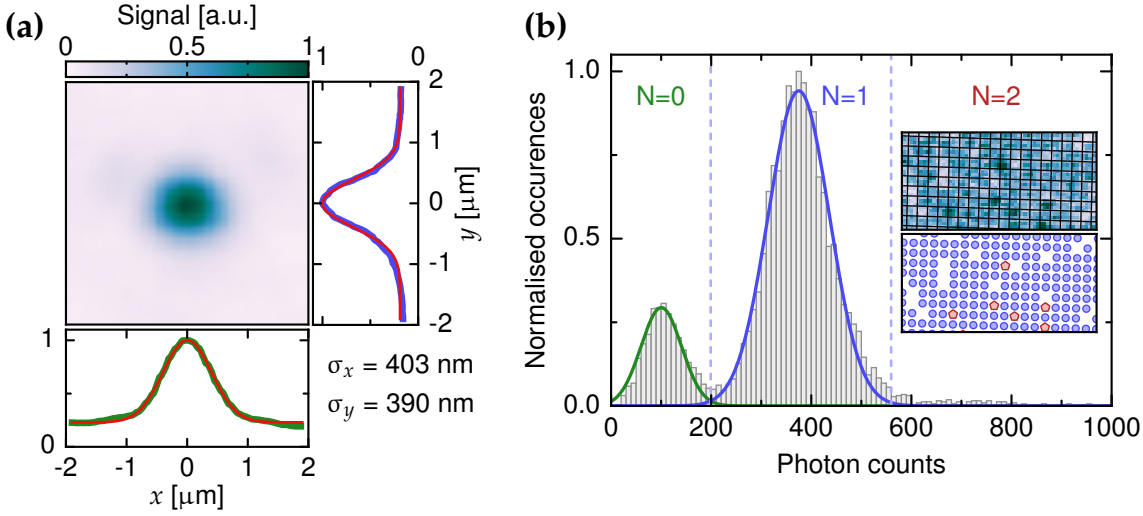
Figure 5.4: Reconstructing the lattice population. (a) Average PSF of 115 atoms with Gaussian fits to the integrated horizontal and vertical profiles. **(b)** Histogram of fluorescence counts for a central region of the lattice. The inset shows the region which has been analysed and the reconstruction. Blue circles denote single atoms, red pentagons mark doubly occupied sites.

Taking this phase information, we obtain a lattice grid that is overlaid onto the image, like in the inset of Fig. 5.4(b). The background offset around the edge of the cloud is globally subtracted from the image. A Gaussian with the size of the average PSF is then used as a fit function on every lattice site and the resulting amplitude of the Gaussian fit is taken as a measure for the fluorescence level. If this level exceeds a certain threshold, the site is marked as occupied. The statistics of the fluorescence levels are expressed as histograms of the Gaussian fit amplitudes (Fig. 5.4(b)). One sees a very clean separation between signals corresponding to populated sites and those corresponding to empty ones. The threshold for declaring a site to be occupied is set in between the two peaks. Based on the overlap between the two Gaussians, we estimate that less than 1% of the singly occupied sites are falsely identified as holes and vice versa.

The $N = 1$ peak in Fig. 5.4(b) has a width of $\sigma_{N=1} \approx 60$, which is three times larger than what one would expect from the photon shot noise $\sigma_n = \sqrt{n} \approx 19$, where $n \approx 375$ is the mean number of photons detected per atom. This discrepancy has a few possible causes:

- Tunneling and losses lead to variations in the registered photon counts per atom.

- The pinning lattice usually displaces the single atom peaks from the centre of the

physics lattice sites, so occasionally an atom signal will intrude into the neighbouring site, which disturbs the fit to the PSF. This can lead to slight mistakes in the fit amplitudes.

- The fluorescence level has slight variations over the width of the cloud (see Section 5.2.6) which can broadens the peak further.

- The tilted angles of the pinning lattice axes (Fig. 3.14(b)) lead to small random displacements of the atoms along the line of sight. This can give a slight variation in the size of the PSF of up to 10%. As the fit routine uses a fixed width for the fitted Gaussian PSF, the variation in widths of the atom signals can translate to a variation in fit amplitudes.

5.2.5 Doubly occupied sites

On most single images and on the histogram in Fig. 5.4(b), we see several sites with fluorescence levels that are clearly higher than the rest. These signals are well localised to one lattice site, so we conclude that these come from two atoms that populate the same physics lattice site. While a majority of these double occupancy occurences are visible by eye, it turns out to be very challenging to distinguish them numerically. The threshold for discerning $N = 1$ and $N = 2$ on a site is not as easily determined as for distinguishing $N = 0$ from $N = 1$, as we do not observe a clear peak separation between $N = 1$ and $N = 2$ signals on the histograms. The threshold for $N = 2$ is therefore set such that the $N = 1$ peak is centred between the two thresholds in the histogram. Possible systematic errors in determining the atom numbers are discussed in Section 5.2.6.

As all quantum gas microscopes suffer from immediate loss of double occupancies, their occurrence in our experiment may seem surprising. However, there is a subtle but straightforward explanation for this, which will be elucidated in Section 5.3.

5.2.6 Error estimates

The biggest cause of reconstruction uncertainty is the PSF being larger than expected. Many atom signals intrude onto neighbouring lattice sites due to the random pinning lattice site positions, which poses a challenge for the Gauss fitting and can be partially prevented by a smaller PSF. The most visible reconstruction errors arise from identifying double occupancies. For data analysis, it is important to know the impact of these errors on the number statistics.

First, we use several hundred images like in Fig. 5.3(b) and take statistics on how often a number of photon counts was encountered on each lattice site. We then evaluate the fluorescence statistics for a central region in the cloud and around the edges

(a)

(b)

(c)
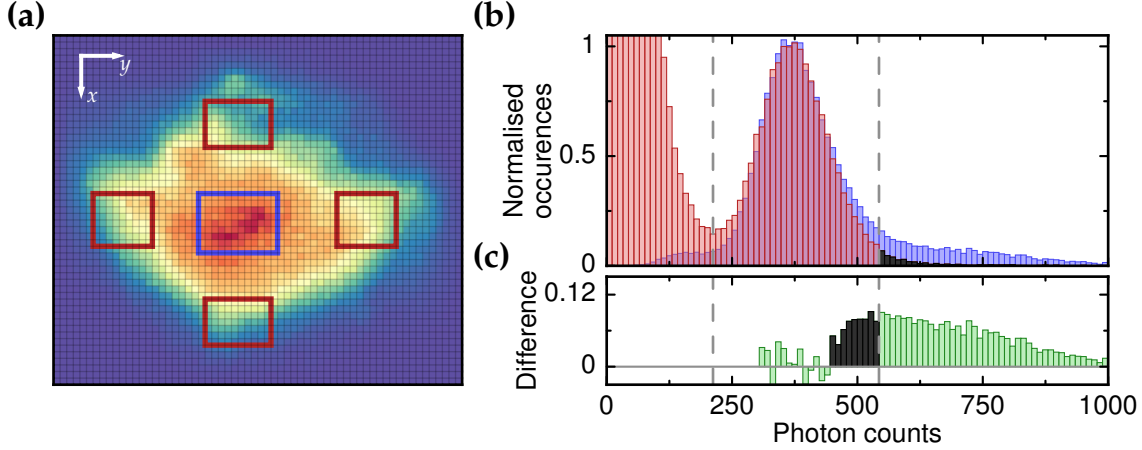
Figure 5.5: Estimate of the errors in assigning on-site atom numbers. (a) Fluorescence statistics in the lattice for a few hundred images. Each pixel corresponds to a single lattice site. The rectangles mark different regions where the fluorescence statistics are analysed. **(b)** Fluorescence statistics at the centre of the cloud (blue histogram and box in (a)) and at the edges (red histogram and boxes in (a)). The two histograms are compared and subtracted, giving the green histogram in **(c)**. The black regions left and right of the threshold are identified as wrongly assigned populations (see Text).

(Fig. 5.5**(a)**), and compare the histograms. Around the edges, where there are practically only single atoms and holes, we expect the histograms to reflect the pure signal of single atoms, and any excess signal in the centre must arise from double occupancies. Atoms in neighbouring planes can also contribute to added fluorescence, however we see that these strong fluorescence peaks are well localised to a single lattice site (inset of Fig. 5.4**(b)**), meaning that these atoms must be in the plane of focus.

One problem is that the peak fluorescence levels do not seem to match on different sides of the cloud. The peak photon count can vary by up to 10% going from one edge of the cloud to the other. This can be explained by a gradient in light intensity of the Raman beams. With a cloud radius of $\sim 24\,\mu$m and Raman beam waists of $140\,\mu$m, the intensity drops by up to 6% at the cloud edge compared to the centre. Any slight misalignment of the Raman beams can lead to larger intensity variations. To circumvent this issue, the histograms from different regions are normalised to each other and rescaled such that the peaks all coincide, in order to get an average histogram shape. This average is also scaled to fit the peak fluorescence counts in the centre.

In the low-density regions, we find only few incidents of counts that exceed the threshold for $N = 2$. In the central region, on the other hand, there is an extended tail of high fluorescence counts, with no clear separation between $N = 1$ and $N = 2$.

Subtracting the two histograms from each other gives a residual, which we assign as an excess signal from double occupancies (Fig. 5.5(c)). The part of this signal which lies above the threshold is assumed to be correctly assigned to $N = 2$, however the part underneath the threshold (shaded in black) is defined as double-occupancy signals that are wrongly counted as single occupancies. This part has an area which is 28% of the total area above the threshold, so we underestimate the number of double occupancies by this percentage. At the same time, the absolute number of assignment errors has to be added onto the single occupancies, because we count too many $N = 1$ events.

The histograms of the cloud edges with low densities also have some signals that exceed the threshold (shaded in black in Fig. 5.5(b)). These are considered single occupancies that are falsely assigned to $N = 2$ and are therefore missing from the $N = 1$ statistics. The fraction of this area is compared to the area under the $N = 1$ within its threshold boundaries. We find that we underestimate the number of single occupancies with a probability of up to 2.5%.

5.3 Avoiding light-induced losses

Currently, all quantum gas microscopes suffer from the loss of atom pairs that populate the same site during fluorescence imaging [110, 111]. The near-resonant light leads to light-assisted collisions with very high two-body loss rates [236, 237], such that no measurable signal from the atom pairs can be detected before they are lost. This restricts the detection to the parity of the atom number on each site. There have been different approaches to avoiding this parity projection, such as the spin-dependent splitting along one lattice axis using field gradients [123] or splitting of double occupancies into neighbouring layers of the lattice [238]. We find that in our experiment, the short-scaled pinning lattice offers a natural way to directly circumvent this issue.

5.3.1 Energy level evolution

Consider the 1D physics lattice shown in Fig. 5.6(a) with two energy levels on each site, corresponding to a ground and excited band. If two atoms of the same spin component populate the same lattice site, they necessarily start from the different bands (shown in Fig. 5.6(a) in blue and turquoise). When the pinning lattice is ramped up, a pinning site is to appear exactly at the centre of the physics site. During the ramp, the energy levels evolve into the new band structure of the pinning lattice. By diagonalising the Hamiltonian of the potential landscape for different pinning-lattice depths, we can follow this evolution carefully.

(a)

(b)
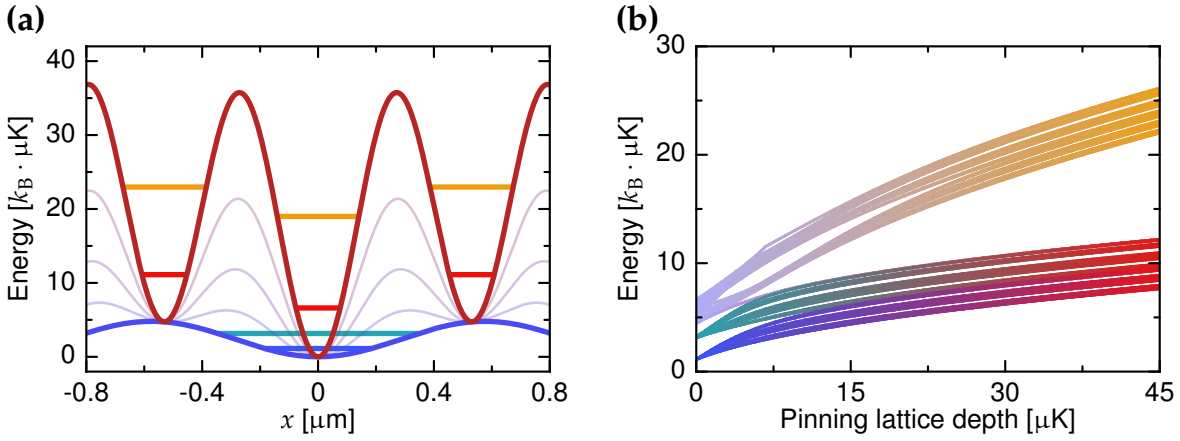
Figure 5.6: Deterministic separation of double occupancies into different pinning wells. (a) Evolution of physics-lattice potential landscape while the pinning lattice (red) is ramped on. For each lattice, the energy levels corresponding to two bands are shown. **(b)** The physics lattice ground band (blue) and excited band (turquoise) both merge into the ground band of the pinning lattice (red). The unoccupied continuum levels (pale blue) merge into the second pinning-lattice band (orange).

The band structure evolution is shown in Fig. 5.6**(b)**. The blue bundle of levels starting on the lower left corner corresponds to all ground-state energies of 20 physics lattice sites. These evolve into ground-state energy levels on pinning lattice sites. At the same time, the turquoise levels, corresponding to the upper physics lattice band, also all merge into the ground band of the pinning lattice. This means that two atoms originating from the same physics site must split into different wells to obey the Pauli exclusion principle. The only levels that evolve into the upper pinning-lattice band are continuum levels that are originally unpopulated.

A close look at Fig. 5.6**(b)** shows that the uppermost bound levels of the physics lattice have a slope pointing towards the excited band of the pinning lattice, but level off between 5-8 μK like in an avoided crossing. In fact, it is the tunnel coupling to neighbouring pinning sites in this region which prevents these levels from going into the upper pinning band. An atom in the upper physics-lattice band in Fig. 5.6**(a)** would, in principle, end up in the central pinning site on the excited level, as one might intuitively expect, but along the way its energy level comes in resonance with the ground state of the neighbouring site, causing the atom to tunnel to the next site and minimise its energy.

The tunnel coupling $\tilde{t}$ between the excited level on one site and the ground level on its neighbour when they are in resonance induces a gap in the energy level spectrum.

The width of the minimal gap is $0.82\,\mu\text{K}$, corresponding to $17\,\text{kHz}$, which is twice the value of $\tilde{t}$, and this sets an adiabaticity criterion: as long as the pinning-lattice ramp is slow enough, all the atoms will adiabatically follow the lower energy curves and end up in the ground band of the pinning lattice.

To estimate an upper bound for the probability to end up in the higher pinning-lattice band, we take the energy curves that approach each other the most and treat them as a two-level system with the gap $2\tilde{t}$. An atom starting on the lower branch and ramped across the gap can end up on the upper branch with probability given by the Landau-Zener formula [239, 240]:

$$P = \exp\left(-\frac{2\pi\tilde{t}^2}{\hbar\left|\mathrm{d}(\varepsilon_2 - \varepsilon_1)/\mathrm{d}t\right|}\right) \tag{5.5}$$

In the region close to the gap, where the energy curves are approximately linear, the energy difference $\varepsilon_2 - \varepsilon_1$ varies by $k_\text{B} \cdot 1\,\mu\text{K}$ per $4\,\mu\text{K}$ of pinning-lattice depth. As we ramp up the full pinning lattice of $800\,\mu\text{K}$ depth in $20\,\text{ms}$, the $1\,\mu\text{K}$ shift is covered in $100\,\mu\text{s}$, giving a "ramp velocity" of $\mathrm{d}(\varepsilon_2 - \varepsilon_1)/\mathrm{d}t = k_\text{B} \cdot 10\,\mu\text{K}/\text{ms}$. Inserting this value into Eq. (5.5) gives a probability of the atoms getting transferred to the upper pinning-lattice band of $P \sim 10^{-6}$. This means that in our experiment, we should expect practically all double occupancies of identical fermions to get split into neighbouring pinning wells.

Note, that this is the extreme case of a 1D lattice. As each physics lattice site is surrounded by pinning sites in 3D, the situation is even more relaxed. With many more pinning sites per physics site, there is a much better probability of finding a suitable pinning site to tunnel to during the ramp-up period.

5.3.2 Experimental probe of parity projection

To verify that this mechanism works as expected, we start out with a 2D gas in the z-lattice plane confined by the cross trap. Before ramping on the physics lattice, the cross-trap confinement is increased to different levels to squeeze the atoms within the plane. After ramping up the physics lattice, the atoms are directly transferred to the pinning lattice and imaged.

We find that for stronger confinement, the cloud radius shrinks and the amount of double occupancies in the centre of the lattice goes up considerably (Fig. 5.7(a)). At the same time, the integrated fluorescence counts of the whole system remain fairly constant for all compression strengths (Fig. 5.7(b)), which already implies undetectable losses during the process. A reconstruction of the lattice population shows that while the double occupancy fraction goes up, there is no increase in the number of holes in the system (Fig. 5.7(c)). In fact, the number of decreases slightly for increasing compression.
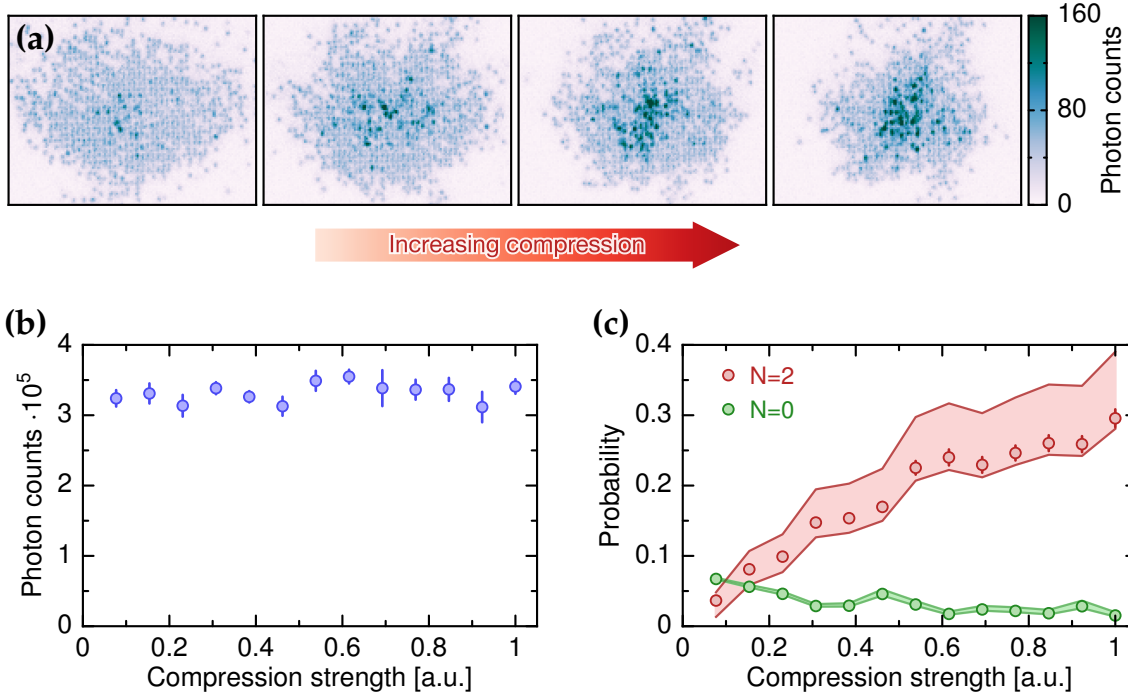
Figure 5.7: Experimental test of absence of parity projection. (a) Fluorescence images for clouds prepared with different levels of compression using the cross trap. A core of multiple occupancies builds up in the centre. **(b)** Integrated fluorescence levels over entire images for different compression strengths. Error bars mark the standard deviation of the mean. The constant level of fluorescence indicates and absence of losses. **(c)** Probability for double occupancies and holes, evaluated for 15×15 sites in the centre. Error bars denote the statistical uncertainty. The shaded regions mark the systematic uncertainty due to reconstruction errors.

Based on the systematic errors in reconstruction, we can set a conservative upper bound for the probability of atoms getting lost. For the strongest compression, we find a probability of detecting holes of $P_h = 2.0(5)\%$. For the double occupancies, the probability is $P_d = 30^{+10}_{-2}\%$. In the worst case, where we assume that we underestimate the holes and overestimate the double occupancies, the ratio between holes to double occupancies is $\kappa = P_h/P_d = 0.09$. If we assume that all holes originated from double occupancies, which is not generally true, then κ gives the probability for parity losses. As the holes primarily arise from the nonzero initial temperature of the system, the true probability for parity losses is presumably much lower.

5.3.3 Comment on parity-free detection of spin mixtures

The analysis of Section 5.3.1 and the experimental verification in 5.3.2 relies on the two atoms starting from different bands with a large enough energy gap. As we have only worked with spin-polarised Fermi gases so far, the double occupancy of a lattice site necessarily places both atoms in different bands. For a spin mixture, this is generally not the case, and they are expected to populate the lowest band. We find that preparing the same band-insulating system without spilling out one spin component leads to images with very strong density fluctuations between zero and two. The splitting becomes only probabilistic.

Several strategies are possible to extend the deterministic detection of atom pairs to spin mixtures:

- A magnetic gradient field along the vertical direction, together with the vertical superlattice can be used to separate the two atoms into neighbouring planes, where they would still be within our depth of focus.

- If the experiments start out in the large-scale physics lattice with $2.3\,\mu$m spacing, the double occupancies can be split into double wells along a horizontal direction together with a gradient field. This also offers a quick spin-dependent imaging scheme.

- By applying strong repulsive interactions between the two spin states, we can transfer the component $|2\rangle$ to $|3\rangle$ using RF while simultaneously transferring the same atoms into the upper band. The orthogonality of the wave functions of both bands is lifted by the interaction with the other spin component before the transfer.

- The repulsive interactions can be used to induce an interaction gap, which increases rapidly during the ramp-up of the pinning lattice. One of the atoms would tunnel to a neighbouring empty pinning site as soon as this interaction energy is equal to the energy offset of the next site. However, as the interaction gaps are typically much smaller than the band gaps of the lattice, this resonance condition occurs for deeper pinning lattices. This makes the tunnel couplings smaller and timescales for adiabaticity much longer, requiring slower ramps. During the time of writing, this scheme has already produced promising first results.

Summary

Basic measurements with the Raman beams in the pinning lattice were presented. We employ Raman sideband cooling in the pinning lattice to image the individual atoms in our system with high fidelity. Systems with band-insulating character could be

observed for high densities of a single spin component.

Our use of a pinning lattice provides a way to avoid parity projection of the lattice population. This can be understood in terms of tunnel coupling during the ramp-up process, which prevents double occupancies in different bands of the physics lattice from ending up on the same pinning lattice site. The reconstruction of the true atom numbers on each site still contains some systematic uncertainties, which were discussed in detail.

Chapter 6

Statistical study of a fermionic band insulator

The ability to image single fermions in an optical lattice and the possibility of avoiding parity-induced losses with the pinning lattice gives us, in principle, full access to the on-site number statistics, from which we can gain better insight about microscopic properties of the many-body system.

In this chapter, the statistics of a simple system – a single-component fermionic band insulator – is presented. For this study, 425 images very similar to the band insulator in Fig. 5.3(b) were taken. For each individual lattice site, we tracked how often the site was empty, singly occupied, or doubly occupied by two fermions of the same spin in different bands. These experimentally measured probabilities for a "hole" P_h, single atom P_s or double occupancy P_d give us access to site-resolved statistical observables, in particular the density, atom number fluctuations and entropy of the system. We also investigate density-density correlations in the band-insulating region as a probe for compressibility.

6.1 Density

The most basic observable is the average density of every site. We simply average the number of atoms detected for each individual lattice site and plot the 2D density distribution in Fig. 6.1(a). Due to the confining lattice potential, we expect the average density to roughly reflect its shape.

On the other hand, we find that there is a plateau of almost unity density near the centre of the trap, seen in the averaged cut in Fig. 6.1(b). This is a manifestation of Fermi statistics, as double occupancy of a single site with identical fermions in a single band is forbidden. Therefore, if all atoms populated the lowest band, we would expect ideally a flat-top density at the trap centre despite the curved confinement, as discussed in Section 2.2.1. However, we also observe double occupancies coming from atoms in a higher lattice band. These double occupancies pile up in the centre, leading to a slight increase in density above unity.
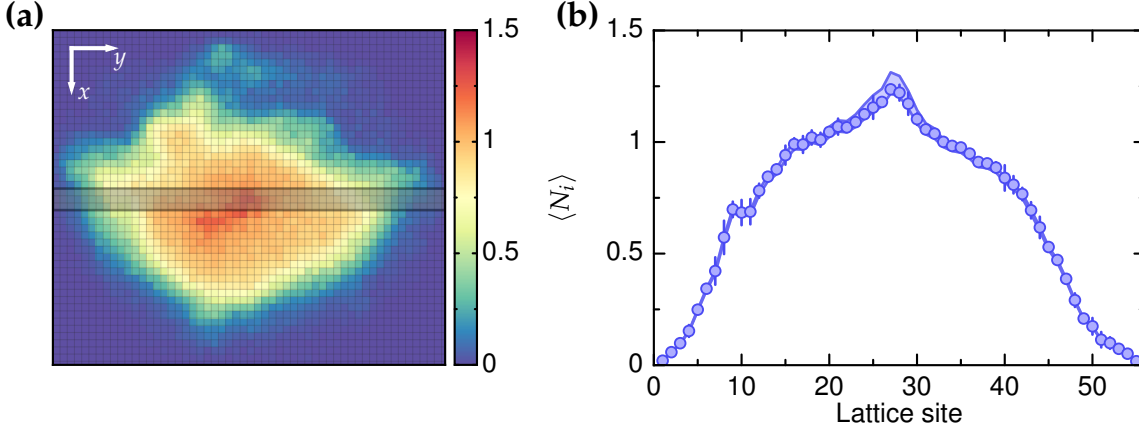
Figure 6.1: Density profile in the band-insulating regime with visible flattening.
(a) 2D distribution of average density for a band insulator. Each square pixel corresponds to a single lattice site. **(b)** Horizontal cut through the 2D plot with an average over three neighbouring lattice sites (grey area of Fig. (a)). The error bars show one standard deviation of the three averaged sites. The shaded areas display the systematic error due to reconstruction uncertainties.

We observe large-scale, static imperfections that possibly originate from slight clipping of the beams. These are not important for this study, as we observe no change in time of these features and we restrict ourselves to on-site properties only. The information about the exact external potential shape is not even necessary.

The uncertainties in the reconstruction algorithm, described in Section 5.2.6, give rise to systematic errors in the density. To determine these errors, we can first express the average atom number for a site i in terms of the probabilities for finding a single or double occupancy there:

$$\langle N_i \rangle = P_s^{(i)} + 2P_d^{(i)} \tag{6.1}$$

From the uncertainties in assigning single and double occupancies, we obtain the total uncertainty using error propagation:

$$\sigma_N = \sqrt{\left(\frac{\partial \langle N \rangle}{\partial P_s}\right)^2 \sigma_s^2 + \left(\frac{\partial \langle N \rangle}{\partial P_d}\right)^2 \sigma_d^2 + 2\frac{\partial \langle N \rangle}{\partial P_s}\frac{\partial \langle N \rangle}{\partial P_d}\sigma_{sd}}$$
$$= \sqrt{\sigma_s^2 + 4\sigma_d^2 + 4\sigma_{sd}} \tag{6.2}$$

where σ_{sd} is the covariance between the uncertainty of single and double occupancy.

A further possible error is the false assignment of a single atom to a hole or vice versa. Based on the fluorescence histogram in Fig. 5.4(b), this error is less than 1% of the total $N = 1$ signal in the dense regions, thus the upper bound is taken as

$\sigma_{s(h)} = 0.01P_s$. This error is added as an uncorrelated contribution to σ_s, as it only affects P_s:

$$\sigma_N = \sqrt{\sigma_s^2 + \sigma_{s(h)}^2 + 4\sigma_d^2 + 4\sigma_{sd}} \tag{6.3}$$

Concerning the false assignment of double occupancies, there are two types of systematic errors we need to distinguish:

- We can falsely declare a doubly occupied site to contain a single atom, with a relative error of up to 28% of P_d, i.e. $\sigma = 0.28P_d$. This type of error leads to an underestimation of density, because we miss the second atom on the site.

- We can falsely declare a singly occupied site to contain a double occupancy, with a relative error of 2.5% of P_s, i.e. $\sigma = 0.025P_s$. This error leads to an overestimation of density, because we assign to a site a second atom which is not there.

In both cases, the errors in single and double occupancy are fully anticorrelated: If we assign a doubly occupied site as a single atom, we have one $N = 2$ instance too few and one $N = 1$ instance too many in the statistics, and vice versa. For the first case, where we underestimate the density, the errors are given by $\sigma_d^+ = \sigma_s^+ = 0.28P_d$. Due to the anticorrelation, the covariance is $\sigma_{sd}^+ = -\sigma_s^+ \sigma_d^+ = -(0.28P_d)^2$. For the second case, where we overestimate the density, the errors are given by $\sigma_s^- = \sigma_d^- = 0.025P_s$ and the covariance is $\sigma_{sd}^- = -(0.025P_s)^2$.

   Inserting these two categories of errors into Eq. (6.3) gives us the total uncertainties σ_N^+ and σ_N^-, from which the shaded area of Fig. 6.1(b) is obtained. The absolute error is quite low due to the small relative error on the single occupancies and the small number of double occupancies, for which we have the largest uncertainty.

6.2   Atom number fluctuations

An interesting observable in this measurement set is the fluctuation of atom numbers on each site, where we see a striking signature of the fermionic nature of the atoms: The fluctuations are strongly suppressed compared to the classical limit of Poissonian number statistics. This reduction of density fluctuations in degenerate Fermi gases have been measured in optical traps [62, 63] and provide clear evidence of Pauli blocking. This will be derived in the following.

6.2.1 Number fluctuations in Fermi gases

Consider a set of discrete, non-degenerate eigenstates $\{|j\rangle\}$ populated by identical fermions. The total atom number operator of the system is given by:

$$\hat{N} = \sum_j \hat{a}_j^\dagger \hat{a}_j = \sum_j \hat{n}_j \tag{6.4}$$

where the individual number operators $\hat{n}_j$ have eigenvalues n_j of 0 or 1.

In general, the local populations $\langle \hat{n}_j \rangle$ undergo fluctuations. Working in a grand canonical ensemble, also the total atom number in the system fluctuates. We characterise the total number fluctuations by the variance:

$$(\Delta N)^2 = \langle \hat{N}^2 \rangle - \langle \hat{N} \rangle^2 = \sum_j \left(\langle \hat{a}_j^\dagger \hat{a}_j \hat{a}_j^\dagger \hat{a}_j \rangle - \langle \hat{a}_j^\dagger \hat{a}_j \rangle \langle \hat{a}_j^\dagger \hat{a}_j \rangle \right) \tag{6.5}$$

where we assume that the numbers n_j and n_i in two states are uncorrelated, thus we can neglect any covariances. Making use of the anticommutation relation (2.1b), we can express the first term of the sum as

$$\langle \hat{a}_j^\dagger \hat{a}_j \hat{a}_j^\dagger \hat{a}_j \rangle = \langle \hat{a}_j^\dagger \hat{a}_j \rangle - \cancel{\langle \hat{a}_j^\dagger \hat{a}_j^\dagger \hat{a}_j \hat{a}_j \rangle} \tag{6.6}$$

where the second term drops out due to the properties of fermions that $\hat{a}\hat{a}$ or $\hat{a}^\dagger \hat{a}^\dagger$ operating on any arbitrary state gives zero. Inserting (6.6) back into (6.5) gives [241, 242]:

$$(\Delta N)^2 = \sum_j \left(\langle \hat{a}_j^\dagger \hat{a}_j \rangle - \langle \hat{a}_j^\dagger \hat{a}_j \rangle \langle \hat{a}_j^\dagger \hat{a}_j \rangle \right) = \sum_j \langle \hat{n}_j \rangle \left(1 - \langle \hat{n}_j \rangle \right) \tag{6.7}$$

We find that the variance is always smaller than the mean atom number $\langle \hat{N} \rangle = \sum_j \langle \hat{n}_j \rangle$, which is a special property of fermions. In the limit where the levels are very sparsely populated, i.e. $\langle \hat{n}_j \rangle \ll 1$, we have

$$(\Delta N)^2 \approx \sum_j \langle \hat{n}_j \rangle = \langle \hat{N} \rangle \tag{6.8}$$

which is a property of Poissonian number statistics. This case applies to classical ideal gases [241]. In the opposite limit, where almost all states are populated, i.e. all $\langle \hat{n}_j \rangle \approx 1$, the variance tends to zero. Therefore in the low-density limit, a Fermi gas behaves like a classical gas with respect to atom number fluctuations, but in the degenerate regime, the number fluctuations are suppressed.
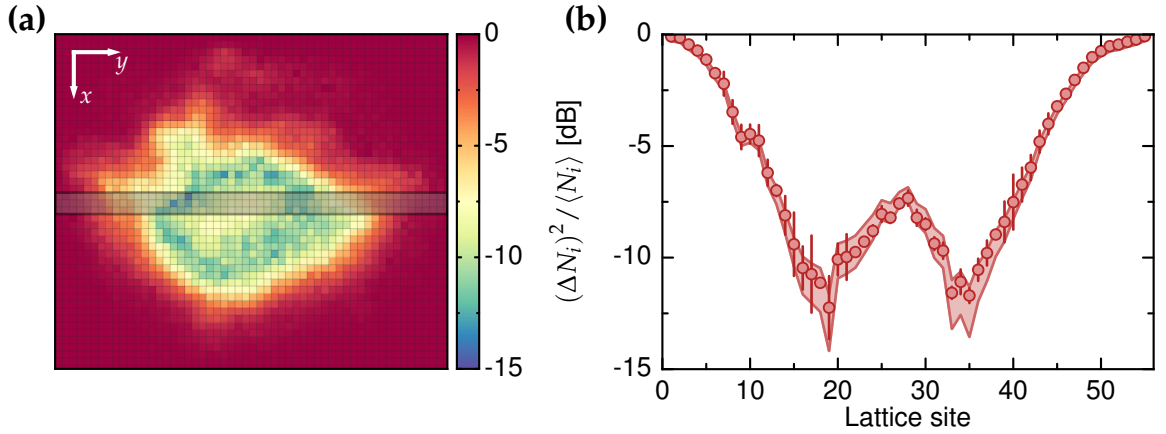
Figure 6.2: Suppression of atom number fluctuations in the band-insulating regime. (a) 2D distribution of relative occupation-number variance for a band insulator. **(b)** Horizontal cut through the 2D plot with an average over three neighbouring lattice sites (grey area of Fig. (a)). The error bars show the statistical uncertainty of the averaging, and the shaded areas display the systematic error due to reconstruction uncertainties.

6.2.2 Measurement of fluctuations

In the measured data set of band insulators, we quantify the density fluctuations by the variance of the atom number on each individual lattice site:

$$(\Delta N_i)^2 = \langle N_i^2 \rangle - \langle N_i \rangle^2 \tag{6.9}$$

whereas N_i is a sum over the numbers on the local vibrational states on the given site, as in Eq. (6.5). We evaluate the number variance on each site for the hundreds of images and compare it with the mean atom number on that site. The corresponding 2D plot in Fig. 6.2**(a)** shows the normalised ratio on a logarithmic scale:

$$\frac{(\Delta N_i)^2}{\langle N_i \rangle} = \frac{\langle N_i^2 \rangle - \langle N_i \rangle^2}{\langle N_i \rangle} \tag{6.10}$$

We find that towards the edge of the system, the ratio $(\Delta N_i)^2/\langle N_i \rangle$ tends to 1 where the density is low. In the central region, where the density is at almost unity filling, the variance is suppressed by an order of magnitude with respect to the mean atom number. At the centre of the trap, where double occupancies accumulate, the fluctuations slightly increase again. This is clear evidence of Pauli blocking in the band-insulating core of the system.

The systematic error of the term (6.10) is estimated along similar lines to the previous Section 6.1. We express the relative variance in terms of the probabilities for

single and double occupancies by using the following expressions:

$$\langle N_i \rangle = \sum_m m P_m^{(i)} = P_s^{(i)} + 2P_d^{(i)}$$

$$\langle N_i \rangle^2 = \left(P_s^{(i)}\right)^2 + 4P_s^{(i)}P_d^{(i)} + 4\left(P_d^{(i)}\right)^2 \tag{6.11}$$

$$\langle N_i^2 \rangle = \sum_m m^2 P_m^{(i)} = P_s^{(i)} + 4P_d^{(i)}$$

Inserting these into Eq. (6.10), we can evaluate the systematic uncertainty of the variance by propagating the correlated errors σ_s and σ_d using a formula like (6.2). Once again, the error is asymmetric and the maximum possible underestimation and overestimation of the atom numbers are taken separately into account.

6.3 Entropy

The number statistics give us access to the occupation probabilities, from which we can deduce the entropy on each lattice site.

6.3.1 Entropy of Fermi gases

Consider a system with a fixed set of single-particle energy levels and different possible particle numbers distributed among them. The system can be characterised in terms of a set of microstates $\{|\mu\rangle\}$, each one describing a fixed particle number and a fixed energy. The occupation probabilities of the different microstates p_μ can be used to fully characterise the system properties. In particular, the entropy of the system is defined in terms of these occupational probabilities alone [241]:

$$S = -k_B \sum_\mu p_\mu \ln p_\mu \tag{6.12}$$

For simple quantum systems, the possible microstates are easy to construct. An important requirement is to ensure the probabilities p_μ are correctly normalised. This requires careful enumeration of *all* possible configurations, which becomes more difficult, the more complex the system is.

If the structure of the single-particle levels is known, one can derive a different but equivalent form of Eq. (6.12), which is simpler to apply to complex level structures. Consider a set of energy levels labeled by an index j, where we now assume γ_j degenerate single-particle states that belong to each energy level j, and $N_j < \gamma_j$ identical, noninteracting fermions distributed among them. The number of possibilities W_j of distributing N_j fermions among the γ_j degenerate sublevels without populating a sublevel twice is simply the number of possibilities to select N_j out of γ_j objects:

$$W_j = \binom{\gamma_j}{N_j} = \frac{\gamma_j!}{N_j!(\gamma_j - N_j)!} \tag{6.13}$$

The total number of possible microscopic configurations in the full set of energy levels is $W = \prod_j W_j$, from which we can obtain the entropy of the system:

$$S = k_B \ln W = k_B \sum_j \ln W_j \tag{6.14}$$

Inserting Eq. (6.13) into (6.14) gives:

$$S = k_B \sum_j \left[\ln \gamma_j! - \ln N_j! - \ln (\gamma_j - N_j)! \right] \tag{6.15}$$

If γ_j and N_j are large, either because the system is very large or because we have many realisations of the same small system, we can apply Stirling's approximation $\ln m! \approx m \ln m - m$. Also, using the fact that the mean population of an energy level is given by $p_j = N_j/\gamma_j$, we can factor out γ_j and use $\ln (\gamma_j - N_j) = \ln \gamma_j + \ln (1 - p_j)$. This gives [241]:

$$S = -k_B \sum_j \gamma_j \left[p_j \ln p_j + (1 - p_j) \ln (1 - p_j) \right] \tag{6.16}$$

For this entropy formula, we did not assume thermal equilibrium, therefore it is always valid for any system for which the mean populations p_j are known. If the system were in thermal equilibrium, the p_j would be given by the Fermi-Dirac distribution [243, 244]:

$$p_j = f(\varepsilon_j) = \frac{1}{\exp\left(\frac{\varepsilon_j - \mu}{k_B T}\right) + 1} \tag{6.17}$$

where ε_j is the energy of the level j, μ is the chemical potential, and T is the temperature.

However in our case, we load a single-component Fermi gas from a 2D trap into a lattice. An energy gap is opened in the quasi-momentum distribution at $q = \pm\pi/a_{latt}$, a manifestly non-adiabatic process. Atoms near the edge of the newly formed Brillouin zone can get excited into a higher band, from which they cannot relax into the ground band due to the absence of s-wave collisions, a necessary process for thermalisation. Without thermalisation, the notion of temperature breaks down after this process and the description with a Fermi-Dirac distribution becomes invalid.

Nevertheless, we can still work with the p_j as generic probabilities, which we match to the experimentally measured probabilities for the different configurations. This requires a few assumptions about the structure of energy levels on each site.

6.3.2 Two-level sites

To find how to apply Eq. (6.16) to our measurement, we construct a toy model to relate the measured number statistics to single-particle states. Consider a single lattice site, which we model as a two-level system, and identical fermions that can populate the two states. Let the probability for the level i to be occupied be p_i, and thus the probability for the level to be unoccupied is $1 - p_i$. As both states are independent, we can easily express the probabilities for the two-level system to be unoccupied (P_h), singly occupied (P_s) or doubly occupied (P_d):

$$
\begin{aligned}
P_h &= (1 - p_1)(1 - p_2) \\
P_s &= p_1(1 - p_2) + (1 - p_1)p_2 \\
P_d &= p_1 \cdot p_2
\end{aligned}
\tag{6.18}
$$

We can resolve these equations with respect to p_1 and p_2 and express them in terms of the probabilities P_h and P_d, which are accessible experimentally (P_s is not an independent variable as $P_h + P_s + P_d = 1$, by construction). There are two valid solutions:

$$
p_i = \frac{1 + P_d - P_h}{2} \pm \sqrt{\frac{(1 + P_d - P_h)^2}{4} - P_d}
\tag{6.19}
$$

p_1 and p_2 necessarily have different signs, but without any further conditions, there is no way to determine which sign is valid for which level, as the problem is symmetric. However, we simply make the physical assumption that the lower level always has the bigger occupation probability than the higher one. In this case, the probabilities are:

$$
\begin{aligned}
p_1 &= \frac{1 + P_d - P_h}{2} + \sqrt{\frac{(1 + P_d - P_h)^2}{4} - P_d} \\
p_2 &= \frac{1 + P_d - P_h}{2} - \sqrt{\frac{(1 + P_d - P_h)^2}{4} - P_d}
\end{aligned}
\tag{6.20}
$$

If we assumed that each lattice site corresponded to a two-level system, we could simply insert this result into the formula (6.16) to obtain the entropy on every site.

6.3.3 Multi-level sites

A more precise description of our system is that there is an excited band for each direction. The excited bands for the x- and y-lattices lie $23\,\text{kHz}$ above the ground band, and the z-lattice has a lower-lying excited band with a gap of $14\,\text{kHz}$.

As we start with presumably all atoms in the ground band of the vertical lattice, one could assume that no excitations occur along this direction because there is almost no coupling to the *x*- and *y*-directions during the lattice ramp-up. Therefore, one could argue that there are only two possible excited bands, and model the system as before with a two-fold degenerate upper level while neglecting the excited *z*-band. However, the most conservative model is that we have three equivalent excited levels, because this gives the highest possible entropy of the system. We use this to get a reliable upper bound for the entropy.

We repeat the analysis in the same spirit as before. Here, we use the probabilities for the site to be singly occupied or doubly occupied, which we model as follows:

$$P_s = p_1(1 - p_2)^3 + 3p_2(1 - p_1)(1 - p_2)^2 \tag{6.21a}$$

$$P_d = 3p_1 p_2(1 - p_2)^2 + 3p_2^2(1 - p_1)(1 - p_2) \tag{6.21b}$$

Eq. (6.21a) expresses the probability to have either a single fermion in the lower level with the upper the unoccupied, or three ways of putting a single fermion in an upper level while keeping the rest empty. Eq. (6.21b) gives the probability for six different configurations: Three with a fermion in the lower level and one in an upper level, and three others with two fermions in upper levels.

There is no closed analytical expression for p_1 and p_2 to be derived from this system of equations, therefore one has to solve them numerically. After getting p_1 and p_2, we can then plug them into Eq. (6.16) with $\gamma_1 = 1$ and $\gamma_2 = 3$ to get the entropy per site. This gives the data shown in Fig. 6.3**(a)**. We see an accumulation of entropy in the centre of the trap, where double occupancies are most likely to occur, and on the edge of the cloud where the density goes down. In the region in between, the entropy is low where the filling fraction is very high. Far outside the cloud, where there are no atoms, the entropy goes to zero.

Fig. 6.3**(b)** shows an averaged cut through the data. The estimate of systematic errors is done by numerical error propagation of the maximum possible deviations of single and double occupancies in both directions, while taking the anticorrelation between the errors into account, as described in Section 6.1.

Normalising the entropy to the local density gives the entropy per atom, shown in Figs. 6.3**(c)** and 6.3**(d)**. We find a low entropy in the trap centre and a diverging entropy per atom towards the edge of the cloud. The lowest entropy is given by $0.34(10)k_B$, taking all uncertainties into account.

6.3.4 Entropy thermometry

Despite the lack of thermal equilibrium in the system, we can make use of the entropy measurement to place an upper bound on our initial temperature in the 2D trap before
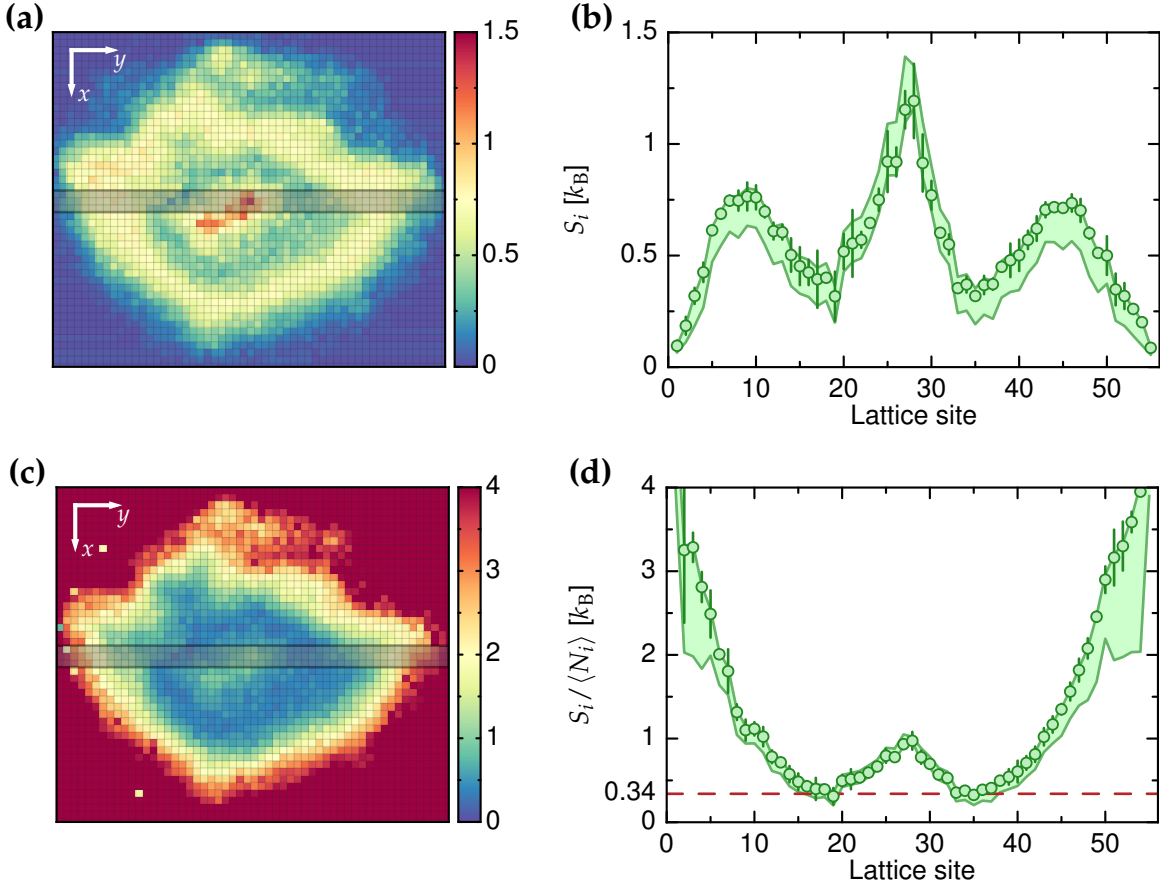
Figure 6.3: System entropy, assuming a ground state and three equal excited levels per site. (a) 2D distribution of entropy per site. The entropy is concentrated around the centre, where double occupancies accumulate, and the wings where the density fluctuations dominate. **(b)** Averaged cut through the 2D plot. The error bars show the statistical uncertainty of the averaging, and the shaded areas display the systematic error due to reconstruction uncertainties. **(c)** 2D distribution of entropy per atom. The entropy per atom is low in the centre of the cloud and diverges outside the wings. In the trap centre, the double occupancies cause an increase in entropy. **(d)** Averaged cut through the 2D plot. The error bars show the statistical uncertainty of the averaging, and the shaded areas display the systematic error due to reconstruction uncertainties. The minimum entropy per atom is around $0.34(10)k_B$.

turning on the lattice. If the processes of spin polarising the sample and ramping up the lattice are adiabatic, then the measured entropy in the lattice would be equal to the entropy in the trap. The Fermi energy is typically much larger than the energy level spacing in the harmonic trap, so one can apply a semi-classical approximation and relate the Fermi gas temperature to the entropy via [242, 245]:

$$S \approx \frac{d}{3}\pi^2 N k_B \frac{T}{T_F} \tag{6.22}$$

where $d = 2$ is the dimensionality of the initial trap. Summing the total entropy of the system in Fig. 6.3**(a)** and dividing by the total atom number given by the density, we find an average entropy per atom of $S/N = 1.05(5)k_B$. According to Eq. (6.22), this corresponds to an initial temperature of $T_{ini} = 0.16(1)T_F$. As the spin polarisation and lattice ramp-up might entail some non-adiabaticity, the initial entropy, and therefore the temperature, may be lower.

Furthermore, the entropy per atom on the order of k_B illustrates the power of quantum gas microscopy for studying strongly correlated systems. A global measurement of system observables would not allow for detecting local phases of low entropy. But with single-site resolution, we can isolate regions of entropy three times lower than the average and study them individually. This will be instrumental for investigating the different phases of the Fermi-Hubbard model.

6.4 Density-density correlations

With ultracold gases, two-point correlation functions have often been used to extract information that goes beyond what is accessible from the average density distributions. This has allowed for studying many-body phases in new ways [61, 100, 101, 117, 246, 247]. With the number statistics at our disposal, we can measure the two-point density correlations in the band insulator. It will be shown that the correlations are related to the compressibility of the system.

We start with a density-density correlation function defined as:

$$\begin{aligned}
c_n(\vec{r}_1, \vec{r}_2) &= \langle \hat{\psi}_1^\dagger \hat{\psi}_2^\dagger \hat{\psi}_2 \hat{\psi}_1 \rangle - \langle \hat{\psi}_1^\dagger \hat{\psi}_1 \rangle \langle \hat{\psi}_2^\dagger \hat{\psi}_2 \rangle \\
&= \langle \hat{\psi}_1^\dagger \hat{\psi}_1 \hat{\psi}_2^\dagger \hat{\psi}_2 \rangle - \langle \hat{\psi}_1^\dagger \hat{\psi}_1 \rangle \delta(\vec{r}_1 - \vec{r}_2) - \langle \hat{\psi}_1^\dagger \hat{\psi}_1 \rangle \langle \hat{\psi}_2^\dagger \hat{\psi}_2 \rangle \\
&= \langle \hat{n}_1 \hat{n}_2 \rangle - \langle \hat{n}_1 \rangle \langle \hat{n}_2 \rangle - \langle \hat{n}_1 \rangle \delta(\vec{r}_1 - \vec{r}_2)
\end{aligned} \tag{6.23}$$

where the $\hat{\psi}_k = \hat{\psi}(\vec{r}_k)$ are fermionic field operators, and we have used the anticommutation relations in Eqs. (2.1a) and (2.1b) to rearrange the term $\hat{\psi}_1^\dagger \hat{\psi}_2^\dagger \hat{\psi}_2 \hat{\psi}_1$. The operators $\hat{n}_k = \hat{n}(\vec{r}_k) = \hat{\psi}_k^\dagger \hat{\psi}_k$ simply correspond to the number density. The brackets

$\langle . \rangle$ denote the ensemble average.

Instead of continuous distances $\vec{r}$, we have discrete lattice sites, and from the reconstructed images we have access to the atom numbers N_i rather than number densities. We can evaluate a correlation function defined similar to (6.23):

$$C(\vec{r}_i, \vec{r}_j) = \langle N_i N_j \rangle - \langle N_i \rangle \langle N_j \rangle - \langle N_i \rangle \, \delta_{ij} \tag{6.24}$$

The analysis is based on the 425 reconstructed and digitised images of bands insulators, such as that in Fig. 6.4(b). We have access to the number N_i on the sites with discrete positions $\vec{r}_i$. The correlation function (6.24) is evaluated for a given displacement $\vec{a}$ between the two positions $\vec{r}_i$ and $\vec{r}_j$, whereas we use the average over all images for each site as the ensemble average. To do this efficiently, a copy of the entire image is displaced by the vector $\vec{a}$ and multiplied by the original one in the overlap region, as in Fig. 6.4(a). This is done for all images of the data set, and all results are averaged. Finally, the average densities in the overlap region for the displaced and non-displaced grids are calculated and subtracted.

For small displacements $\vec{a}$, we observe small but finite density correlations at the edge of the cloud and around the centre (Figs. 6.4(c) and 6.4(d)). This hints towards a relation between the atom number fluctuations and the density correlations. For larger displacements, the density correlations in the centre vanish, as seen in Fig. 6.4(e).

If we are only interested in the correlation vs. distance, we can perform a further average of $C(\vec{r}_i, \vec{r}_j)$ over all lattice sites around the central region:

$$g^{(2)}(\vec{a}) = \frac{\sum_i C(\vec{r}_i, \vec{r}_i + \vec{a})}{\sum_i} \tag{6.25}$$

The result is shown in Fig. 6.5(a). A radial average, shown in Fig. 6.5(b), shows that that biggest correlations are found for short distances. At $\vec{a} = 0$, the value of $g^{(2)}$ is -1, which arises from the subtraction of $\langle N_i \rangle \, \delta_{ij}$ in (6.24).

It can be shown that the sum of the correlation function $g^{(2)}(\vec{a})$ over all positions within a given volume is related to the total atom number fluctuations in that volume via [241]:

$$\sum_{\vec{a}} g^{(2)}(\vec{a}) = \frac{\langle (\Delta N)^2 \rangle}{\langle N \rangle} - 1 \tag{6.26}$$

and, if the system were in thermal equilibrium, that the atom number fluctuations are related to the isothermal compressibility κ_T [241]:

$$(\Delta N)^2 = k_{\mathrm{B}} T \left(\frac{\partial N}{\partial \mu} \right)_{T,V} =: k_{\mathrm{B}} T \, \langle N \rangle \, \kappa_T \tag{6.27}$$

(a)

(b)

(c)

(d)

(e)
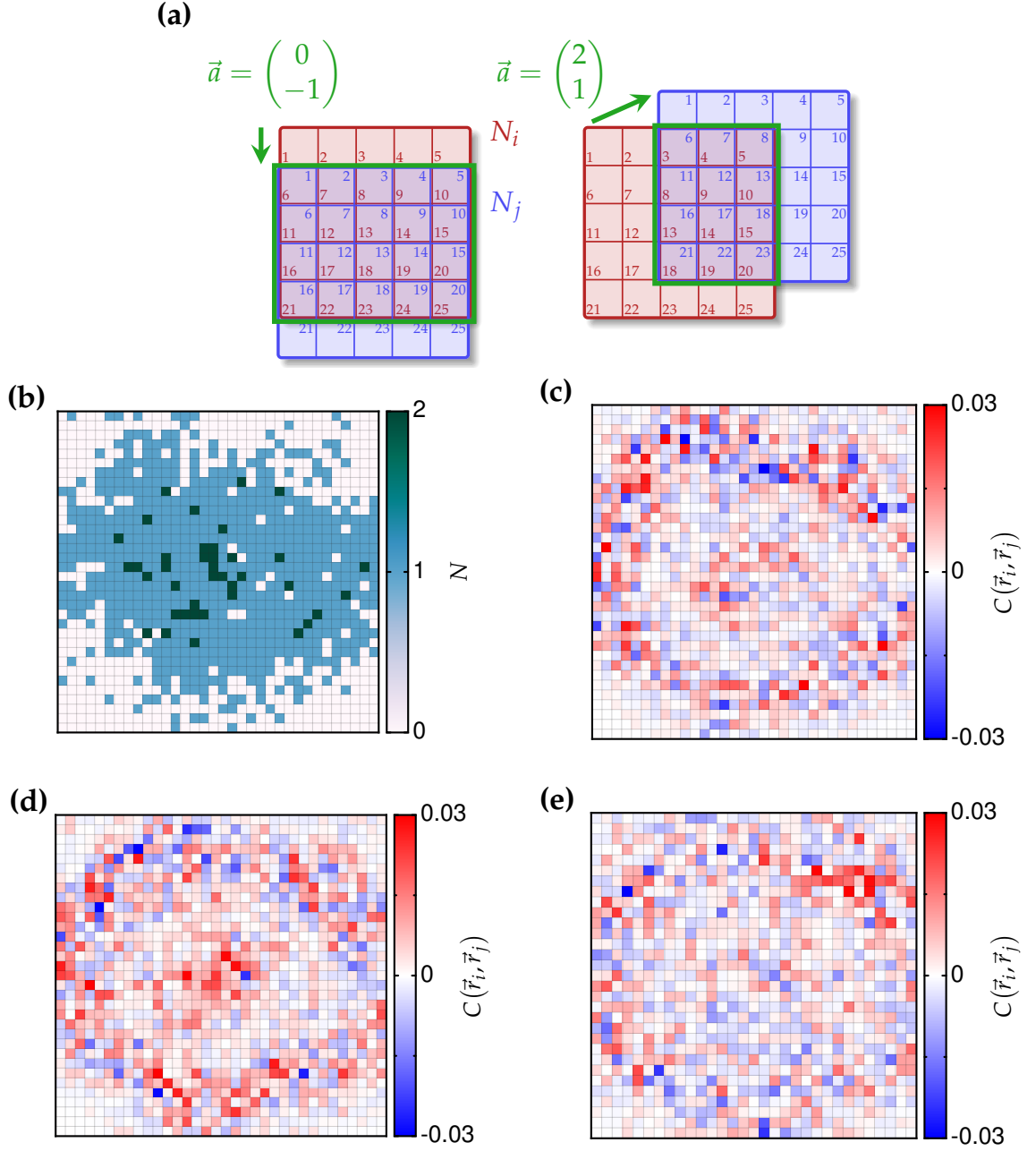
Figure 6.4: Two-point density correlation function. Local correlations are detected at the edges of the cloud and in the centre, but mostly at short ranges. **(a)** Method for obtaining the correlation function $C(\vec{r}_i, \vec{r}_j)$. An array of lattice sites from an image (red grid) is shifted by a discrete vector $\vec{a}$. The resulting (blue) grid is multiplied with the original one in the overlapping region marked by the green rectangle. Repeating the same operation for all images and a given $\vec{a}$, and then averaging yields $\langle N_i N_j \rangle$. **(b)** Single digitised image of a band insulator. **(c)** Local correlation for $\vec{a} = (1, 0)$. **(d)** Local correlation for $\vec{a} = (0, 1)$. **(e)** Local correlation for $\vec{a} = (3, 3)$.
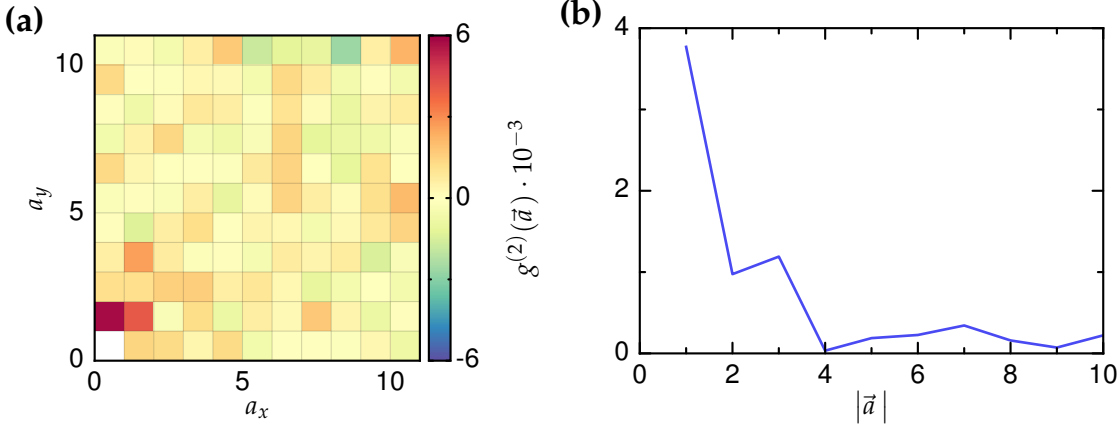
Figure 6.5: Correlation function $g^{(2)}(\vec{a})$**. (a)** Density correlation function averaged over the central 11×11 sites. The white pixel on the bottom left corresponds to $g^{(2)}(0) = -1$. **(b)** Radial average of $g^{(2)}$. The biggest density correlations are found at short ranges.

which is a consequence of the fluctuation-dissipation theorem [248]. Inserting (6.27) into (6.26) gives:

$$\sum_{\vec{a}} g^{(2)}(\vec{a}) = k_{\mathrm{B}} T \kappa_T - 1 \qquad (6.28)$$

The -1 on the right-hand side already arises due to $g^{(2)}(0)$. If the other contributions at finite $\vec{a}$ have any finite value, this means that the compressibility has to be nonzero. Conversely, we detect finite correlation signals in regions where the compressibility is finite, and in the band-insulating ring with almost unity filling the density correlations vanish. Such a link between compressibility and density-density correlation functions has been investigated for Mott [249] and band insulators [148].

There are a few points where one must be cautious:

- The on-site atom numbers N_i used in the correlation function (6.24) are not entirely equivalent to the densities $\hat{n}_i$ used in the correlation function (6.23), as the $\hat{n}_i$ are defined in terms of fermionic operators and therefore can only have eigenvalues 0 or 1, whereas we can measure 0, 1 or 2 for the N_i. The N_i can accommodate atoms that populate different bands. Nevertheless, $\langle N_i \rangle$ can be expressed as $\left\langle \sum_k \hat{n}_i^{(k)} \right\rangle$, where k is a band index. Inserting this into Eq. (6.24) and using the fact that the numbers of different bands are mutually uncorrelated, the expression reduces to the sum of correlations of the form (6.23) for the different bands.

- The assignment of a temperature in the relation (6.28) is not correct, especially as

Eq. (6.23) can be derived from a grand-canonical partition function, which in this case is not applicable. On the other hand, it has been recently shown that non-interacting gases of fermions can converge to systems that resemble thermalised systems and can be described using generalised Gibbs ensembles [250, 251].

Summary

We measured statistical properties of a spin-polarised Fermi gas with a band-insulating region in the centre. Clear signatures of Fermi statistics appeared in the signal, namely a plateau in density and a strong suppression of density fluctuations. A low entropy per atom of $0.34k_B$ was measured, and the entropy was used as a thermometer to characterise the initial equilibrium temperature of the gas. Density-density correlations were used as an alternative way to probe the incompressibility of the band insulator.

These measurements provide a successful benchmark of our system and represent the first single-site imaging experiments with fermions in a quantum degenerate regime.

Chapter 7

Conclusion and outlook

This thesis reported on the realisation of a new-generation quantum gas microscope for fermionic ^{6}Li in optical lattices. We apply standard techniques of laser cooling to produce cold clouds of ^{6}Li in two spin components. The first step of laser cooling is along the principal 671 nm line, and the second step is along the 323 nm transition, which possesses a narrower linewidth and a lower Doppler limit. A homebuilt laser system produces the UV light for narrow-line cooling by sum-frequency generation of two infrared wavelengths and subsequent second-harmonic generation. The frequency is stabilised to a hyperfine transition of molecular iodine.

Following the laser cooling, we apply evaporative cooling and optical transport to produce a degenerate Fermi gas. A tightly confining dimple trap allows for loading a single 2D plane of a vertical optical lattice, where we perform magnetically driven evaporative cooling. We then ramp on a lattice in the plane with a lattice constant of 1.16 μm, larger than for quantum gas microscopes that have been previously built. The atoms are then transferred into a deep and short-scaled pinning lattice, where we perform Raman sideband cooling to scatter photons while suppressing the recoil heating. With a high-resolution microscope objective with a numerical aperture of NA $= 0.5$, we can image the fluorescing atoms with high fidelity larger than 95%.

This implementation of the microscope is conceptually different from previous ones. With the short-scaled pinning lattice, the system under study is separate from the detection, allowing for more flexibility in the lattice geometry. Furthermore, we found that the pinning lattice provides a new way to avoid pairwise losses of atoms originating from the same lattice site. Due to the oversampling of the physics lattice sites, these pairs can be split into different wells of the pinning lattice, where they do not undergo these losses. This gives direct access to the true number statistics on every site.

Using these tools, we investigated a dense sample of spin-polarised fermions in the lattice with a very high filling fraction in the centre of the system. We detected a flattening of the density profile towards the centre of the cloud, consistent with a decrease of compressibility. This could also be seen in density-density correlations, where incompressibility leads to an absence of correlations. Using the access to the

on-site number statistics, the atom number fluctuations were found to be highly suppressed in the central region, which is expected for band-insulating states, and a clear signature of Pauli blocking. The local entropy could be evaluated on a single site level and was found to be as low as $0.34k_B$ per atom. Despite the lack of thermalisation in the band-insulating region, the entropy could be used as a thermometer to place an upper bound on the starting temperature of the system before it was loaded into the lattice. These observations represent the first microscopic measurements on a degenerate Fermi gas on the single-atom level.

Current developments

Since the data for this thesis was taken, more progress has been made on improving the machine. This progress will be described in more detail in the PhD theses of Martin Boll and Timon Hilker.

The high-resolution imaging setup has undergone several improvements. Careful alignment of the objective position and tilt angle has allowed for a major improvement in the point-spread-function. Some apertures on mechanical elements that possibly clipped the signal have been enlarged or removed. The magnification of the imaging setup was changed from 35 to 60, leading to better sampling of each atom signal on the camera. This reduced the uncertainty in fitting the PSF position and width.

The reconstruction algorithm has been overhauled, allowing for more reliable and much faster reconstruction. Instead of fitting each lattice site with a Gaussian and determining the amplitude, the image is now deconvolved with the real averaged PSF, such that every atom signal ideally collapses onto a single pixel. The total counts within a lattice site are taken as a measure for the atom number. This method has previously been used to overcome the diffraction limit in fluorescence imaging [252]. Together with the improved PSF, it gave a better reconstruction fidelity and reduced the effect of atom signals intruding into neighbouring sites. The counts for $N = 1$ and $N = 2$ are on average much more distinguishable, and the relative uncertainty in assigning a double occupancy is now 10% instead of 28%.

By simply omitting the removal of one spin component described in Section 4.3.3, we could easily start with a spin mixture of $|1\rangle$ and $|2\rangle$ in the lattice. Repulsive interactions enabled us to observe the crossover into the Mott insulating regime. Imaging of Mott insulators with ^{6}Li and single-site resolution had already been reported in [165].

The problem with two spin components was that the splitting of two different spins on the same lattice site into different pinning lattice wells was only probabilistic as they were not separated in energy. This led to many losses of atom pairs due to light-assisted collisions. However, with the aid of strong repulsive interactions using the Feshbach field, the probability for splitting the pair could be increased. Taking

into account that the adiabaticity in this process is given for much slower ramps of the pinning lattice, the fidelity of detecting double occupancies could be considerably improved, leading to clear images of a two-component band insulator.

Future experiments

The experiment is designed to be a useful quantum simulator for the Fermi-Hubbard model, which was discussed in Sections 2.2.2 through 2.2.4. The following features are part of the longer-term goals of the experiment to realise this goal or study other physical models:

- **Superlattices.** The use of superlattices opens up many new possibilities and is, in combination with site-resolved imaging, a unique feature of our experiment. With the possibility of using 2×2 plaquettes, we could study resonant valence bond states [253] or topological phases [254]. Furthermore, with superlattices we could possibly prepare antiferromagnetically ordered states by adiabatic splitting of spin singlets into double wells and then coupling neighbouring singlets [255]. This approach is promising due to the very low initial entropy.

- **Spin-resolved imaging.** The atoms start in a node of the large-scaled vertical lattice with $3\,\mu$m spacing. By slowly ramping up the short-scaled lattice, the plane can be split into two. If we simultaneously apply a magnetic gradient field in the vertical direction, different spin components can be deterministically split in opposite directions. Shifting the relative phase of both lattices by π and ramping down the short-scaled lattice brings the atoms to a separation of a full plane. This can be repeated several times until we can image each component while the other is out of focus [238].
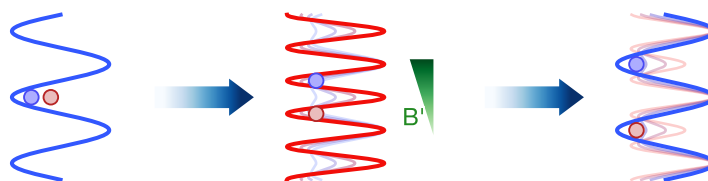
Being able to measure spin correlation functions over many lattice sites would represent a major step forward in quantum gas microscopy and will be instrumental in probing quantum magnetism [97, 98].

- **Arbitrary light patterns.** We plan to implement a digital spatial light modulator [256]. This will enable us to perform multi-site addressing, thereby preparing a well defined initial density or spin distribution [113]. It will also allow

for projecting arbitrary light potentials onto the atoms, setting novel boundary conditions. For example, the use of 1D superlattices and together with optical "hard-wall" potentials can be used to probe solitons in the Su-Schrieffer-Heeger model [257]. In general, hard walls are useful for probing topological edge states [258, 259].

- **Fermions in 1D.** The regime of fermions in one dimension has been studied theoretically [260–262] but many aspects of this regime remain largely unexplored experimentally. The breakdown of individual excitations and the separation of charge and spin are of particular interest [263]. By preparing spin-imbalanced fermions, where the Fermi energies of both components do not match, one can study superfluidity [174, 264] and FFLO phases [179, 180].

  Spin resolved imaging in 1D systems would be particularly simple: we confine the atoms to decoupled 1D chains, using the 1.16 μm lattice along the chains and the 2.32 μm lattice perpendicular to them. By applying a magnetic gradient and ramping up the short 1.16 μm lattice perpendicular to the chain, each well splits into two, while the spins deterministically get split in opposite directions. This yields the original spatial and spin distribution in a single image.

- **Systems out of equilibrium.** Ultracold atom systems are generally readily tunable, which allows for performing sudden quenches of a system parameter and observing subsequent dynamics [114, 116, 265, 266]. The question of how quantum systems out of equilibrium relax is a topic of active research (see [267] and references therein). It is assumed that integrable quantum systems do not relax to equilibrium states [268, 269]. We can probe the Fermi-Hubbard model in two limiting cases: one with vanishing interactions, where the system is integrable and does not thermalise, and another with finite interactions with the possibility to relax to equilibrium. The breakdown of integrability for finite interactions can be investigated for a quenched or driven system.

Bibliography

[1] W. Pauli. *Über den Zusammenhang des Abschlusses der Elektronengruppen im Atom mit der Komplexstruktur der Spektren*. Z. Phys. **31**, 765 (1925). (Cited on page **1**)

[2] F. J. Dyson. *Ground-state energy of a finite system of charged particles*. J. Math. Phys. **8**, 1538 (1967). (Cited on page **1**)

[3] F. J. Dyson and A. Lenard. *Stability of matter I*. J. Math. Phys. **8**, 423 (1967). (Cited on page **1**)

[4] A. Lenard and F. J. Dyson. *Stability of matter II*. J. Math. Phys. **9**, 698 (1968). (Cited on page **1**)

[5] K. v. Klitzing, G. Dorda, and M. Pepper. *New method for high-accuracy determination of the fine-structure constant based on quantized Hall resistance*. Phys. Rev. Lett. **45**, 494 (1980). (Cited on page **1**)

[6] L. D. Landau. *The theory of a Fermi liquid*. J. Exp. Theor. Phys. **30**, 1058 (1956). (Cited on page **1**)

[7] E. M. Lifshitz and L. P. Pitaevskii. *Statistical physics, part 2*. Pergamon Press Ltd. (1980). (Cited on page **1**)

[8] A. Fert. *Origin, development, and future of spintronics*. Rev. Mod. Phys. **80**, 1517 (2008). (Cited on page **1**)

[9] P. A. Grünberg. *From spin waves to giant magnetoresistance and beyond*. Rev. Mod. Phys. **80**, 1531 (2008). (Cited on page **1**)

[10] J. Bardeen, L. N. Cooper, and J. R. Schrieffer. *Theory of superconductivity*. Phys. Rev. **108**, 1175 (1957). (Cited on page **1**)

[11] B. Spivak, S. V. Kravchenko, S. A. Kivelson, and X. P. A. Gao. *Transport in strongly correlated two dimensional electron fluids*. Rev. Mod. Phys. **82**, 1743 (2010). (Cited on page **1**)

[12] J. G. Bednorz and K. A. Müller. *Possible high T_c superconductivity in the Ba-La-Cu-O system*. Z. Phys. B Cond. Matt. **64**, 189 (1986). (Cited on page **1**)

[13] I. Bloch, J. Dalibard, and W. Zwerger. *Many-body physics with ultracold gases*. Rev. Mod. Phys. **80**, 885 (2008). (Cited on pages **2**, **9**, **10**, **12**, **13**, and **14**)

[14] R. P. Feynman. *Simulating physics with computers*. Int. J. Theor. Phys. **21**, 467 (1982). (Cited on page **2**)

[15] T. W. Hänsch and A. L. Schawlow. *Cooling of gases by laser radiation*. Opt. Commun. **13**, 68 (1975). (Cited on page **2**)

[16] D. J. Wineland and H. Dehmelt. *Proposed $10^{14}\Delta\nu < \nu$ laser fluorescence spectroscopy on TI^+ mono-ion oscillator III*. Bull. Am. Phys. Soc. **20**, 637 (1975). (Cited on page **2**)

[17] W. Neuhauser, M. Hohenstatt, P. Toschek, and H. Dehmelt. *Optical-sideband cooling of visible atom cloud confined in parabolic well*. Phys. Rev. Lett. **41**, 233 (1978). (Cited on page **2**)

[18] D. J. Wineland, R. E. Drullinger, and F. L. Walls. *Radiation-pressure cooling of bound resonant absorbers*. Phys. Rev. Lett. **40**, 1639 (1978). (Cited on page **2**)

[19] S. Chu, L. Hollberg, J. E. Bjorkholm, A. Cable, and A. Ashkin. *Three-dimensional viscous confinement and cooling of atoms by resonance radiation pressure*. Phys. Rev. Lett. **55**, 48 (1985). (Cited on page **2**)

[20] E. L. Raab, M. Prentiss, A. Cable, S. Chu, and D. E. Pritchard. *Trapping of neutral sodium atoms with radiation pressure*. Phys. Rev. Lett. **59**, 2631 (1987). (Cited on page **2**)

[21] P. D. Lett, R. N. Watts, C. I. Westbrook, W. D. Phillips, P. L. Gould, and H. J. Metcalf. *Observation of atoms laser cooled below the Doppler limit*. Phys. Rev. Lett. **61**, 169 (1988). (Cited on pages **2** and **18**)

[22] J. Dalibard and C. Cohen-Tannoudji. *Laser cooling below the Doppler limit by polarization gradients: simple theoretical models*. J. Opt. Soc. Am. B **6**, 2023 (1989). (Cited on page **2**)

[23] A. Aspect, E. Arimondo, R. Kaiser, N. Vansteenkiste, and C. Cohen-Tannoudji. *Laser cooling below the one-photon recoil energy by velocity-selective coherent population trapping*. Phys. Rev. Lett. **61**, 826 (1988). (Cited on page **2**)

[24] F. Diedrich, J. C. Bergquist, W. M. Itano, and D. J. Wineland. *Laser cooling to the zero-point energy of motion*. Phys. Rev. Lett. **62**, 403 (1989). (Cited on page **2**)

[25] A. L. Migdall, J. V. Prodan, W. D. Phillips, T. H. Bergeman, and H. J. Metcalf. *First observation of magnetically trapped neutral atoms*. Phys. Rev. Lett. **54**, 2596 (1985). (Cited on page **2**)

[26] W. Petrich, M. H. Anderson, J. R. Ensher, and E. A. Cornell. *Stable, tightly confining magnetic trap for evaporative cooling of neutral atoms*. Phys. Rev. Lett. **74**, 3352 (1995). (Cited on page **2**)

[27] K. B. Davis, M.-O. Mewes, M. A. Joffe, M. R. Andrews, and W. Ketterle. *Evaporative cooling of sodium atoms*. Phys. Rev. Lett. **74**, 5202 (1995). (Cited on page **2**)

[28] M. H. Anderson, J. R. Ensher, M. R. Matthews, C. E. Wieman, and E. A. Cornell. *Observation of Bose-Einstein condensation in a dilute atomic vapor*. Science **269**, 198 (1995). (Cited on page **2**)

[29] C. C. Bradley, C. A. Sackett, J. J. Tollett, and R. G. Hulet. *Evidence of Bose-Einstein condensation in an atomic gas with attractive interactions*. Phys. Rev. Lett. **75**, 1687 (1995). (Cited on page **2**)

[30] K. B. Davis, M.-O. Mewes, M. R. Andrews, N. J. van Druten, D. S. Durfee, D. M. Kurn, and W. Ketterle. *Bose-Einstein condensation in a gas of sodium atoms*. Phys. Rev. Lett. **75**, 3969 (1995). (Cited on page **2**)

[31] S. Chu, J. E. Bjorkholm, A. Ashkin, and A. Cable. *Experimental observation of optically trapped atoms*. Phys. Rev. Lett. **57**, 314 (1986). (Cited on page **2**)

[32] C. S. Adams, H. J. Lee, N. Davidson, M. Kasevich, and S. Chu. *Evaporative cooling in a crossed dipole trap*. Phys. Rev. Lett. **74**, 3577 (1995). (Cited on page **2**)

[33] M. R. Andrews, C. G. Townsend, H.-J. Miesner, D. S. Durfee, D. M. Kurn, and W. Ketterle. *Observation of interference between two Bose condensates*. Science **275**, 637 (1997). (Cited on page **2**)

[34] M.-O. Mewes, M. R. Andrews, D. M. Kurn, D. S. Durfee, C. G. Townsend, and W. Ketterle. *Output coupler for Bose-Einstein condensed atoms*. Phys. Rev. Lett. **78**, 582 (1997). (Cited on page **2**)

[35] E. W. Hagley, L. Deng, M. Kozuma, J. Wen, K. Helmerson, S. L. Rolston, and W. D. Phillips. *A well-collimated quasi-continuous atom laser*. Science **283**, 1706 (1999). (Cited on page **2**)

[36] I. Bloch, T. W. Hänsch, and T. Esslinger. *Atom laser with a cw output coupler*. Phys. Rev. Lett. **82**, 3008 (1999). (Cited on page **2**)

[37] D. S. Jin, J. R. Ensher, M. R. Matthews, C. E. Wieman, and E. A. Cornell. *Collective*

excitations of a Bose-Einstein condensate in a dilute gas. Phys. Rev. Lett. **77**, 420 (1996). (Cited on page **2**)

[38] M.-O. Mewes, M. R. Andrews, N. J. van Druten, D. M. Kurn, D. S. Durfee, C. G. Townsend, and W. Ketterle. *Collective excitations of a Bose-Einstein condensate in a magnetic trap*. Phys. Rev. Lett. **77**, 988 (1996). (Cited on page **2**)

[39] M. R. Andrews, D. M. Kurn, H.-J. Miesner, D. S. Durfee, C. G. Townsend, S. Inouye, and W. Ketterle. *Propagation of sound in a Bose-Einstein condensate*. Phys. Rev. Lett. **79**, 553 (1997). (Cited on page **2**)

[40] D. M. Stamper-Kurn, A. P. Chikkatur, A. Görlitz, S. Inouye, S. Gupta, D. E. Pritchard, and W. Ketterle. *Excitation of phonons in a Bose-Einstein condensate by light scattering*. Phys. Rev. Lett. **83**, 2876 (1999). (Cited on page **2**)

[41] J. Stenger, S. Inouye, A. P. Chikkatur, D. M. Stamper-Kurn, D. E. Pritchard, and W. Ketterle. *Bragg spectroscopy of a Bose-Einstein condensate*. Phys. Rev. Lett. **82**, 4569 (1999). (Cited on page **2**)

[42] M. R. Matthews, B. P. Anderson, P. C. Haljan, D. S. Hall, C. E. Wieman, and E. A. Cornell. *Vortices in a Bose-Einstein condensate*. Phys. Rev. Lett. **83**, 2498 (1999). (Cited on page **2**)

[43] K. W. Madison, F. Chevy, W. Wohlleben, and J. Dalibard. *Vortex formation in a stirred Bose-Einstein condensate*. Phys. Rev. Lett. **84**, 806 (2000). (Cited on page **2**)

[44] J. R. Abo-Shaeer, C. Raman, J. M. Vogels, and W. Ketterle. *Observation of vortex lattices in Bose-Einstein condensates*. Science **292**, 476 (2001). (Cited on page **2**)

[45] S. Burger, K. Bongs, S. Dettmer, W. Ertmer, K. Sengstock, A. Sanpera, G. V. Shlyapnikov, and M. Lewenstein. *Dark solitons in Bose-Einstein condensates*. Phys. Rev. Lett. **83**, 5198 (1999). (Cited on page **2**)

[46] J. Denschlag, J. E. Simsarian, D. L. Feder, C. W. Clark, L. A. Collins, J. Cubizolles, L. Deng, E. W. Hagley, K. Helmerson, W. P. Reinhardt, S. L. Rolston, B. I. Schneider, and W. D. Phillips. *Generating solitons by phase engineering of a Bose-Einstein condensate*. Science **287**, 97 (2000). (Cited on page **2**)

[47] H. Feshbach. *A unified theory of nuclear reactions II*. Ann. Phys. **19**, 287 (1962). (Cited on page **2**)

[48] C. Chin, R. Grimm, P. Julienne, and E. Tiesinga. *Feshbach resonances in ultracold gases*. Rev. Mod. Phys. **82**, 1225 (2010). (Cited on pages **2** and **19**)

[49] S. Inouye, M. R. Andrews, J. Stenger, H.-J. Miesner, D. M. Stamper-Kurn, and

W. Ketterle. *Observation of Feshbach resonances in a Bose-Einstein condensate*. Nature **392**, 151 (1998). (Cited on page **2**)

[50] P. Courteille, R. S. Freeland, D. J. Heinzen, F. A. van Abeelen, and B. J. Verhaar. *Observation of a Feshbach resonance in cold atom scattering*. Phys. Rev. Lett. **81**, 69 (1998). (Cited on page **2**)

[51] E. Tiesinga, A. J. Moerdijk, B. J. Verhaar, and H. T. C. Stoof. *Conditions for Bose-Einstein condensation in magnetically trapped atomic cesium*. Phys. Rev. A **46**, R1167 (1992). (Cited on page **2**)

[52] J. Stenger, S. Inouye, M. R. Andrews, H.-J. Miesner, D. M. Stamper-Kurn, and W. Ketterle. *Strongly enhanced inelastic collisions in a Bose-Einstein condensate near Feshbach resonances*. Phys. Rev. Lett. **82**, 2422 (1999). (Cited on page **2**)

[53] T. Kinoshita, T. Wenger, and D. S. Weiss. *Observation of a one-dimensional Tonks-Girardeau gas*. Science **305**, 1125 (2004). (Cited on page **2**)

[54] B. Paredes, A. Widera, V. Murg, O. Mandel, S. Fölling, I. Cirac, G. V. Shlyapnikov, T. W. Hänsch, and I. Bloch. *Tonks-Girardeau gas of ultracold atoms in an optical lattice*. Nature **429**, 277 (2004). (Cited on page **2**)

[55] B. DeMarco and D. S. Jin. *Onset of Fermi degeneracy in a trapped atomic gas*. Science **285**, 1703 (1999). (Cited on page **2**)

[56] A. G. Truscott, K. E. Strecker, W. I. McAlexander, G. B. Partridge, and R. G. Hulet. *Observation of Fermi pressure in a gas of trapped atoms*. Science **291**, 2570 (2001). (Cited on page **3**)

[57] F. Schreck, L. Khaykovich, K. L. Corwin, G. Ferrari, T. Bourdel, J. Cubizolles, and C. Salomon. *Quasipure Bose-Einstein condensate immersed in a Fermi sea*. Phys. Rev. Lett. **87**, 080403 (2001). (Cited on page **3**)

[58] S. R. Granade, M. E. Gehm, K. M. O'Hara, and J. E. Thomas. *All-optical production of a degenerate Fermi gas*. Phys. Rev. Lett. **88**, 120405 (2002). (Cited on page **3**)

[59] Z. Hadzibabic, C. A. Stan, K. Dieckmann, S. Gupta, M. W. Zwierlein, A. Görlitz, and W. Ketterle. *Two-species mixture of quantum degenerate Bose and Fermi gases*. Phys. Rev. Lett. **88**, 160401 (2002). (Cited on page **3**)

[60] G. Roati, F. Riboli, G. Modugno, and M. Inguscio. *Fermi-Bose quantum degenerate ^{40}K-^{87}Rb mixture with attractive interaction*. Phys. Rev. Lett. **89**, 150403 (2002). (Cited on page **3**)

[61] T. Rom, T. Best, D. van Oosten, U. Schneider, S. Fölling, B. Paredes, and I. Bloch. *Free fermion antibunching in a degenerate atomic Fermi gas released from an optical lattice.* Nature **444**, 733 (2006). (Cited on pages **3**, **4**, and **83**)

[62] T. Müller, B. Zimmermann, J. Meineke, J.-P. Brantut, T. Esslinger, and H. Moritz. *Local observation of antibunching in a trapped Fermi gas.* Phys. Rev. Lett. **105**, 040401 (2010). (Cited on pages **3** and **75**)

[63] C. Sanner, E. J. Su, A. Keshet, R. Gommers, Y.-i. Shin, W. Huang, and W. Ketterle. *Suppression of density fluctuations in a quantum degenerate Fermi gas.* Phys. Rev. Lett. **105**, 040402 (2010). (Cited on pages **3** and **75**)

[64] D. S. Petrov, C. Salomon, and G. V. Shlyapnikov. *Weakly bound dimers of fermionic atoms.* Phys. Rev. Lett. **93**, 90404 (2004). (Cited on page **3**)

[65] S. Giorgini, L. P. Pitaevskii, and S. Stringari. *Theory of ultracold atomic Fermi gases.* Rev. Mod. Phys. **80**, 1215 (2008). (Cited on pages **3** and **9**)

[66] K. M. O'Hara, S. L. Hemmer, M. E. Gehm, S. R. Granade, and J. E. Thomas. *Observation of a strongly-interacting degenerate Fermi gas of atoms.* Science **298**, 2179 (2002). (Cited on page **3**)

[67] T. Bourdel, J. Cubizolles, L. Khaykovich, K. M. F. Magalhães, S. J. J. M. F. Kokkelmans, G. V. Shlyapnikov, and C. Salomon. *Measurement of the interaction energy near a Feshbach Resonance in a ^{6}Li Fermi gas.* Phys. Rev. Lett. **91**, 020402 (2003). (Cited on page **3**)

[68] M. Greiner, C. A. Regal, and D. S. Jin. *Emergence of a molecular Bose-Einstein condensate from a Fermi gas.* Nature **426**, 537 (2003). (Cited on page **3**)

[69] S. Jochim, M. Bartenstein, A. Altmeyer, G. Hendl, S. Riedl, C. Chin, J. Hecker Denschlag, and R. Grimm. *Bose-Einstein condensation of molecules.* Science **302**, 2101 (2003). (Cited on page **3**)

[70] M. W. Zwierlein, C. A. Stan, C. H. Schunck, S. M. F. Raupach, S. Gupta, Z. Hadzibabic, and W. Ketterle. *Observation of Bose-Einstein condensation of molecules.* Phys. Rev. Lett. **91**, 250401 (2003). (Cited on page **3**)

[71] C. A. Regal, M. Greiner, and D. S. Jin. *Observation of resonance condensation of fermionic atom pairs.* Phys. Rev. Lett. **92**, 040403 (2004). (Cited on page **3**)

[72] H. T. C. Stoof, M. Houbiers, C. A. Sackett, and R. G. Hulet. *Superfluidity of spin-polarized ^{6}Li.* Phys. Rev. Lett. **76**, 10 (1996). (Cited on page **3**)

[73] C. Chin, M. Bartenstein, A. Altmeyer, S. Riedl, S. Jochim, J. Hecker Denschlag,

and R. Grimm. *Observation of the pairing gap in a strongly interacting Fermi gas.* Science **305**, 1128 (2004). (Cited on page **3**)

[74] M. W. Zwierlein, J. R. Abo-Shaeer, A. Schirotzek, C. H. Schunck, and W. Ketterle. *Vortices and superfluidity in a strongly interacting Fermi gas.* Nature **435**, 1047 (2005). (Cited on pages **3** and **10**)

[75] B. J. DeSalvo, M. Yan, P. G. Mickelson, Y. N. Martinez de Escobar, and T. C. Killian. *Degenerate Fermi gas of ^{87}Sr.* Phys. Rev. Lett. **105**, 030402 (2010). (Cited on page **3**)

[76] M. K. Tey, S. Stellmer, R. Grimm, and F. Schreck. *Double-degenerate Bose-Fermi mixture of strontium.* Phys. Rev. A **82**, 011608 (2010). (Cited on page **3**)

[77] M. Lu, N. Q. Burdick, and B. L. Lev. *Quantum degenerate dipolar Fermi gas.* Phys. Rev. Lett. **108**, 215301 (2012). (Cited on page **3**)

[78] K. Aikawa, A. Frisch, M. Mark, S. Baier, R. Grimm, and F. Ferlaino. *Reaching Fermi degeneracy via universal dipolar scattering.* Phys. Rev. Lett. **112**, 010404 (2014). (Cited on page **3**)

[79] T. Fukuhara, Y. Takasu, S. Sugawa, and Y. Takahashi. *Quantum degenerate Fermi gases of ytterbium atoms.* J. Low Temp. Phys. **148**, 441 (2007). (Cited on page **3**)

[80] S. Taie, Y. Takasu, S. Sugawa, R. Yamazaki, T. Tsujimoto, R. Murakami, and Y. Takahashi. *Realization of a $SU(2) \times SU(6)$ system of fermions in a cold atomic gas.* Phys. Rev. Lett. **105**, 190401 (2010). (Cited on page **3**)

[81] M. Takamoto, F.-L. Hong, R. Higashi, and H. Katori. *An optical lattice clock.* Nature **435**, 321 (2005). (Cited on page **3**)

[82] N. Hinkley, J. A. Sherman, N. B. Phillips, M. Schioppo, N. D. Lemke, K. Beloy, M. Pizzocaro, C. W. Oates, and A. D. Ludlow. *An atomic clock with 10^{-18} instability.* Science **341**, 1215 (2013). (Cited on page **3**)

[83] B. J. Bloom, T. L. Nicholson, J. R. Williams, S. L. Campbell, M. Bishof, X. Zhang, W. Zhang, S. L. Bromley, and J. Ye. *An optical lattice clock with accuracy and stability at the 10^{-18} level.* Nature **506**, 71 (2014). (Cited on page **3**)

[84] A. J. Daley, M. M. Boyd, J. Ye, and P. Zoller. *Quantum computing with alkaline-earth-metal atoms.* Phys. Rev. Lett. **101**, 170504 (2008). (Cited on page **3**)

[85] A. V. Gorshkov, A. M. Rey, A. J. Daley, M. M. Boyd, J. Ye, P. Zoller, and M. D. Lukin. *Alkaline-earth-metal atoms as few-qubit quantum registers.* Phys. Rev. Lett. **102**, 110503 (2009). (Cited on page **3**)

[86] K. Aikawa, S. Baier, A. Frisch, M. Mark, C. Ravensbergen, and F. Ferlaino. *Observation of Fermi surface deformation in a dipolar gas*. Science **345**, 1484 (2014). (Cited on page **3**)

[87] M. Hermele, V. Gurarie, and A. M. Rey. *Mott insulators of ultracold fermionic alkaline earth atoms: underconstrained magnetism and chiral spin liquid*. Phys. Rev. Lett. **103**, 135301 (2009). (Cited on page **3**)

[88] A. V. Gorshkov, M. Hermele, V. Gurarie, C. Xu, P. S. Julienne, J. Ye, P. Zoller, E. Demler, M. D. Lukin, and A. M. Rey. *Two-orbital $SU(N)$ magnetism with ultracold alkaline-earth atoms*. Nat. Phys. **6**, 289 (2010). (Cited on page **3**)

[89] D. Jaksch, C. Bruder, J. I. Cirac, C. W. Gardiner, and P. Zoller. *Cold bosonic atoms in optical lattices*. Phys. Rev. Lett. **81**, 3108 (1998). (Cited on pages **3** and **12**)

[90] K. I. Petsas, A. B. Coates, and G. Grynberg. *Crystallography of optical lattices*. Phys. Rev. A **50**, 5173 (1994). (Cited on page **3**)

[91] M. Greiner, O. Mandel, T. Esslinger, T. W. Hänsch, and I. Bloch. *Quantum phase transition from a superfluid to a Mott insulator in a gas of ultracold atoms*. Nature **415**, 39 (2002). (Cited on pages **3**, **4**, and **12**)

[92] M. Lewenstein, A. Sanpera, V. Ahufinger, B. Damski, A. Sen(De), and U. Sen. *Ultracold atomic gases in optical lattices: mimicking condensed matter physics and beyond*. Adv. Phys. **56**, 243 (2007). (Cited on page **3**)

[93] M. Köhl, H. Moritz, T. Stöferle, K. Günter, and T. Esslinger. *Fermionic atoms in a three dimensional optical lattice: observing Fermi surfaces, dynamics, and interactions*. Phys. Rev. Lett. **94**, 080403 (2005). (Cited on page **3**)

[94] A. Georges. *Condensed-matter physics with light and atoms: strongly correlated cold fermions in optical lattices*. In *Ultra-cold Fermi Gases*. Società Italiana di Fisica, Bologna (2007). (Cited on pages **3**, **13**, and **14**)

[95] R. Jördens, N. Strohmaier, K. Günter, H. Moritz, and T. Esslinger. *A Mott insulator of fermionic atoms in an optical lattice*. Nature **455**, 204 (2008). (Cited on pages **3** and **14**)

[96] U. Schneider, L. Hackermüller, S. Will, T. Best, I. Bloch, T. A. Costi, R. W. Helmes, D. Rasch, and A. Rosch. *Metallic and insulating phases of repulsively interacting fermions in a 3D optical lattice*. Science **322**, 1520 (2008). (Cited on pages **3** and **14**)

[97] D. Greif, T. Uehlinger, G. Jotzu, L. Tarruell, and T. Esslinger. *Short-range quantum magnetism of ultracold fermions in an optical lattice*. Science **340**, 1307 (2013). (Cited on pages **3**, **15**, and **91**)

[98] R. A. Hart, P. M. Duarte, T.-L. Yang, X. Liu, T. Paiva, E. Khatami, R. T. Scalettar, N. Trivedi, D. A. Huse, and R. G. Hulet. *Observation of antiferromagnetic correlations in the Hubbard model with ultracold atoms*. Nature **519**, 211 (2015). (Cited on pages **3**, **4**, **9**, **15**, and **91**)

[99] J. K. Chin, D. E. Miller, Y. Liu, C. Stan, W. Setiawan, C. Sanner, K. Xu, and W. Ketterle. *Evidence for superfluidity of ultracold fermions in an optical lattice*. Nature **443**, 961 (2006). (Cited on page **4**)

[100] E. Altman, E. Demler, and M. D. Lukin. *Probing many-body states of ultracold atoms via noise correlations*. Phys. Rev. A **70**, 013603 (2004). (Cited on pages **4** and **83**)

[101] S. Fölling, F. Gerbier, A. Widera, O. Mandel, T. Gericke, and I. Bloch. *Spatial quantum noise interferometry in expanding ultracold atom clouds*. Nature **434**, 481 (2005). (Cited on pages **4** and **83**)

[102] M. Greiner, I. Bloch, O. Mandel, T. W. Hänsch, and T. Esslinger. *Exploring phase coherence in a 2D lattice of Bose-Einstein condensates*. Phys. Rev. Lett. **87**, 160405 (2001). (Cited on page **4**)

[103] D. Clément, N. Fabbri, L. Fallani, C. Fort, and M. Inguscio. *Exploring correlated 1D Bose gases from the superfluid to the Mott-insulator state by inelastic light scattering*. Phys. Rev. Lett. **102** (2009). (Cited on page **4**)

[104] N. Gemelke, X. Zhang, C.-L. Hung, and C. Chin. *In situ observation of incompressible Mott-insulating domains in ultracold atomic gases*. Nature **460**, 995 (2009). (Cited on pages **4** and **12**)

[105] C. Hofrichter, L. Riegger, F. Scazza, M. Höfer, D. R. Fernandes, I. Bloch, and S. Fölling. *Direct probing of the Mott crossover in the SU(N) Fermi-Hubbard model*. arXiv. 1511.07287 (2015). (Cited on page **4**)

[106] K. D. Nelson, X. Li, and D. S. Weiss. *Imaging single atoms in a three-dimensional array*. Nat. Phys. **3**, 556 (2007). (Cited on page **4**)

[107] A. Itah, H. Veksler, O. Lahav, A. Blumkin, C. Moreno, C. Gordon, and J. Steinhauer. *Direct observation of a sub-Poissonian number distribution of atoms in an optical lattice*. Phys. Rev. Lett. **104**, 113001 (2010). (Cited on page **4**)

[108] T. Gericke, P. Würtz, D. Reitz, T. Langen, and H. Ott. *High-resolution scanning electron microscopy of an ultracold quantum gas*. Nat. Phys. **4**, 949 (2008). (Cited on page **4**)

[109] P. Würtz, T. Langen, T. Gericke, A. Koglbauer, and H. Ott. *Experimental demonstration of single-site addressability in a two-dimensional optical lattice*. Phys. Rev. Lett. **103**, 080404 (2009). (Cited on page **4**)

[110] W. S. Bakr, J. I. Gillen, A. Peng, S. Fölling, and M. Greiner. *A quantum gas microscope for detecting single atoms in a Hubbard-regime optical lattice*. Nature **462**, 74 (2009). (Cited on pages **4**, **20**, **43**, and **67**)

[111] J. F. Sherson, C. Weitenberg, M. Endres, M. Cheneau, I. Bloch, and S. Kuhr. *Single-atom-resolved fluorescence imaging of an atomic Mott insulator*. Nature **467**, 68 (2010). (Cited on pages **4**, **12**, **20**, **43**, and **67**)

[112] W. S. Bakr, A. Peng, M. E. Tai, R. Ma, J. Simon, J. I. Gillen, S. Fölling, L. Pollet, and M. Greiner. *Probing the superfluid-to-Mott insulator transition at the single-atom level*. Science **329**, 547 (2010). (Cited on pages **4** and **12**)

[113] T. Fukuhara, A. Kantian, M. Endres, M. Cheneau, P. Schauß, S. Hild, D. Bellem, U. Schollwöck, T. Giamarchi, C. Gross, I. Bloch, and S. Kuhr. *Quantum dynamics of a mobile spin impurity*. Nat. Phys. **9**, 235 (2013). (Cited on pages **4** and **91**)

[114] S. Hild, T. Fukuhara, P. Schauß, J. Zeiher, M. Knap, E. Demler, I. Bloch, and C. Gross. *Far-from-equilibrium spin transport in Heisenberg quantum magnets*. Phys. Rev. Lett. **113**, 147205 (2014). (Cited on pages **4** and **92**)

[115] P. M. Preiss, R. Ma, M. E. Tai, A. Lukin, M. Rispoli, P. Zupancic, Y. Lahini, R. Islam, and M. Greiner. *Strongly correlated quantum walks in optical lattices*. Science **347**, 1229 (2015). (Cited on page **4**)

[116] M. Cheneau, P. Barmettler, D. Poletti, M. Endres, P. Schauss, T. Fukuhara, C. Gross, I. Bloch, C. Kollath, and S. Kuhr. *Light-cone-like spreading of correlations in a quantum many-body system*. Nature **481**, 484 (2012). (Cited on pages **4** and **92**)

[117] M. Endres, M. Cheneau, T. Fukuhara, C. Weitenberg, P. Schauß, C. Gross, L. Mazza, M. C. Bañuls, L. Pollet, I. Bloch, and S. Kuhr. *Observation of correlated particle-hole pairs and string order in low-dimensional Mott insulators*. Science **334**, 200 (2011). (Cited on pages **4** and **83**)

[118] T. Fukuhara, P. Schauß, M. Endres, S. Hild, M. Cheneau, I. Bloch, and C. Gross. *Microscopic observation of magnon bound states and their dynamics*. Nature **502**, 76 (2013). (Cited on page **4**)

[119] J. Simon, W. S. Bakr, R. Ma, M. E. Tai, P. M. Preiss, and M. Greiner. *Quantum simulation of antiferromagnetic spin chains in an optical lattice*. Nature **472**, 307 (2011). (Cited on page **4**)

[120] P. Schauß, M. Cheneau, M. Endres, T. Fukuhara, S. Hild, A. Omran, T. Pohl, C. Gross, S. Kuhr, and I. Bloch. *Observation of spatially ordered structures in a two-dimensional Rydberg gas*. Nature **490**, 87 (2012). (Cited on page **4**)

[121] P. Schauß, J. Zeiher, T. Fukuhara, S. Hild, M. Cheneau, T. Macrì, T. Pohl, I. Bloch, and C. Gross. *Crystallization in Ising quantum magnets*. Science **347**, 1455 (2015). (Cited on page **4**)

[122] J. Zeiher, P. Schauß, S. Hild, T. Macrì, I. Bloch, and C. Gross. *Microscopic characterization of scalable coherent Rydberg superatoms*. Phys. Rev. X **5**, 031015 (2015). (Cited on page **4**)

[123] T. Fukuhara, S. Hild, J. Zeiher, P. Schauß, I. Bloch, M. Endres, and C. Gross. *Spatially resolved detection of a spin-entanglement wave in a Bose-Hubbard chain*. Phys. Rev. Lett. **115**, 035302 (2015). (Cited on pages **4** and **67**)

[124] R. Islam, R. Ma, P. M. Preiss, M. Eric Tai, A. Lukin, M. Rispoli, and M. Greiner. *Measuring entanglement entropy in a quantum many-body system*. Nature **528**, 77 (2015). (Cited on page **4**)

[125] M. Miranda, R. Inoue, Y. Okuyama, A. Nakamoto, and M. Kozuma. *Site-resolved imaging of ytterbium atoms in a two-dimensional optical lattice*. Phys. Rev. A **91**, 063414 (2015). (Cited on page **4**)

[126] R. Yamamoto, J. Kobayashi, T. Kuno, K. Kato, and Y. Takahashi. *An ytterbium quantum gas microscope with narrow-line laser cooling*. New J. Phys. **18**, 023016 (2016). (Cited on page **4**)

[127] E. Haller, J. Hudson, A. Kelly, D. A. Cotta, B. Peaudecerf, G. D. Bruce, and S. Kuhr. *Single-atom imaging of fermions in a quantum-gas microscope*. Nat. Phys. **11**, 738 (2015). (Cited on pages **4**, **19**, and **20**)

[128] L. W. Cheuk, M. A. Nichols, M. Okan, T. Gersdorf, V. V. Ramasesh, W. S. Bakr, T. Lompe, and M. W. Zwierlein. *Quantum-gas microscope for fermionic atoms*. Phys. Rev. Lett. **114**, 193001 (2015). (Cited on pages **4**, **19**, and **57**)

[129] M. F. Parsons, F. Huber, A. Mazurenko, C. S. Chiu, W. Setiawan, K. Wooley-Brown, S. Blatt, and M. Greiner. *Site-resolved imaging of fermionic ^6Li in an optical lattice*. Phys. Rev. Lett. **114**, 213002 (2015). (Cited on pages **4**, **19**, **20**, and **57**)

[130] G. J. A. Edge, R. Anderson, D. Jervis, D. C. McKay, R. Day, S. Trotzky, and J. H. Thywissen. *Imaging and addressing of individual fermionic atoms in an optical lattice*. Phys. Rev. A **92**, 063406 (2015). (Cited on pages **4**, **19**, and **20**)

[131] A. Omran, M. Boll, T. A. Hilker, K. Kleinlein, G. Salomon, I. Bloch, and C. Gross. *Microscopic observation of Pauli blocking in degenerate fermionic lattice gases*. Phys. Rev. Lett. **115**, 263001 (2015). (Cited on pages **4**, **19**, and **20**)

[132] L. D. Landau and E. M. Lifshitz. *Quantum mechanics*. Pergamon Press Ltd. (1977). (Cited on page **7**)

[133] N. W. Ashcroft and N. D. Mermin. *Solid state physics*. Brooks Cole (1976). (Cited on pages **8**, **9**, **10**, and **12**)

[134] M. Horikoshi, S. Nakajima, M. Ueda, and T. Mukaiyama. *Measurement of universal thermodynamic functions for a unitary Fermi gas*. Science **327**, 442 (2010). (Cited on page **9**)

[135] S. Nascimbène, N. Navon, K. J. Jiang, F. Chevy, and C. Salomon. *Exploring the thermodynamics of a universal Fermi gas*. Nature **463**, 1057 (2010). (Cited on page **9**)

[136] N. Navon, S. Nascimbène, F. Chevy, and C. Salomon. *The equation of state of a low-temperature Fermi gas with tunable interactions*. Science **328**, 729 (2010). (Cited on page **9**)

[137] T. Yefsah, R. Desbuquois, L. Chomaz, K. J. Günter, and J. Dalibard. *Exploring the thermodynamics of a two-dimensional Bose gas*. Phys. Rev. Lett. **107**, 130401 (2011). (Cited on page **9**)

[138] M. J. H. Ku, A. T. Sommer, L. W. Cheuk, and M. W. Zwierlein. *Revealing the superfluid lambda transition in the universal thermodynamics of a unitary Fermi gas*. Science **335**, 563 (2012). (Cited on pages **9** and **10**)

[139] K. Fenech, P. Dyke, T. Peppler, M. G. Lingham, S. Hoinka, H. Hu, and C. J. Vale. *Thermodynamics of an attractive 2D Fermi gas*. Phys. Rev. Lett. **116**, 045302 (2016). (Cited on page **9**)

[140] I. Boettcher, L. Bayha, D. Kedar, P. A. Murthy, M. Neidig, M. G. Ries, A. N. Wenz, G. Zürn, S. Jochim, and T. Enss. *Equation of state of ultracold fermions in the 2D BEC-BCS crossover region*. Phys. Rev. Lett. **116**, 045303 (2016). (Cited on page **9**)

[141] F. Schwabl. *Statistical mechanics*. Springer-Verlag Berlin Heidelberg, 2nd edition (2006). (Cited on page **9**)

[142] G. Baym and F. K. Lamb. *Neutron stars*. arXiv. physics/0503245 (2005). (Cited on page **9**)

[143] W. Ketterle and M. W. Zwierlein. *Making, probing and understanding ultracold*

Fermi gases. In *Ultra-cold Fermi Gases*. Società Italiana di Fisica, Bologna (2007). (Cited on page **9**)

[144] M. W. Zwierlein, C. H. Schunck, A. Schirotzek, and W. Ketterle. *Direct observation of the superfluid phase transition in ultracold Fermi gases*. Nature **442**, 54 (2006). (Cited on pages **9** and **16**)

[145] R. Haussmann and W. Zwerger. *Thermodynamics of a trapped unitary Fermi gas*. Phys. Rev. A **78**, 063602 (2008). (Cited on page **9**)

[146] L. A. Sidorenkov, M. K. Tey, R. Grimm, Y.-H. Hou, L. Pitaevskii, and S. Stringari. *Second sound and the superfluid fraction in a Fermi gas with resonant interactions*. Nature **498**, 78 (2013). (Cited on page **10**)

[147] F. Werner, O. Parcollet, A. Georges, and S. R. Hassan. *Interaction-induced adiabatic cooling and antiferromagnetism of cold fermions in optical lattices*. Phys. Rev. Lett. **95**, 056401 (2005). (Cited on pages **10** and **14**)

[148] M. Rigol and A. Muramatsu. *Confinement control by optical lattices*. Phys. Rev. A **70**, 043627 (2004). (Cited on pages **10** and **86**)

[149] S. Will. *Interacting bosons and fermions in three-dimensional optical lattice potentials. From atom optics to quantum simulation*. PhD thesis, Johannes Gutenberg-Universität Mainz (2011). (Cited on page **10**)

[150] J. Hubbard. *Electron correlations in narrow energy bands*. Proc. R. Soc. Lond. A **276**, 238 (1963). (Cited on page **11**)

[151] J. Hubbard. *Electron correlations in narrow energy bands II. The degenerate band case*. Proc. R. Soc. Lond. A **277**, 237 (1964). (Cited on page **11**)

[152] J. Hubbard. *Electron correlations in narrow energy bands III. An improved solution*. Proc. R. Soc. Lond. A **281**, 401 (1964). (Cited on page **11**)

[153] N. F. Mott and R. Peierls. *Discussion of the paper by de Boer and Verwey*. Proc. Phys. Soc. **49**, 72 (1937). (Cited on page **12**)

[154] N. F. Mott. *The basis of the electron theory of metals, with special reference to the transition metals*. Proc. Phys. Soc. **62**, 416 (1949). (Cited on page **12**)

[155] M. P. A. Fisher, P. B. Weichman, G. Grinstein, and D. S. Fisher. *Boson localization and the superfluid-insulator transition*. Phys. Rev. B **40**, 546 (1989). (Cited on page **12**)

[156] D. Jaksch and P. Zoller. *The cold atom Hubbard toolbox*. Ann. Phys. **315**, 52 (2005). (Cited on page **12**)

[157] S. Fölling, A. Widera, T. Müller, F. Gerbier, and I. Bloch. *Formation of spatial shell structure in the superfluid to Mott insulator transition.* Phys. Rev. Lett. **97**, 060403 (2006). (Cited on page **12**)

[158] M. Endres, T. Fukuhara, D. Pekker, M. Cheneau, P. Schauß, C. Gross, E. Demler, S. Kuhr, and I. Bloch. *The 'Higgs' amplitude mode at the two-dimensional super-fluid/Mott insulator transition.* Nature **487**, 454 (2012). (Cited on page **12**)

[159] W. Hofstetter, J. I. Cirac, P. Zoller, E. Demler, and M. D. Lukin. *High-temperature superfluidity of fermionic atoms in optical lattices.* Phys. Rev. Lett. **89**, 220407 (2002). (Cited on pages **12** and **16**)

[160] P. A. Lee, N. Nagaosa, and X.-G. Wen. *Doping a Mott insulator: physics of high-temperature superconductivity.* Rev. Mod. Phys. **78**, 17 (2006). (Cited on pages **12** and **16**)

[161] J. E. Hirsch. *Two-dimensional Hubbard model: numerical simulation study.* Phys. Rev. B **31**, 4403 (1985). (Cited on page **12**)

[162] E. Y. Loh, J. E. Gubernatis, R. T. Scalettar, S. R. White, D. J. Scalapino, and R. L. Sugar. *Sign problem in the numerical simulation of many-electron systems.* Phys. Rev. B **41**, 9301 (1990). (Cited on page **12**)

[163] T. Esslinger. *Fermi-Hubbard physics with atoms in an optical lattice.* Annu. Rev. Cond. Mat. Phys. **1**, 129 (2010). (Cited on pages **12** and **15**)

[164] J. Weiner, V. S. Bagnato, S. Zilio, and P. S. Julienne. *Experiments and theory in cold and ultracold collisions.* Rev. Mod. Phys. **71**, 1 (1999). (Cited on page **13**)

[165] D. Greif, M. F. Parsons, A. Mazurenko, C. S. Chiu, S. Blatt, F. Huber, G. Ji, and M. Greiner. *Site-resolved imaging of a fermionic Mott insulator.* Science **351**, 953 (2016). (Cited on pages **14** and **90**)

[166] R. Jördens, L. Tarruell, D. Greif, T. Uehlinger, N. Strohmaier, H. Moritz, T. Esslinger, L. De Leo, C. Kollath, A. Georges, V. Scarola, L. Pollet, E. Burovski, E. Kozik, and M. Troyer. *Quantitative determination of temperature in the approach to magnetic order of ultracold fermions in an optical lattice.* Phys. Rev. Lett. **104**, 180401 (2010). (Cited on page **14**)

[167] T. Paiva, R. Scalettar, M. Randeria, and N. Trivedi. *Fermions in 2D optical lattices: temperature and entropy scales for observing antiferromagnetism and superfluidity.* Phys. Rev. Lett. **104**, 066406 (2010). (Cited on page **15**)

[168] C. L. Cleveland and R. Medina A. *Obtaining a Heisenberg Hamiltonian from the Hubbard model.* Am. J. Phys. **44**, 44 (1976). (Cited on page **15**)

[169] E. Fradkin. *Field theories of condensed matter physics*. Cambridge University Press, 2nd edition (2013). (Cited on page 15)

[170] R. Micnas, J. Ranninger, and S. Robaszkiewicz. *Superconductivity in narrow-band systems with local nonretarded attractive interactions*. Rev. Mod. Phys. **62**, 113 (1990). (Cited on pages 15 and 16)

[171] A. F. Ho, M. A. Cazalilla, and T. Giamarchi. *Quantum simulation of the Hubbard model: the attractive route*. Phys. Rev. A **79**, 033620 (2009). (Cited on page 16)

[172] M. R. Norman. *The challenge of unconventional superconductivity*. Science **332**, 196 (2011). (Cited on page 16)

[173] D. E. Sheehy and L. Radzihovsky. *BEC-BCS crossover, phase transitions and phase separation in polarized resonantly-paired superfluids*. Ann. Phys. **322**, 1790 (2007). (Cited on page 16)

[174] F. Chevy and C. Mora. *Ultra-cold polarized Fermi gases*. Rep. Prog. Phys. **73**, 112401 (2010). (Cited on pages 16 and 92)

[175] K. B. Gubbels and H. T. C. Stoof. *Imbalanced Fermi gases at unitarity*. Phys. Rep. **525**, 255 (2013). (Cited on page 16)

[176] Y. Shin, M. W. Zwierlein, C. H. Schunck, A. Schirotzek, and W. Ketterle. *Observation of phase separation in a strongly interacting imbalanced Fermi gas*. Phys. Rev. Lett. **97**, 030401 (2006). (Cited on page 16)

[177] Y.-i. Shin, C. H. Schunck, A. Schirotzek, and W. Ketterle. *Phase diagram of a two-component Fermi gas with resonant interactions*. Nature **451**, 689 (2008). (Cited on page 16)

[178] Y.-a. Liao, A. S. C. Rittner, T. Paprotta, W. Li, G. B. Partridge, R. G. Hulet, S. K. Baur, and E. J. Mueller. *Spin-imbalance in a one-dimensional Fermi gas*. Nature **467**, 567 (2010). (Cited on page 16)

[179] P. Fulde and R. A. Ferrell. *Superconductivity in a strong spin-exchange field*. Phys. Rev. **135**, A550 (1964). (Cited on pages 16 and 92)

[180] A. I. Larkin and Y. N. Ovchinnikov. *Nonuniform state of superconductors*. Zh. Eksp. Teor. Fiz. **47**, 1136 (1964). (Cited on pages 16 and 92)

[181] M. E. Gehm. *Properties of ^6Li* (2003). https://www.physics.ncsu.edu/jet/techdocs/pdf/PropertiesOfLi.pdf. (Cited on pages 17, 18, 21, and 48)

[182] P. M. Duarte, R. A. Hart, J. M. Hitchcock, T. A. Corcovilos, T.-L. Yang, A. Reed,

and R. G. Hulet. *All-optical production of a lithium quantum gas using narrow-line laser cooling.* Phys. Rev. A **84**, 061406 (2011). (Cited on pages **17**, **27**, and **47**)

[183] W. Nagourney, W. Happer, and A. Lurio. *Level-crossing study of the hyperfine structure of lithium.* Phys. Rev. A **17**, 1394 (1978). (Cited on page **18**)

[184] W. R. Johnson, U. I. Safronova, A. Derevianko, and M. S. Safronova. *Relativistic many-body calculation of energies, lifetimes, hyperfine constants, and polarizabilities in ^7Li.* Phys. Rev. A **77**, 022510 (2008). (Cited on page **18**)

[185] G. Breit and I. I. Rabi. *Measurement of nuclear spin.* Phys. Rev. **38**, 2082 (1931). (Cited on page **18**)

[186] G. Zürn, T. Lompe, A. N. Wenz, S. Jochim, P. S. Julienne, and J. M. Hutson. *Precise characterization of ^6Li Feshbach resonances using trap-sideband-resolved RF spectroscopy of weakly bound molecules.* Phys. Rev. Lett. **110**, 135301 (2013). (Cited on page **19**)

[187] E. L. Hazlett, Y. Zhang, R. W. Stites, and K. M. O'Hara. *Realization of a resonant Fermi gas with a large effective range.* Phys. Rev. Lett. **108**, 45304 (2012). (Cited on page **19**)

[188] T. G. Tiecke. *Properties of potassium* (2011). http://www.tobiastiecke.nl/archive/PotassiumProperties.pdf. (Cited on page **20**)

[189] R. Wei and E. J. Mueller. *Magnetic-field dependence of Raman coupling in alkali-metal atoms.* Phys. Rev. A **87**, 042514 (2013). (Cited on page **20**)

[190] G. Morigi, J. Eschner, and C. H. Keitel. *Ground state laser cooling using electromagnetically induced transparency.* Phys. Rev. Lett. **85**, 4458 (2000). (Cited on page **20**)

[191] C. F. Roos, D. Leibfried, A. Mundt, F. Schmidt-Kaler, J. Eschner, and R. Blatt. *Experimental demonstration of ground state laser cooling with electromagnetically induced transparency.* Phys. Rev. Lett. **85**, 5547 (2000). (Cited on page **20**)

[192] C. Monroe, D. M. Meekhof, B. E. King, S. R. Jefferts, W. M. Itano, D. J. Wineland, and P. Gould. *Resolved-sideband Raman cooling of a bound atom to the 3D zero-point energy.* Phys. Rev. Lett. **75**, 4011 (1995). (Cited on page **20**)

[193] S. E. Hamann, D. L. Haycock, G. Klose, P. H. Pax, I. H. Deutsch, and P. S. Jessen. *Resolved-sideband Raman cooling to the ground state of an optical lattice.* Phys. Rev. Lett. **80**, 4149 (1998). (Cited on page **20**)

[194] A. J. Kerman, V. Vuletić, C. Chin, and S. Chu. *Beyond optical molasses: 3D Raman sideband cooling of atomic cesium to high phase-space density.* Phys. Rev. Lett. **84**, 439 (2000). (Cited on page **20**)

[195] W. D. Phillips and H. Metcalf. *Laser deceleration of an atomic beam*. Phys. Rev. Lett. **48**, 596 (1982). (Cited on page **21**)

[196] T. Hilker. *Laser cooling of bosonic and fermionic lithium*. Diploma thesis, Technische Universität München (2012). (Cited on pages **21** and **48**)

[197] T. Gantner. *Magnetic trapping of lithium-6 and lithium-7*. Diploma thesis, Technische Universität München (2012). (Cited on pages **21** and **23**)

[198] E. Hecht. *Optics*. Addison-Wesley, 4th edition (2001). (Cited on page **24**)

[199] M. Lohse. *Large-spacing optical lattices for many-body physics with degenerate quantum gases*. Diploma thesis, Karlsruher Institut für Technologie (2012). (Cited on pages **24** and **40**)

[200] A. L. Schawlow. *Spectroscopy in a new light*. Rev. Mod. Phys. **54**, 697 (1982). (Cited on page **25**)

[201] D. C. McKay, D. Jervis, D. J. Fine, J. W. Simpson-Porco, G. J. A. Edge, and J. H. Thywissen. *Low-temperature high-density magneto-optical trapping of potassium using the open $4S \rightarrow 5P$ transition at $405\,nm$*. Phys. Rev. A **84**, 063420 (2011). (Cited on page **27**)

[202] J. Sebastian, C. Gross, K. Li, H. C. J. Gan, W. Li, and K. Dieckmann. *Two-stage magneto-optical trapping and narrow-line cooling of ^6Li atoms to high phase-space density*. Phys. Rev. A **90**, 033417 (2014). (Cited on pages **27**, **47**, and **49**)

[203] D. Rio Fernandes, F. Sievers, N. Kretzschmar, S. Wu, C. Salomon, and F. Chevy. *Sub-Doppler laser cooling of fermionic ^{40}K atoms in three-dimensional gray optical molasses*. Europhys. Lett. **100**, 63001 (2012). (Cited on page **27**)

[204] A. T. Grier, I. Ferrier-Barbut, B. S. Rem, M. Delehaye, L. Khaykovich, F. Chevy, and C. Salomon. *Λ-enhanced sub-Doppler cooling of lithium atoms in D_1 gray molasses*. Phys. Rev. A **87**, 063411 (2013). (Cited on page **27**)

[205] G. Salomon, L. Fouché, P. Wang, A. Aspect, P. Bouyer, and T. Bourdel. *Gray-molasses cooling of ^{39}K to a high phase-space density*. Europhys. Lett. **104**, 63002 (2013). (Cited on page **27**)

[206] F. Sievers, N. Kretzschmar, D. Rio Fernandes, D. Suchet, M. Rabinovic, S. Wu, C. V. Parker, L. Khaykovich, C. Salomon, and F. Chevy. *Simultaneous sub-Doppler laser cooling of fermionic ^6Li and ^{40}K on the D_1 line: theory and experiment*. Phys. Rev. A **91**, 023426 (2015). (Cited on page **27**)

[207] A. Burchianti, J. A. Seman, G. Valtolina, A. Morales, M. Inguscio, M. Zaccanti,

and G. Roati. *All-optical production of ^6Li quantum gases*. J. Phys. Conf. Ser. **594**, 012042 (2015). (Cited on page **27**)

[208] A. C. Wilson, C. Ospelkaus, A. P. VanDevender, J. A. Mlynek, K. R. Brown, D. Leibfried, and D. J. Wineland. *A 750-mW, continuous-wave, solid-state laser source at 313 nm for cooling and manipulating trapped $^9Be^+$ ions*. Appl. Phys. B **105**, 741 (2011). (Cited on pages **27** and **29**)

[209] R. J. Rengelink, R. P. M. J. W. Notermans, and W. Vassen. *A simple 2 W continuous-wave laser system for trapping ultracold metastable helium atoms at the 319.8 nm magic wavelength*. arXiv. 1511.00443 (2015). (Cited on page **27**)

[210] J. A. Armstrong, N. Bloembergen, J. Ducuing, and P. S. Pershan. *Interactions between light waves in a nonlinear dielectric*. Phys. Rev. **127**, 1918 (1962). (Cited on page **28**)

[211] J. D. McMullen. *Optical parametric interactions in isotropic materials using a phase-corrected stack of nonlinear dielectric plates*. J. Appl. Phys. **46**, 3076 (1975). (Cited on page **28**)

[212] G. D. Boyd and D. A. Kleinman. *Parametric interaction of focused Gaussian light beams*. J. Appl. Phys. **39**, 3597 (1968). (Cited on page **28**)

[213] W. P. Risk, T. R. Gosnell, and A. V. Nurmikko. *Compact Blue-Green Lasers*. Cambridge University Press (2003). (Cited on page **28**)

[214] S. Guha and J. Falk. *The effects of focusing in the three-frequency parametric upconverter*. J. Appl. Phys. **51**, 50 (1980). (Cited on page **28**)

[215] A. Ashkin, G. D. Boyd, and J. M. Dziedzic. *Resonant optical second harmonic generation and mixing*. IEEE J. Quantum Electron. **QE-2**, 109 (1966). (Cited on page **29**)

[216] R. Paschotta. *Encyclopedia of laser physics and technology*. Wiley-VCH, Berlin (2008). (Cited on page **29**)

[217] T. C. Briles, D. C. Yost, A. Cingöz, J. Ye, and T. R. Schibli. *Simple piezoelectric-actuated mirror with 180 kHz servo bandwidth*. Opt. Express **18**, 9739 (2010). (Cited on page **29**)

[218] F. Seeßelberg. *A dye laser system for NaK-photoassociation spectroscopy*. Master thesis, Ludwig-Maximilians-Universität München (2014). (Cited on page **30**)

[219] R. V. Pound. *Electronic frequency stabilization of microwave oscillators*. Rev. Sci. Instrum. **17**, 490 (1946). (Cited on page **30**)

[220] R. W. P. Drever, J. L. Hall, F. V. Kowalski, J. Hough, G. M. Ford, A. J. Munley, and H. Ward. *Laser phase and frequency stabilization using an optical resonator*. Appl. Phys. B **31**, 97 (1983). (Cited on page **30**)

[221] S. Gerstenkorn and P. Luc. *Atlas du spectre d'absorption de la molécule d'iode, 14800-20000 cm^{-1}*. Centre national de la recherche scientifique (1978). (Cited on page **32**)

[222] M. S. Safronova, U. I. Safronova, and C. W. Clark. *Magic wavelengths for optical cooling and trapping of lithium*. Phys. Rev. A **86**, 042505 (2012). (Cited on pages **32** and **36**)

[223] H. Knöckel and E. Tiemann. *IodineSpec5* (2014). http://www.iqo.uni-hannover.de/250.html. (Cited on pages **32** and **33**)

[224] T. L. Gustavson, A. P. Chikkatur, A. E. Leanhardt, A. Görlitz, S. Gupta, D. E. Pritchard, and W. Ketterle. *Transport of Bose-Einstein condensates with optical tweezers*. Phys. Rev. Lett. **88**, 020401 (2002). (Cited on page **37**)

[225] J. Léonard, M. Lee, A. Morales, T. M. Karg, T. Esslinger, and T. Donner. *Optical transport and manipulation of an ultracold atomic cloud using focus-tunable lenses*. New J. Phys. **16**, 093028 (2014). (Cited on page **37**)

[226] D. M. Stamper-Kurn, H.-J. Miesner, A. P. Chikkatur, S. Inouye, J. Stenger, and W. Ketterle. *Reversible formation of a Bose-Einstein condensate*. Phys. Rev. Lett. **81**, 2194 (1998). (Cited on page **38**)

[227] R. A. Williams, J. D. Pillet, S. Al-Assam, B. Fletcher, M. Shotter, and C. J. Foot. *Dynamic optical lattices: two-dimensional rotating and accordion lattices for ultracold atoms*. Opt. Express **16**, 16977 (2008). (Cited on page **40**)

[228] L. Skuja, H. Hosono, and M. Hirano. *Laser-induced color centers in silica*. Proc. SPIE **4347**, 155 (2001). (Cited on page **49**)

[229] T. Rom. *Bosonische und fermionische Quantengase in dreidimensionalen optischen Gittern*. PhD thesis, Ludwig-Maximilians-Universität München (2009). (Cited on page **52**)

[230] F. Schreck. *Mixtures of ultracold gases: Fermi sea and Bose-Einstein condensate of lithium isotopes*. PhD thesis, Université Pierre et Marie Curie - Paris VI (2002). (Cited on page **53**)

[231] Y. S. Patil, S. Chakram, L. M. Aycock, and M. Vengalattore. *Nondestructive imaging of an ultracold lattice gas*. Phys. Rev. A **90**, 033422 (2014). (Cited on page **57**)

[232] B. J. Lester, A. M. Kaufman, and C. A. Regal. *Raman cooling imaging: detecting single atoms near their ground state of motion*. Phys. Rev. A **90**, 011804 (2014). (Cited on page **57**)

[233] C. Cohen-Tannoudji and D. Guéry-Odelin. *Advances in atomic physics*. World Scientific (2011). (Cited on page **59**)

[234] J. Eschner, G. Morigi, F. Schmidt-Kaler, and R. Blatt. *Laser cooling of trapped ions*. J. Opt. Soc. Am. B **20**, 1003 (2003). (Cited on pages **59** and **60**)

[235] T. Lindeberg. *Feature detection with automatic scale selection*. Int. J. Comp. Vis. **30**, 79 (1998). (Cited on page **63**)

[236] A. Fuhrmanek, R. Bourgain, Y. R. P. Sortais, and A. Browaeys. *Light-assisted collisions between a few cold atoms in a microscopic dipole trap*. Phys. Rev. A **85**, 062708 (2012). (Cited on page **67**)

[237] P. Sompet, A. V. Carpentier, Y. H. Fung, M. McGovern, and M. F. Andersen. *Dynamics of two atoms undergoing light-assisted collisions in an optical microtrap*. Phys. Rev. A **88**, 051401 (2013). (Cited on page **67**)

[238] P. M. Preiss, R. Ma, M. E. Tai, J. Simon, and M. Greiner. *Quantum gas microscopy with spin, atom-number, and multilayer readout*. Phys. Rev. A **91**, 041602 (2015). (Cited on pages **67** and **91**)

[239] L. D. Landau. *A theory of energy transfer II*. Phys. Z. USSR **2**, 46 (1932). (Cited on page **69**)

[240] C. Zener. *Non-adiabatic crossing of energy levels*. Proc. R. Soc. Lond. A **137**, 696 (1932). (Cited on page **69**)

[241] L. D. Landau and E. M. Lifshitz. *Statistical physics, part 1*. Pergamon Press Ltd. (1980). (Cited on pages **76**, **78**, **79**, and **84**)

[242] Y. Castin. *Basic theory tools for degenerate Fermi gases*. In *Ultra-cold Fermi Gases*. Società Italiana di Fisica, Bologna (2007). (Cited on pages **76** and **83**)

[243] E. Fermi. *Zur Quantelung des idealen einatomigen Gases*. Z. Phys. **36**, 902 (1926). (Cited on page **79**)

[244] P. A. M. Dirac. *On the theory of quantum mechanics*. Proc. R. Soc. Lond. A **112**, 661 (1926). (Cited on page **79**)

[245] L. D. Carr, G. V. Shlyapnikov, and Y. Castin. *Achieving a BCS transition in an atomic Fermi gas*. Phys. Rev. Lett. **92**, 150404 (2004). (Cited on page **83**)

[246] I. B. Spielman, W. D. Phillips, and J. V. Porto. *Mott-insulator transition in a two-dimensional atomic Bose gas*. Phys. Rev. Lett. **98**, 080404 (2007). (Cited on page **83**)

[247] T. Jeltes, J. M. McNamara, W. Hogervorst, W. Vassen, V. Krachmalnicoff, M. Schellekens, A. Perrin, H. Chang, D. Boiron, A. Aspect, and C. I. Westbrook. *Comparison of the Hanbury Brown-Twiss effect for bosons and fermions*. Nature **445**, 402 (2007). (Cited on page **83**)

[248] R. Kubo. *The fluctuation-dissipation theorem*. Rep. Prog. Phys. **29**, 255 (1966). (Cited on page **86**)

[249] M. Rigol, A. Muramatsu, G. Batrouni, and R. Scalettar. *Local quantum criticality in confined fermions on optical lattices*. Phys. Rev. Lett. **91**, 130403 (2003). (Cited on page **86**)

[250] M. Gluza, C. Krumnow, M. Friesdorf, C. Gogolin, and J. Eisert. *Equilibration via Gaussification in fermionic lattice systems*. arXiv. 1601.00671 (2016). (Cited on page **87**)

[251] L. D'Alessio, Y. Kafri, A. Polkovnikov, and M. Rigol. *From quantum chaos and eigenstate thermalization to statistical mechanics and thermodynamics*. arXiv. 1509.06411 (2015). (Cited on page **87**)

[252] M. Karski, L. Förster, J. M. Choi, W. Alt, A. Widera, and D. Meschede. *Nearest-neighbor detection of atoms in a 1D optical lattice by fluorescence imaging*. Phys. Rev. Lett. **102**, 053001 (2009). (Cited on page **90**)

[253] S. Nascimbène, Y.-A. Chen, M. Atala, M. Aidelsburger, S. Trotzky, B. Paredes, and I. Bloch. *Experimental realization of plaquette resonating valence-bond states with ultracold atoms in optical superlattices*. Phys. Rev. Lett. **108**, 205301 (2012). (Cited on page **91**)

[254] M. Lohse, C. Schweizer, O. Zilberberg, M. Aidelsburger, and I. Bloch. *A Thouless quantum pump with ultracold bosonic atoms in an optical superlattice*. Nat. Phys. - Adv. online publ. (2015). (Cited on page **91**)

[255] M. Lubasch, V. Murg, U. Schneider, J. I. Cirac, and M. C. Bañuls. *Adiabatic preparation of a Heisenberg antiferromagnet using an optical superlattice*. Phys. Rev. Lett. **107**, 165301 (2011). (Cited on page **91**)

[256] N. Savage. *Digital spatial light modulators*. Nat. Photonics **3**, 170 (2009). (Cited on page **91**)

[257] W. P. Su, J. R. Schrieffer, and A. J. Heeger. *Solitons in polyacetylene*. Phys. Rev. Lett. **42**, 1698 (1979). (Cited on page **92**)

[258] B. K. Stuhl, H.-I. Lu, L. M. Aycock, D. Genkina, and I. B. Spielman. *Visualizing edge states with an atomic Bose gas in the quantum Hall regime.* Science **349**, 1514 (2015). (Cited on page **92**)

[259] M. Mancini, G. Pagano, G. Cappellini, L. Livi, M. Rider, J. Catani, C. Sias, P. Zoller, M. Inguscio, M. Dalmonte, and L. Fallani. *Observation of chiral edge states with neutral fermions in synthetic Hall ribbons.* Science **349**, 1510 (2015). (Cited on page **92**)

[260] H. J. Schulz. *Correlated fermions in one dimension.* Int. J. Mod. Phys. B **05**, 57 (1991). (Cited on page **92**)

[261] T. Giamarchi. *Quantum physics in one dimension.* Clarendon Press (2003). (Cited on page **92**)

[262] A. Angelone, M. Campostrini, and E. Vicari. *Universal quantum behavior of interacting fermions in one-dimensional traps: from few particles to the trap thermodynamic limit.* Phys. Rev. A **89**, 023635 (2014). (Cited on page **92**)

[263] C. Kollath, U. Schollwöck, and W. Zwerger. *Spin-charge separation in cold Fermi gases: a real time analysis.* Phys. Rev. Lett. **95**, 176401 (2005). (Cited on page **92**)

[264] H. Hu, X. J. Liu, and P. D. Drummond. *Phase diagram of a strongly interacting polarized Fermi gas in one dimension.* Phys. Rev. Lett. **98**, 070403 (2007). (Cited on page **92**)

[265] U. Schneider, L. Hackermüller, J. P. Ronzheimer, S. Will, S. Braun, T. Best, I. Bloch, E. Demler, S. Mandt, D. Rasch, and A. Rosch. *Fermionic transport and out-of-equilibrium dynamics in a homogeneous Hubbard model with ultracold atoms.* Nat. Phys. **8**, 213 (2012). (Cited on page **92**)

[266] S. Will, D. Iyer, and M. Rigol. *Observation of coherent quench dynamics in a metallic many-body state of fermionic atoms.* Nat. Comm. **6**, 6009 (2015). (Cited on page 92)

[267] C. Gogolin and J. Eisert. *Equilibration, thermalisation, and the emergence of statistical mechanics in closed quantum systems.* arXiv. 1503.07538 (2015). (Cited on page **92**)

[268] T. Kinoshita, T. Wenger, and D. S. Weiss. *A quantum Newton's cradle.* Nature **440**, 900 (2006). (Cited on page **92**)

[269] M. Rigol, V. Dunjko, V. Yurovsky, and M. Olshanii. *Relaxation in a completely integrable many-body quantum system: an ab initio study of the dynamics of the highly excited states of 1D lattice hard-core bosons.* Phys. Rev. Lett. **98**, 050405 (2007). (Cited on page **92**)

Acknowledgments

For a period of 4.5 years, the people I want to thank are almost too many to enumerate. This is a non-exhaustive, in-no-particular-order list of people I owe a lot of gratitude:

- My supervisor, Immanuel Bloch, for offering this position and inspiring the project with a lot of energy and valuable feedback. Working in this group has been an exceptional experience and I have learned a great deal.

- Our group leader, Christian Groß, for striking the right balance between supervisor and colleague, and for always providing pragmatic input on everything.

- My lab mates Martin Boll, Timon Hilker, Katharina Kleinlein and Guillaume Salomon. We've been through both good and rough times together, and it has certainly paid off.

- The various diploma, master and bachelor students for their valuable work on different projects: Thomas Gantner, Michael Lohse, Thomas Reimann, Konrad Viebahn, Leo Stenzel, Michael Höse, Sam Markson, Chenchen Luo, Seth Coleman, Daniela Köck and Alex Keesling.

- Alex Keesling and Mohamed Zaghoo for being good hosts during my visits to Boston.

- Kristina Schuldt, Marianne Kargl and Ildiko Kecskesi for the administrative support, and the personnel at the MPQ administration for all organisational matters.

- Karsten Förster, Oliver Mödl and Bodo Hecker for the great help with my electronics endeavours. Also, thanks to Anton Mayer for invaluable assistance with mechanical constructions, and to the MPQ machine shop for executing his designs to perfection.

- Guillaume Salomon, Timon Hiker, Martin Boll, Frauke Seeßelberg, Tarik Yefsah and Christian Gross for the helpful proofreading.

- All members of the rubidium, molecule and strontium labs at MPQ, for the borrowed equipment, late night dinners, useful discussions and the fun we had together

- Selim Jochim for agreeing to participate in the exam committee and for the helpful discussions on experimental matters.

- Christoph Gohle for being a beacon of technical expertise and for all the music.

- Tarik Yefsah for helpful advice on experimental and non-experimental matters.

- Sebastian Hild for useful Matlab code and Johannes Zeiher for the SHG cavity design.

- The MPQ purchasing and goods-receiving departments for the support with countless purchase orders.

- Markus Greiner and Sebastian Blatt for the helpful discussions on the fluorescence imaging process.

- Eugene Demler and Michael Knap for valuable discussions on the band insulator statistics.

- Tracy Li and Pranjal Bordia for the motivating weekend meetings.

- Andrew Wilson from NIST, and Pedro Duarte and Jason Nguyen of Rice university for the help on UV laser/MOT related matters.

- Stefan Kuhr and Wilhelm Zwerger for writing recommendation letters when I needed them.

Finally, and most importantly, I would like to thank my family, to whom I owe everything, and whose support simply cannot be adequately described in words.

Thank you!